CMS HF CALORIMETER PMTS AND Ξ_C^+ LIFETIME MEASUREMENT

by

Ugur Akgun

An Abstract

Of a thesis submitted in partial fulfillment of the
requirements for the Doctor of Philosophy
degree in Physics in the
Graduate College of The
University of Iowa

December 2003

Thesis Supervisor: Professor Yasar Onel

ABSTRACT

This thesis consists of two parts: In the first part we describe the Photomultiplier Tube (PMT) selection and testing processes for the Hadronic Forward (HF) calorimeter of the CMS, a Large Hadron Collier (LHC) experiment at CERN. We report the evaluation process of the candidate PMTs from three different manufacturers, the complete tests performed on the 2300 Hamamatsu PMTs which will be used in the HF calorimeter, and the details of the PMT Test Station that is in University of Iowa CMS Laboratories. In the second part we report the Ξ_c^+ lifetime measurement from SELEX, the charm hadro-production experiment at Fermilab. Based upon 301 ± 31 events from three different decay channels, by using the binned maximum likelihood technique, we observe the lifetime of Ξ_c^+ as $427 \pm 31 \pm 13$ fs.

Abstract Approved: _____
Thesis Supervisor

_____
Title and Department

_____
Date

CMS HF CALORIMETER PMTS AND Ξ_C^+ LIFETIME MEASUREMENT

by

Ugur Akgun

A thesis submitted in partial fulfillment of the
requirements for the Doctor of Philosophy
degree in Physics in the
Graduate College of The
University of Iowa

December 2003

Thesis Supervisor: Professor Yasar Onel

Copyright by
UGUR AKGUN
2003
All Rights Reserved

Graduate College
The University of Iowa
Iowa City, Iowa

CERTIFICATE OF APPROVAL

PH.D. THESIS

This is to certify that the Ph.D. thesis of

Ugur Akgun

has been approved by the Examining Committee for the thesis requirement for the Doctor of Philosophy degree in Physics at the December 2003 graduation.

Thesis committee: _____
Yasar Onel, Thesis Supervisor

_____
Edward R. McCliment

_____
Robert L. Merlino

_____
Paul D. Kleiber

_____
Tuong Ton-That

To my Dad and Mom, who always supported me to follow my dreams

ACKNOWLEDGMENTS

I am grateful to my advisor Prof. Yasar Onel for his support during my research on CMS and SELEX experiments. My gratitute goes to my friend and colleque Ahmet Sedat Ayan, who went through all the steps of graduate journey in the University of Iowa with me. I am also grateful to my CMS colleagues, Erhan Gulmez, Jonathan Olson, Michael Miller, Ianos Schmidt, and Peter Bruecken for their invaluable contributions to the PMT tests station that we constructed. I owe thanks to my E781 collaborators, Peter Cooper, Maurizio Iori, Soon Yun, and James Russ for their guidance on SELEX analysis. Finally, I thank to my dearest Firdevs Duru for her constant support, encouragement, and love throughout my life outside physics.

ABSTRACT

This thesis consists of two parts: In the first part we describe the Photomultiplier Tube (PMT) selection and testing processes for the Hadronic Forward (HF) calorimeter of the CMS, a Large Hadron Collier (LHC) experiment at CERN. We report the evaluation process of the candidate PMTs from three different manufacturers, the complete tests performed on the 2300 Hamamatsu PMTs which will be used in the HF calorimeter, and the details of the PMT Test Station that is in University of Iowa CMS Laboratories. In the second part we report the Ξ_c^+ lifetime measurement from SELEX, the charm hadro-production experiment at Fermilab. Based upon 301 ± 31 events from three different decay channels, by using the binned maximum likelihood technique, we observe the lifetime of Ξ_c^+ as $427 \pm 31 \pm 13$ fs.

TABLE OF CONTENTS

LIST OF TABLES

LIST OF FIGURES

CHAPTER 1
LARGE HADRON COLLIDER AND CMS EXPERIMENT

1.1 The Large Hadron Collider

1.1.1 The Accelerator

The Large Hadron Collider (LHC) is being constructed at CERN in Geneva, Switzerland, and will be the largest hadron collider in the world when it is finished. It is scheduled to start operation in 2008. It will provide proton-proton collisions at a centre-of-mass energy $\sqrt{s} = 14$ TeV, which is 7 times higher than the $p\overline{p}$ collisions of Fermilab and it will be placed in the already existing LEP tunnel.

The LHC is designed to reach a luminosity of $\mathcal{L} = 10^{34}\ cm^{-2}s^{-1}$, this value is about 100 times more than the current luminosities reached by existing colliders. This *high luminosity scenario* will allow to collect approximately 100 fb^{-1} per year. For the first three years of operation LHC is planned to run at a luminosity of $\mathcal{L} = 2 \times 10^{33}\ cm^{-2}s^{-1}$, *low luminosity scenario*, and collect estimated 10 fb^{-1} per year for this period.

In addition to proton-proton collisions, LHC will provide heavy ion (lead) collisions with a centre-of-mass energy of 2.76 TeV per nucleon. This energy level is about 30 times higher than the Relativistic Heavy Ion Collider (RHIC) at the Brookhaven Laboratory.

The existing CERN facilities will be upgraded to provide the pre-accelerated protons for LHC. There will be series of existing machines which will be used to accelerate the protons to high energies; a Linac will bring them up to 50 MeV, a Booster up to 1.4 GeV, the PS up to 25 GeV and SPS up to 450 GeV, finally they will enter to LHC which is going to take them up to 7 TeV.

In LHC, two separate beam channels with opposite directions are required so as to accommodate the collisions between the same types of particles. The

Figure 1.1: Large Hadron Collider at CERN in Geneva, Switzerland.

Figure 1.2: Inside view of the LEP tunnels.

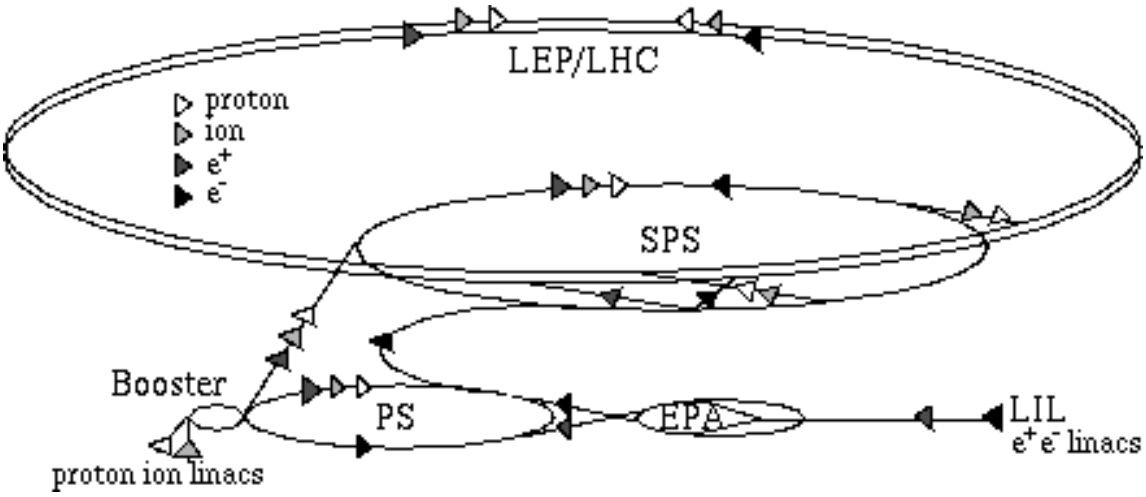

Figure 1.3: LHC and LEP injection chains.

two channels and their superconducting dipole magnets with corresponding coils will be inserted in a single cryostatic structure. Dipoles will operate at 1.9 K and will provide the magnetic field strength of approximately 8 Tesla. The boost will be provided by 400 MHz superconducting radiofrequency cavities with a voltage ranging from 8 to 16 MV/m. The main parameters of the LHC are summarized in the Table 1.1.

In every beam bunch there will be 10^{11} protons 7.5 cm long in the beam direction with 15μm transverse spread at the collision points. The *Luminosity* $\mathcal{L}$ depends on the number of particles at each beam (n1 and n2), the revolution frequency (f) and the widths which characterize the Gaussian transverse beam profiles in the horizontal and vertical directions (σ_x and σ_y respectively through the formula:

$$\mathcal{L} = f\frac{n_1 n_2}{4\pi\sigma_x\sigma_y} \tag{1.1}$$

The number of interactions N_i, corresponding to the process i with a cross section σ_i, is given by

$$N_i = \sigma_i \int \mathcal{L} dt \tag{1.2}$$

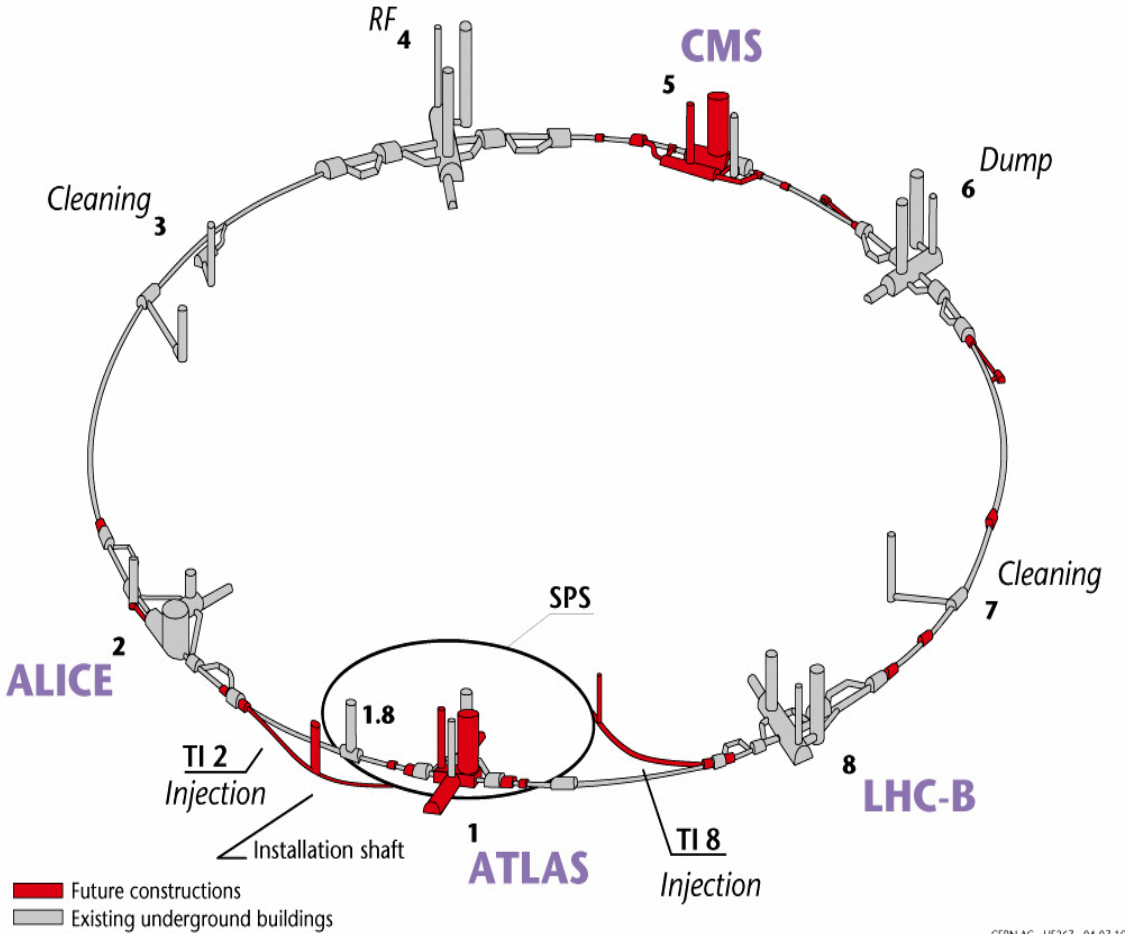

Figure 1.4: The LHC in the underground. The caverns for the CMS and ATLAS experiments are under construction at point 5 and 1 respectively. ALICE replaces the LEP experiment L3 at point 2, while LHCb replaces the LEP experiment DELPHI at point 8. The cavern of the LEP experiment ALEPH at point 4 will be used to house the RF system, and the cavern of the LEP experiment OPAL at point 6 will be used to install the beam dump.

$\int \mathcal{L} dt$ is also called *Integrated Luminosity*.

There will be four experiments located at the correspondence of four collision points of the LHC: CMS [1] and ATLAS [2] are multi-purpose detectors, designed to cover large domain of physics. ALICE [3] is dedicated to the Pb-Pb collisions and LHCb [4] is especially designed for b-physics.

Beam energy at collision	7 TeV
Beam energy at injection	450 GeV
Dipole field at 7 TeV	8.33 T
Design Luminosity	$1 \times 10^{34} cm^{-2} s^{-1}$
DC beam current	0.56 A
Bunch spacing	7.48 m
Bunch separation	24.95 ns
Number of particles per bunch	1.1×10^{11}
Total crossing angle	300μ rad
Luminosity lifetime	10 h
Energy loss per turn	7 keV
Total radiated power per beam	3.8 kW
Stored energy per beam	350 MJ
Filling time per ring	4.3 min

Table 1.1: LHC general parameters.

1.1.2 LHC Physics

The main goal of the LHC is to give the final answer to the question of the Higgs boson existence and to measure its properties with good precision. It is well known that the value of the Higgs mass is not predictable in Standard Model (SM).

On the other hand, it cannot be too heavy, otherwise the perturbative regime breaks down, and this leads to the upper bound on the Higgs mass of about 1000 GeV. Present measurements yield lower bounds of 114.1 GeV for the SM Higgs and 91.0 and 91.9 GeV for the light (h) and pseudoscalar (A) Higgs boson of the MSSM Model [5]. The LHC experiment will be able to observe a SM Higgs boson over its full mass range.

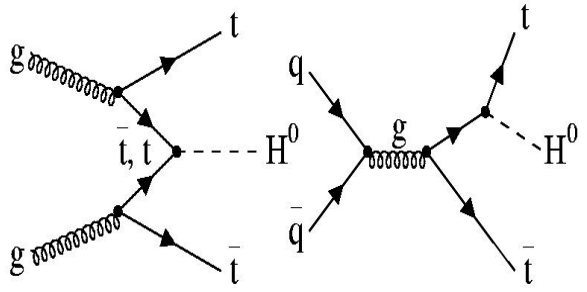

Figure 1.5: Principal Feynman diagrams for Higgs production at the LHC; $t\bar{t}$ associated production.

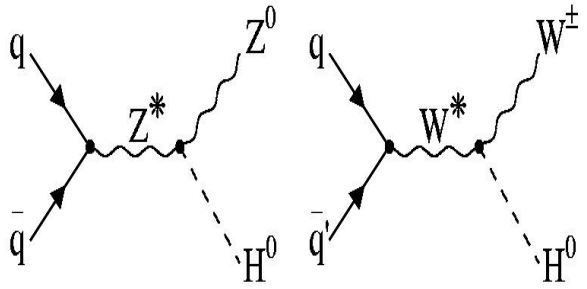

Figure 1.6: Principal Feynman diagrams for Higgs production at the LHC; W, Z associated production.

There are several reasons to believe that the Standard Model is not the ultimate theory of particle interactions but rather a low-energy approximation of some more fundamental theory. The first problem is the so-called *hierarchy problem*: the Higgs mechanism has little physical justification and leads to divergent radiative corrections to the Higgs boson mass unless fine-tuned cancellations are made.

Furthermore, there are a large number of free parameters in SM, which are not predicted by the theory. Grand Unification Theories solve this problem by assuming that $SU(3) \times SU(2) \times U(1)$ group of SM results from the spontaneous breaking of a higher symmetry.

Another apparent contradiction with the SM is the existence of some hints that the coupling constants of the electromagnetic, weak and strong interactions could unify into single value α_G at an energy scale of 10^{16} GeV [6].

All these problems can be solved in *Supersymmetry* (SUSY), a more general theory which predicts a universal boson-fermion symmetry. The SUSY predicts supersymmetric partners of the known particles and some new gauge bosons. The LHC will be able to reach the energy scale that these theories predict a new physics.

The high energy heavy ion collisions in LHC will help to understand the *quark-gluon plasma*, the phenomenon of formation of a deconfined state of hadronic matter.

Other than the new physics search the LHC will produce the known particles with a huge rate that allows us to make precision measurements on SM processes like top quark physics and b-quark physics.

1.2 CMS Detector

The Compact Muon Solenoid (CMS) is one of the four experiments which are designed to fulfill the physics requirements of LHC. The design goals of the CMS detector in the Letter of Intent [8] are summarized as follws: (i) a strong superconducting solenoid, to keep a compact design in a high magnetic field environment; (ii) a very good and redundant muon detection system; (iii) a high resolution electromagnetic calorimeter; (iv) a hadronic calorimeter of high granularity to perform E_T^{miss} measurements and jet identifications of high quality; (v) an inner tracking system to measure charged track momentum with high resolution.

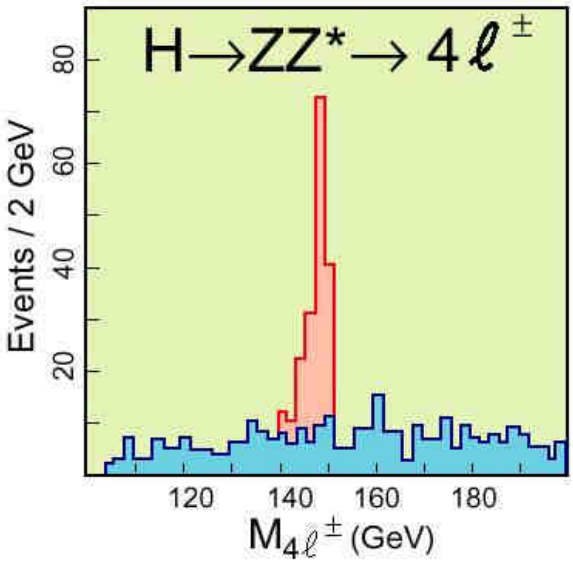

Figure 1.7: CMS simulation for $H \to ZZ^* \to l^+l^-l^+l^-$ and $m_H = 150$ GeV.

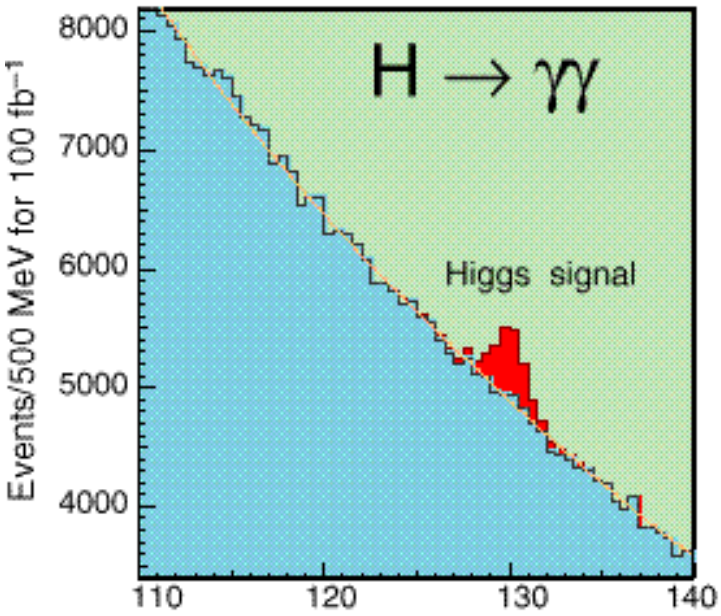

Figure 1.8: CMS simulation for $H \to \gamma\gamma$ ($m_H = 130$ GeV) before the background subtraction.

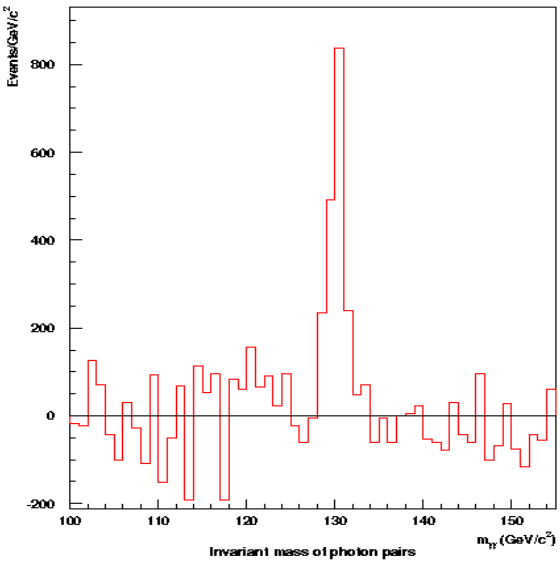

Figure 1.9: CMS simulation for $H \rightarrow \gamma\gamma$ ($m_H = 130$ GeV) after the background subtraction.

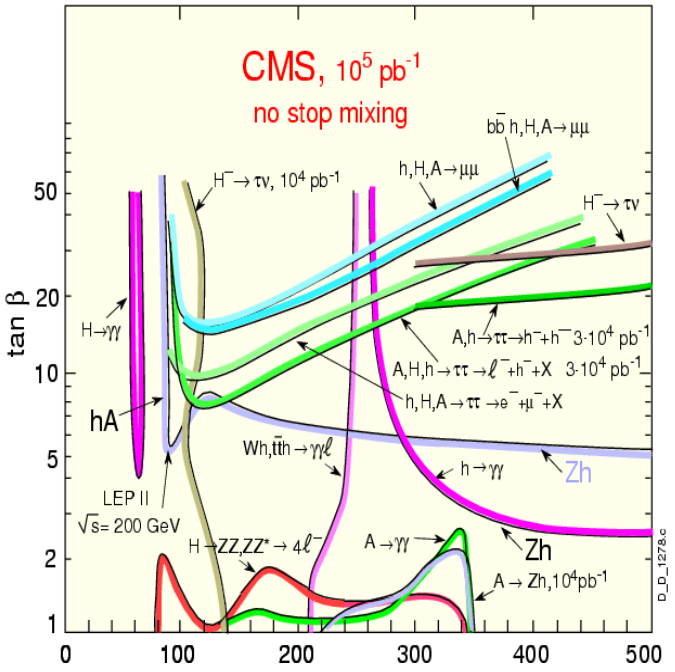

Figure 1.10: CMS 5 sigma significance contour plot for the MSSM Higgs sector in the $m_A - tan\beta$ plane.

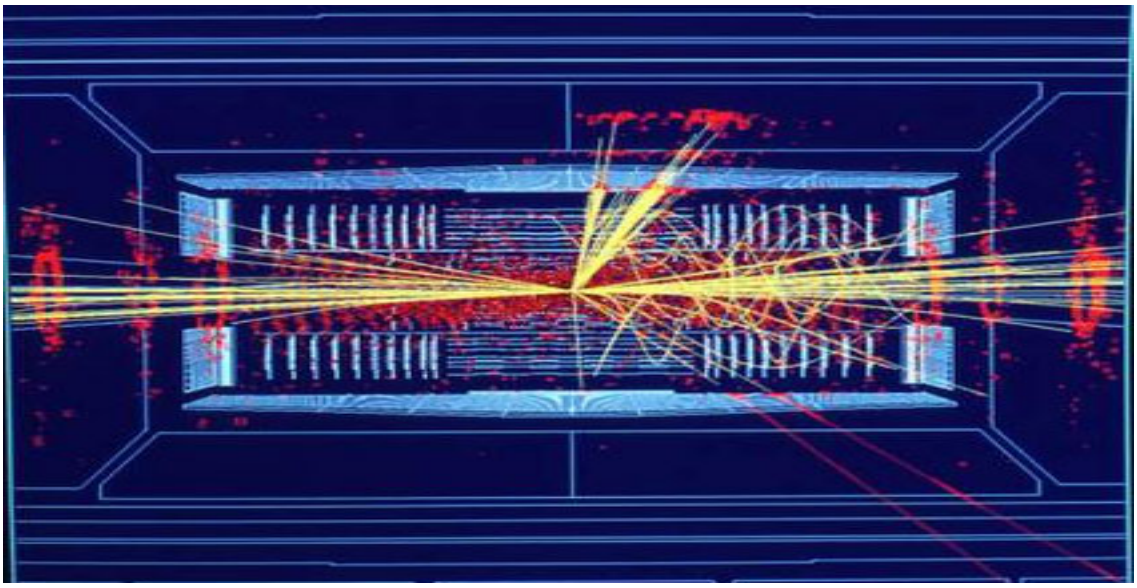

Figure 1.11: Event display at CMS Experiment.

The CMS detector (see Fig 1.13) has a cylindrical shape, with symmetry in the azimuthal angle. The dimensions are a length of 21.6 m (HF calorimeters excluded), a diameter of 14.6 m and a total weight of 14500 tons. The detector has an almost 4π solid angle coverage and there are four main subsystems; magnet, muon system, tracking and calorimetry. The central part of the detector is located in a 4 Tesla magnetic field which is parallel to the beam direction. In CMS reference frame: the x-axis points towards the center of the collider, the y-axis points upwards and the z-axis points along the beam. Often a pseudo-spherical coordinate system is used: in the transverse plane geometry is defined by the radius, r, and the azimuthal angle Φ with respect to y-axis, and the polar angle Θ with respect to z-axis, while instead of the polar angle the pseudorapidity η is used.

$$\eta = -ln(tan\frac{\Theta}{2}) \tag{1.3}$$

The pseudorapidity is an approximation of the rapidity y, given by

$$y = \frac{1}{2}ln\frac{E + p_z}{E - p_z} \tag{1.4}$$

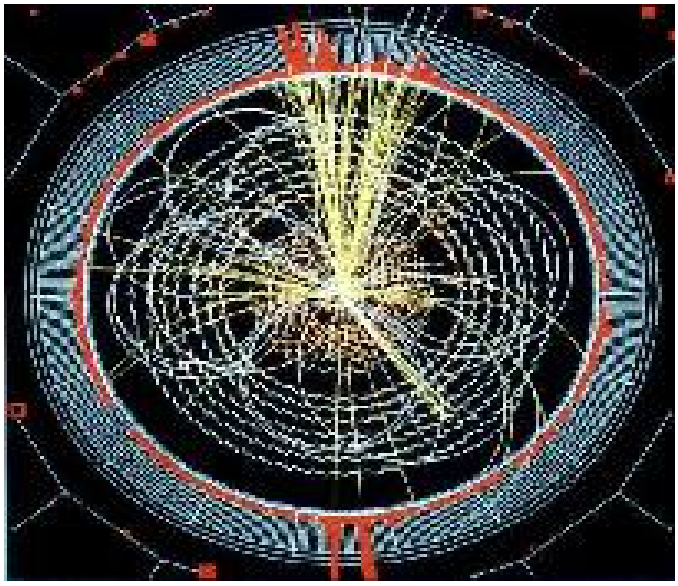

Figure 1.12: Higgs decay simulation in CMS.

where E and p are energy and momentum of a particle. The rapidity y is very useful in this respect as a boost along the z-direction only adds a constant to the rapidity and leaves distributions dN/dy invariant. The pseudorapidity is a good approximation of the rapidity for $p >> m$ and $\Theta >> 1/\gamma$.

1.2.1 Magnet

The magnet of the CMS detector (see Fig 1.13) is a long superconducting solenoid of length 13 m and inner diameter 5.9 m and it creates a uniform magnetic field of 4 T. The magnetic flux is returned via a 1.8 m thick saturated iron yoke which is instrumented with muon stations. The yoke consists of five barrel rings, each made of 3 iron layers, and two end-caps. The favorable aspect of the ratio of the solenoid allows efficient muon detection and measurement up to rapidity of 2.4 without the need of forward toroids. Thus the muon spectrometer uses single magnet, simplifying the detector design. The inner coil diameter is large enough to accommodate the tracker and the calorimeters. Since the magnet is the main element of CMS in terms of size, weight, and structural rigidity, it is used as the

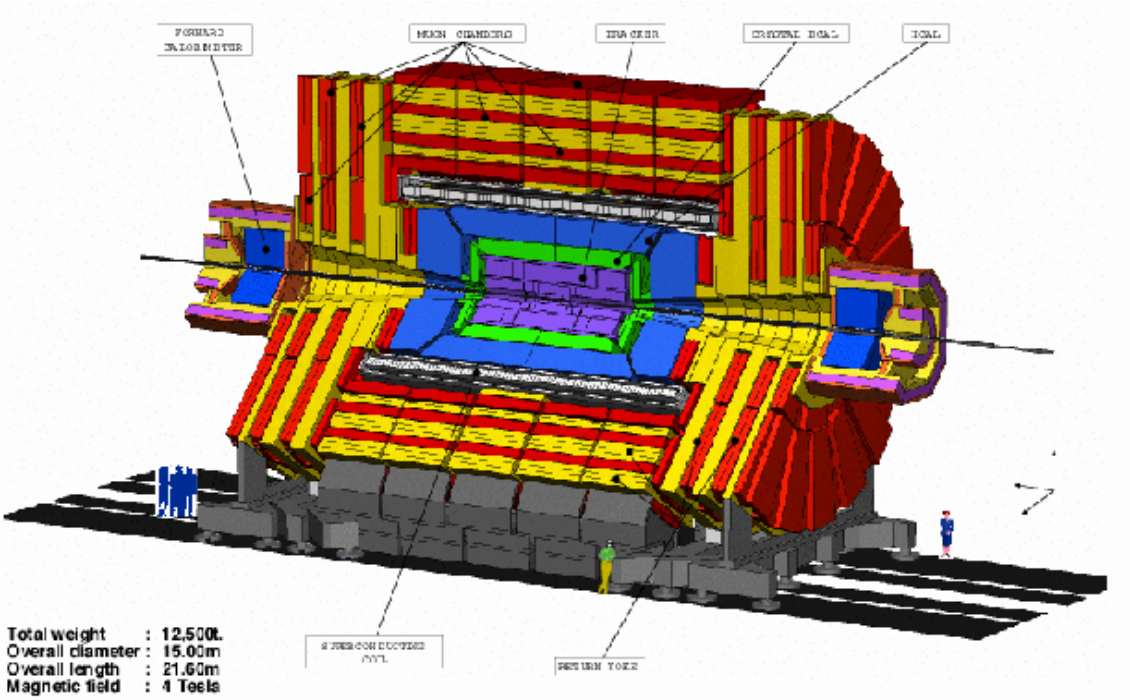

Figure 1.13: Three dimensional view of the CMS Detector.

principal structural element to support all other barrel detector components [1].

1.2.2 Muon System

A good muon identification and momentum measurement system are the main concept of the CMS experiment. The muons offer a clean signature for a wide range of processes: they are basic for Higgs and SUSY searches, not only for discoveries but also for extracting their properties. Muon identification relies on the high penetrating power of the muons: the muon detector is placed outside the magnetic filed, after the calorimeters, which are supposed to stop all other charged particles. The muon system plays an important role for triggering interesting events, so it must be composed of very fast detectors, delivering a signal that can be associated to a single bunch crossing, and capable of providing a fast estimate of the muon transverse momentum in order to allow P_t cuts at the trigger level. In the CMS detector a muon sees four muon stations over most of the solid angle (see Fig

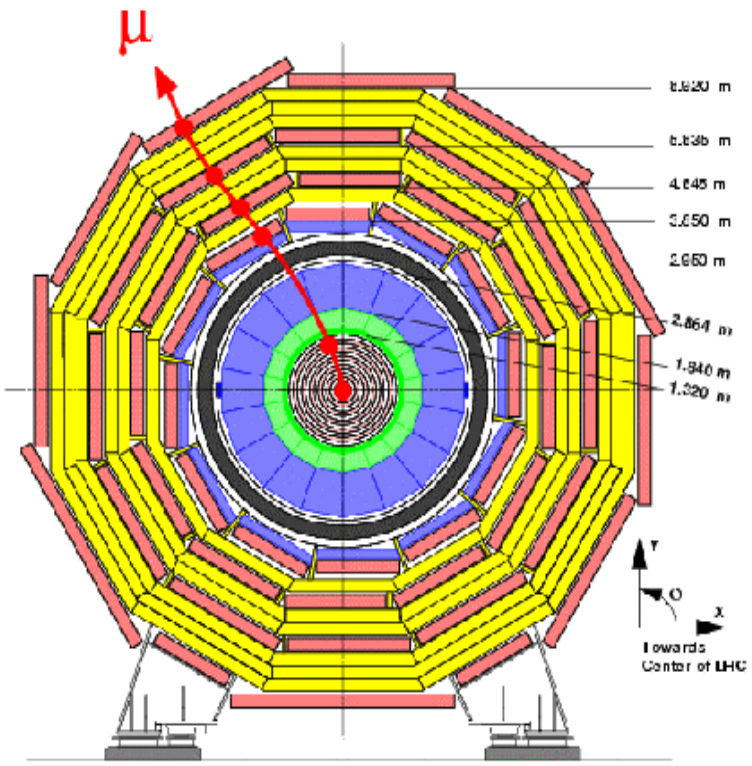

Figure 1.14: Transverse view of the CMS detector.

1.14). Each of the four barrel stations (MS1 to MS4) consists of twelve planes of aluminum drift tubes (DTs), arranged in twelve azimuthal sectors, such that there are no cracks pointing to the primary vertex 1.14. The endcap muon system also consists of four muon stations MF1 to MF4. Each station consists of sectors of CSCs overlapping in azimuth to maintain full coverage. The two stations MF1A and MF1B have been added to ensure that all muon tracks traverse four stations at all rapidities, including the transition region between the barrel and the endcaps ($1 < |\eta| < 1.5$) (see Fig 1.16).

Efficient muon detection is guaranteed up to $|\eta| = 2.4$ for $P_t > 4GeV/c$. The acceptance of the hadronic endcap HF has been extends up to $|\eta| = 3$ to allow the insertion of a thicker conical iron structure. This cone significantly reduces the background rate in the four forward stations (MF1 to MF4). It can also support the

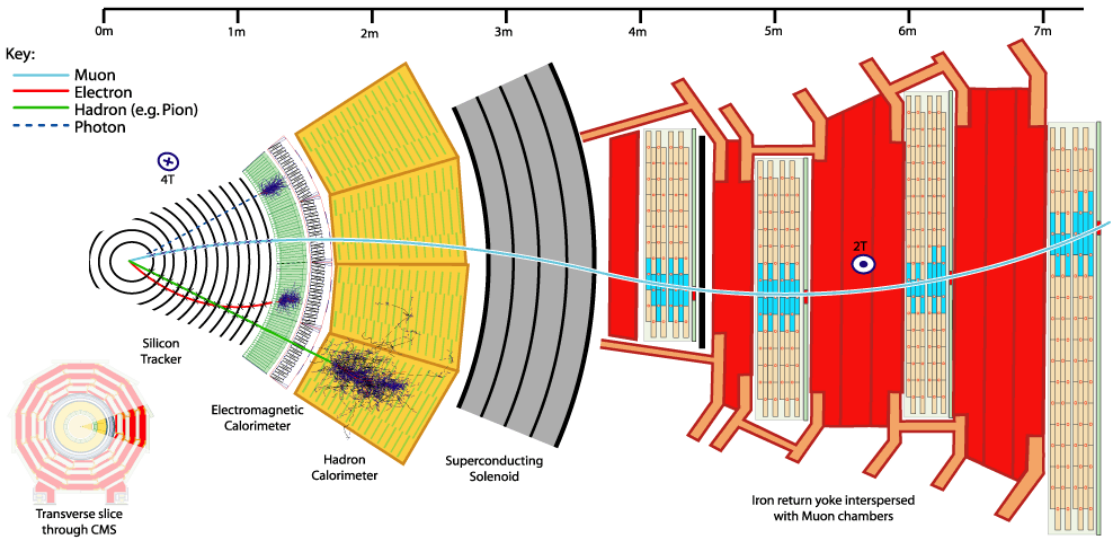

Figure 1.15: Event trajectories in the CMS detector.

endcap calorimeters (HF and EF) without cutting into the azimuthal acceptance.

1.2.3 Tracking

An important part of the CMS physics program relies on the capability of the detector to reconstruct charged particle tracks, and measure their momentum and impact parameters with high resolution. This is crucial for heavy quark physics and b-tagging.

CMS tracking system is capable of reconstructing isolated high P_t tracks with an efficiency of better than 95 percent, and high P_t tracks within jets with an efficiency of better than 90 percent over the rapidity range $|\eta| < 2.6$.

The momentum resolution required for isolated charged leptons in the central rapidity region is $\Delta P_t/P_t = 0.1P_t$ where P_t is in TeV/c. This will allow the measurement of the lepton charge up to $P_t = 2$ Tev/c. This will also allow frequent in situ calibration of every cell of the crystal electromagnetic calorimeter, needed to maintain the high-energy resolution of the calorimeter, using the high rate of precisely measured electrons from W and Z decays. The silicon pixel detectors close

to the interaction vertex is designed to give 20 μm resolution in the transverse plane and 100 μm in the z direction. The solid-state pixel and microstrip detectors will provide the granularity and precision on pattern recognition at high luminosities [1].

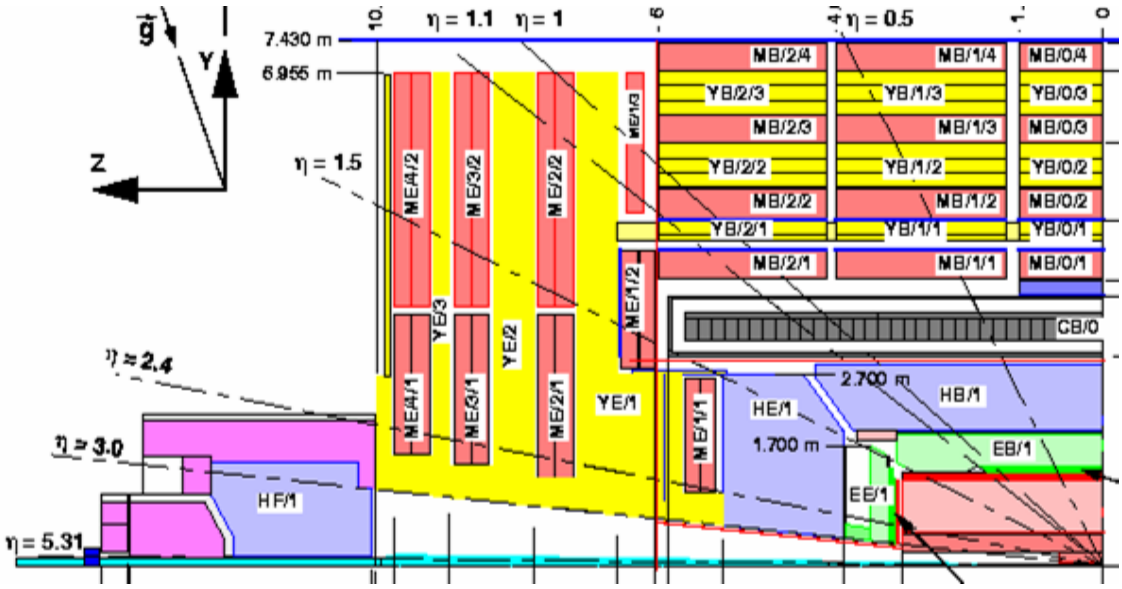

Figure 1.16: Longitudinal view of the CMS detector.

1.2.4 The Electromagnetic Calorimeter (ECAL)

The high resolution PbWO4 (Lead Tungstate Crystals) Electromagnetic calorimeter (ECAL) (see Fig 1.17) is designed to measure the energies of electrons and photon with high precision. The electromagnetic calorimeter will play a very important role in the search for the Higgs, by measuring the photon decay mode ($H \rightarrow \gamma\gamma$) for $m_H < 150$ GeV, and by measuring electrons and positrons from the decays of W's and Z's coming from the $H \rightarrow ZZ^*$ and $H \rightarrow WW$ decay chains for 140 GeV $< m_H <$ 700 GeV. For these physics goals, the energy resolution has to be very good, and the crystals should give fast response to make the ECAL information available at the trigger level. Since the detector is located at high radiation area

the material has to be radiation hard, too. The PbWO4 has high density, and small Molieère radius which allows to have narrow showers, so the scintillating process is fast, 20 ns, in addition the lead tungstate is radiation hard. The ECAL is composed of barrel and end-cap parts. The barrel part covers $\eta < 1.48$ range, with crystals of 26 radiation length depth. The end-cap part covers up to $\eta < 3.0$ with crystals of 25 radiation length depth. To improve the $\pi^0 - \gamma$ separation a preshower will be placed in the pseudorapidity region $1.65 < \eta < 2.6$. The CMS ECAL will hold more than 8×10^5 crystals. Because of the strong magnetic field it is not possible to use the photomultipliers in ECAL. For the barrel region silicon avalanche photodiodes, and for the end-cap radiation hard vacuum phototriodes are used. The energy resolution for ECAL can be parameterized as:

$$(\frac{\sigma}{E})^2 = (\frac{a}{\sqrt{E(GeV)}})^2 + (\frac{\sigma_n}{E(GeV)})^2 + c^2 \tag{1.5}$$

where a is the stochastic term, including the fluctuations of the shower containment as well as the contributions from photo statistics, σ_n is the noise term, including the electronic noise and pile-up effects, and c is the constant term. At high luminosity the contributions of the different terms are expected to be $a = 2.7\%, \sigma_n = 210$ MeV, c=0.55% in the barrel and a=5.7%, $\sigma_n = 915$ MeV, c=0.55% in the end-caps.

1.2.5 The Hadronic Calorimeter (HCAL)

The Hadronic Calorimeter (HCAL) is the outermost detector placed inside the magnet coil. The HCAL surrounds the ECAL (Fig.1.17) and acts in conjunction with it to measure the energies and directions of particle jets, and to provide hermetic coverage for measuring missing transverse energy. These measurements will play an important role in the discovery of the Higgs boson in the high mass range and in the discovery of supersymmetric particles. In order to achieve good missing energy resolution, a hermetic calorimetry coverage to $|\eta| < 5$ is required.

The HCAL consists of a barrel (HB), endcap (HE), and forward (HF) parts. The pseudorapidity range of $|\eta| < 3.0$ is covered by the barrel and the endcap HCALs which sit inside the 4 T field of the CMS solenoid [1]. The HF calorimeter is placed around the beam-pipe outside the muon system and extends the coverage up to $|\eta| < 5.3$. The HB and HE are sampling calorimeters consisting of 50 mm thick copper absorbers interleaved with 4 mm thick plastic scintillator tiles that are read out with wavelength shifting fibers. The light is detected by hybrid photodiodes. The HB is made of two half-barrels each of 4.3 meter length. The HE consists of two large structures, situated at each end of the barrel detector and within the region of high magnetic field. Because the barrel HCAL inside the coil is not sufficiently thick to contain all the energy of high energy showers, additional scintillation layers (HOB) are placed just outside the magnetic coil. The full depth of the combined HB and HOB detectors is approximately 11 absorption lengths.

The achievable energy resolution is given by $\sigma_E/E = 65\%/\sqrt{E} + 5\%$ in the barrel and by $\sigma_E/E = 85\%/\sqrt{E} + 5\%$ in the endcaps and $\sigma_E/E = 100\%/\sqrt{E} + 5\%$ in the forward part, where E is measured energy in GeV.

1.2.6 The Hadronic Forward (HF) Calorimeter

There are two HF Forward Calorimeter units, one at each end of CMS. Each unit has an active radius of 1.4m and consists of iron absorbers, fibers embedded into the absorbers, and phototubes. The embedded fibers will have two different lengths to differentiate between shower processes. Longer fibers (1.65 m) will provide light from EM and hadronic showers in the absorber. Shorter fibers (1.43 m) will only see the hadronic showers[9]. The long and the short fibers are read out by separate PMTs. The iron absorber length (1.65 m) is 10 nuclear interaction lengths. The two HF calorimeters in CMS detector cover the pseudorapidity range from 3.0 to 5.0.

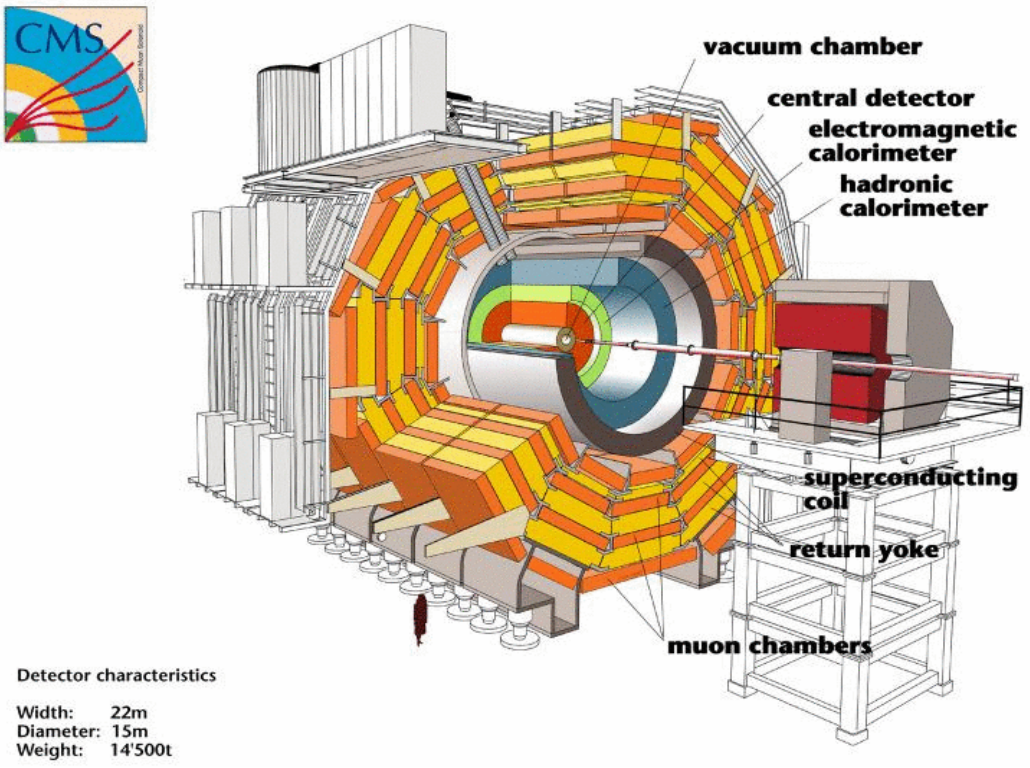

Figure 1.17: Another three dimensional view of the CMS Detector.

The HF calorimeters are located 11 m away from the interaction point as shown in Fig 1.17 . The HF calorimeter improves the measurement of the missing transverse energy and enables very forward jets to be identified and reconstructed. These jets are distinguishing characteristic of several important physics processes; in the case of heavy Higgs production, they materialize through WW and ZZ fusion. In the case of slepton, chargino and neutralino searches, they are background signatures.

The Large Hadron Collider will be operating at a luminosity of 10^{34} cm^{-2} sec^{-1}, and the average particle multiplicity at the IP per crossing is about 5700 with an RMS value of 1200. This corresponds to a rate of 2.3×10^{11} sec^{-1}, equivalent to 280 particles/crossing/rapidity unit. $4.5 < |\eta| < 5.0$ region will experience a flux of about 6.0×10^{6} cm^{-2} sec^{-1} and absorbed doses will reach about 100 Mrad/year. Therefore, the detectors must be able to survive in an exceptionally high radiation

field. The CMS experiment has chosen the quartz fibers as the active material for the HF regions because the high-purity quartz is known to be very radiation-hard [10].

A calorimeter with optical quartz fibers embedded into an absorber matrix was proposed by HCAL group [11] for producing extremely fast signal as well as radiation hardness. A lot of simulation and test beam studies that have been made on quartz fiber calorimeter prototypes by CMS HCAL group, which includes University of Iowa CMS group. Those studies can be summarized as follows: testing the response of the prototype CMS hadron calorimeter to different beams [12], testing the quartz fiber calorimeter prototype composed of a single active section with a passive absorber in front of it [13], testing the prototype for the detection of different particles (electron, photon, hadrons and hadron-jets) [14] [15], calculation of resolution and reconstruction efficiencies by Monte Carlo simulations [16] [17] [18], and the radiation damage studies on the absorber material and on the fibers [19].

Being sensitive to the hard particle core of the shower has benefits. The distribution of the relativistic particles in the shower shows a narrow profile, even narrower than its corresponding Molière radius. It is also shorter than the full shower profile. Hence using Cherenkov-radiation-in-quartz-fiber method enables us to have a more compact design for the HF Forward Calorimeter. This type of shower detection is fast since the tail in the time distribution is caused by slower particles that do not produce Cherenkov radiation. These features of the calorimeter have been confirmed in our prototype tests at CERN[9].

Each HF module is divided into 18 wedges. Every wedge consists of about 2400 stacked parallel iron plates each with 5mm thickness. Grooves are machined lengthwise along each plate and quartz fibers are inserted in these grooves. These groves are separated from each other by 5mm both vertically and horizontally. Short and long fibers are placed in each tower in alternate grooves. All the long

fibers from a tower will be put together in a bundle and attached to a 42 cm light guide, a photomultiplier tube will be attached to the other end of the light guide. Similarly, all the short fibers from a tower will be attached to another light guide and photomultiplier tube. There will be 48 PMTs per wedge. Reliable operation of the HF Forward Calorimeter depends mostly on the PMTs. In the next chapter we are describing the evaluation procedure and the tests we performed on the candidate PMTs for the HF calorimeter.

CHAPTER 2
PHOTOMULTIPLIER TUBE (PMT) EVALUATION FOR THE CMS HF CALORIMETER

2.1 Introduction

The HF Calorimeter of CMS experiment samples particle showers in an iron absorber by detecting the Cherenkov light. The Cherenkov light produced in the fibers will be detected and measured with PMTs. In HF calorimeter the PMTs will operate in a temperature-controlled environment, and be inside individual magnetic shields to protect them from a moderate magnetic field. Due to the large number the PMTs must be small in diameter. The light from the calorimeter fiber will be in the 300-600 nm range. So the photocathode must have good quantum efficiency in that wavelength region. The PMTs will also be in a radiation environment, and they should not appreciably deteriorate over a 10 years lifetime of operation. As in all calorimeters, a premium is placed on the short-term and long-term gain stability of the tubes as functions of time and average anode current; it is also important that the tubes have large linear dynamic range at all gains.

Three PMT manufacturers, Hamamatsu, Photonis (Philips), and Electron Tubes (EMI), provided us with candidate tubes that met the minimum requirements for the HF calorimeter. These candidate PMTs were tested for timing, gain, dark current, linearity and single photoelectron resolution.

Overall evaluation of the candidate PMTs was based on the results of all these tests. Hamamatsu R7525HA PMT was chosen as the optimum choice for the HF calorimeter. The evaluation procedure for the PMTs is explained and the results are summarized in this chapter.

2.2 HF Requirements for PMTs

Specifications of the PMTs to be used in the HF calorimeter are listed in Table 2.1. The PMT specifications are meant to address the various issues in the construction and operation of the HF calorimeter. Operating conditions in the LHC, the mechanical construction of the HF calorimeter, and the way the fibers generate Cherenkov light and transport this light to the PMTs determine some of the physical parameters of the PMTs needed in the HF. Location and the available volume for the PMTs in the HF calorimeter define the size of the PMTs. The amount of radiation expected at the HF location and the environmental conditions, such as temperature and humidity, put limitations on the size, packaging, and materials used in manufacturing the PMTs. The intensity and the wavelength of the Cherenkov light generated in the fibers will guide us in selecting the window material and the minimum quantum efficiency. These initial requirements are listed in the top part of Table 2.1. The second half of the table lists those parameters that are related to the operation of the HF specifically.

2.3 Evaluation Procedure

Manufacturers were asked to propose specific PMTs meeting the requirements summarized in Table 2.1. The suggested PMTs were tested under varying conditions to determine the dynamic range of the operating parameters. A PMT that was low-cost and conformed well to the requirements over a wide range of conditions was selected.

Three manufacturers, Hamamatsu, Photonis, and Electron Tubes, responded and provided us with candidate PMTs. These are listed in Table 2.2.

These PMTs were tested for the operational requirements, specifically; the timing characteristics (anode pulse width, rise-time, transit-time, and transit-time

Basic Requirements	
Window Material	Borosilicate glass
Effective Photocathode Diameter	22-28 mm, head-on
Quantum Efficiency	$> 15\%$ (400-500 nm)
Photocathode Lifetime	> 200 mC
Stability	$< \pm 3\%$ within any 48 hr. period
Envelope	opaque and HV conductive coating

Operational Requirements	
Anode Current vs Position	$< 20\%$ variation with 3 mm spot scan
Gain	10^4 to $10^5, 10^5$ at less than 0.75 x V_{KA}(max)
Single Photoelectron Resolution	50% or better (rms/mean of SPE peak)
Pulse Linearity	± 2 percent for 1-3000 p.e.
Anode pulse rise-time	< 5 ns
Transit Time	< 25 ns preferred
Transit Time Spread	< 2 ns preferred
Pulse width	< 15 ns FWHM
Gain (1/2)-lifetime	> 1500 C
Average Cathode Current	< 1 nA (g = 10^4)
Average Anode Current	< 10 μA (g = 10^4)
Anode Dark Current	< 2 nA (g = 10^4)

Table 2.1: Summary of the specifications for the HF PMTs.

spread), gain, dark current [20], linearity [21], single photoelectron resolution spectrum [22], and spatial uniformity of the photocathode surface [23].

Most of the parameters were measured at a nominal PMT gain of $10^4 - 10^5$, since the HF PMT readout system was designed to accept low amplitude signals.

Manufacturer	Type	Serial Number	Base used
Hamamatsu	R7525HA	ZC9898	Resistive
Hamamatsu	R7525HA	ZC9900	Resistive
Hamamatsu	R7525HA	ZC9903	Resistive
Hamamatsu	R7525HA	ZC9957	Resistive
Photonis	XP3182/D1	99023	Resistive
Photonis	XP3182/D1	99021	Resistive
Photonis	XP2960	12031	Resistive
Photonis	XP2960	12033	Resistive
Electron Tubes	D843WSB	102	Cockroft-Walton
Electron Tubes	D844WSB	103	Cockroft-Walton

Table 2.2: Candidate PMTs and the manufacturers.

With the expected Cherenkov light intensity and the required photocathode quantum efficiency, this gain will be sufficient to generate an output pulse compatible with the readout system requirements of the HF calorimeter.

Since there was more than one sample PMT for some of the PMT types, all ten of the PMTs were not always tested. A representative sample of measurements for each PMT type was considered sufficient. All the tests were performed on all the PMT types even if a specific PMT did not perform in accordance with the HF requirements in a previous test.

2.3.1 Timing Measurements

The time response of the PMTs, including pulse width, rise time, transit time and its spread, are determined together in the same setup. The transit time is the travel time of the photoelectrons from the photocathode to the anode via

the dynodes. This transit time depends on the voltage applied to the PMT. It also depends indirectly on the electrode structure, since the electrode structure determines the electric field applied to the electrons.

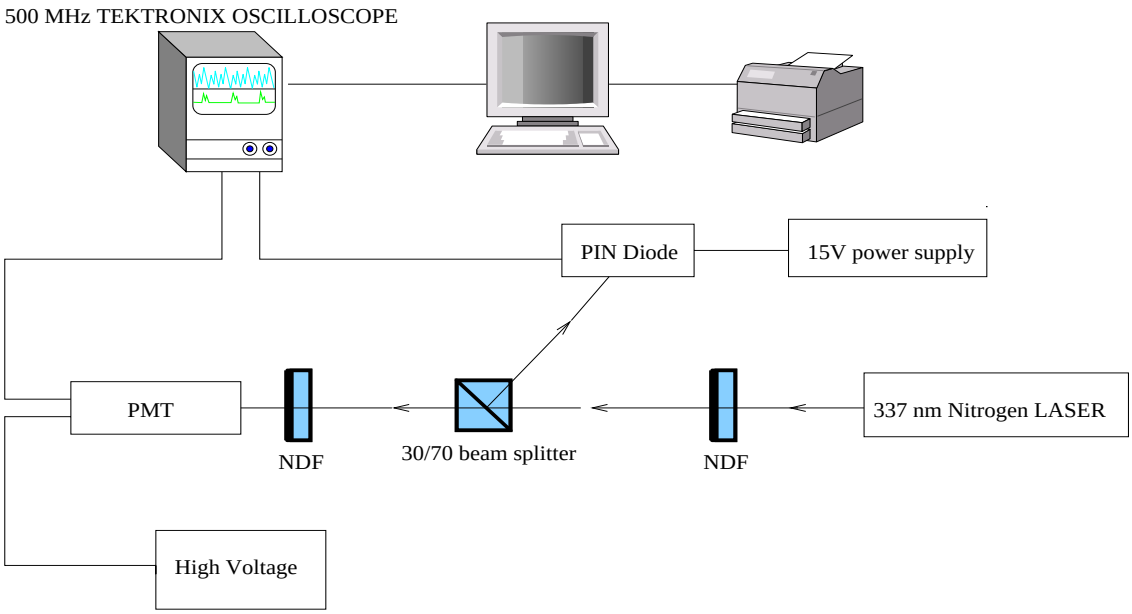

Figure 2.1: Test setup for timing measurements.

Transit time variations between different events are caused by different impact points on the photocathode. Fast PMTs are designed to minimize these variations [24][25]. However, there is still some fluctuation in the transit time. These fluctuations produce a transit time spread (TTS).

Other timing characteristics, such as pulse width and rise time, are also important quantities. Pulse width is the FWHM of a pulse. Rise time is defined as the time for the signal to go from 10% to 90% of its maximum amplitude. Total time for the detection process would be the sum of the transit time and the pulse width.

In our timing measurements (see Fig. 2.1), a 337 nm nitrogen laser (LSI VSL-337 ND) was used as the light source. The laser pulse was sufficiently sharp so that its contribution to various measurements was negligible. The laser beam passed

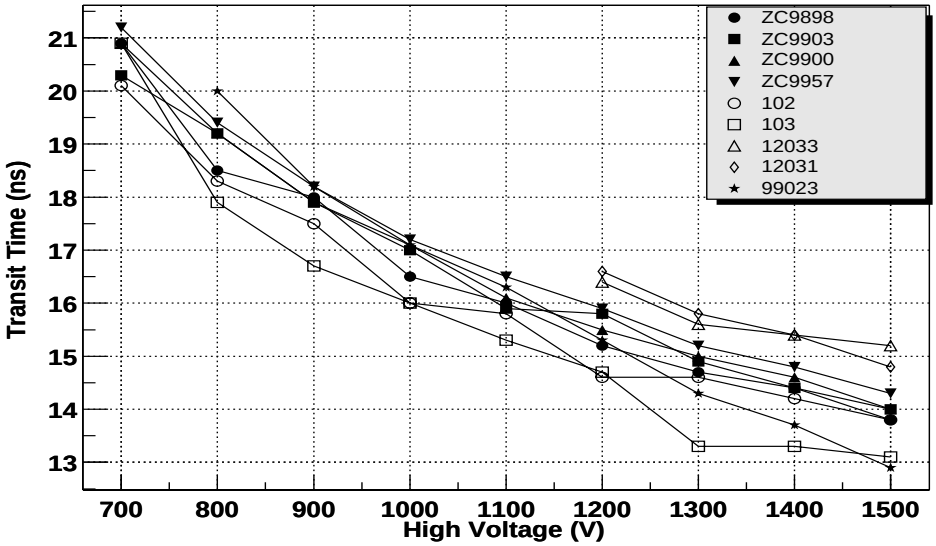

Figure 2.2: Transit times of the candidate PMTs as a function of high voltage.

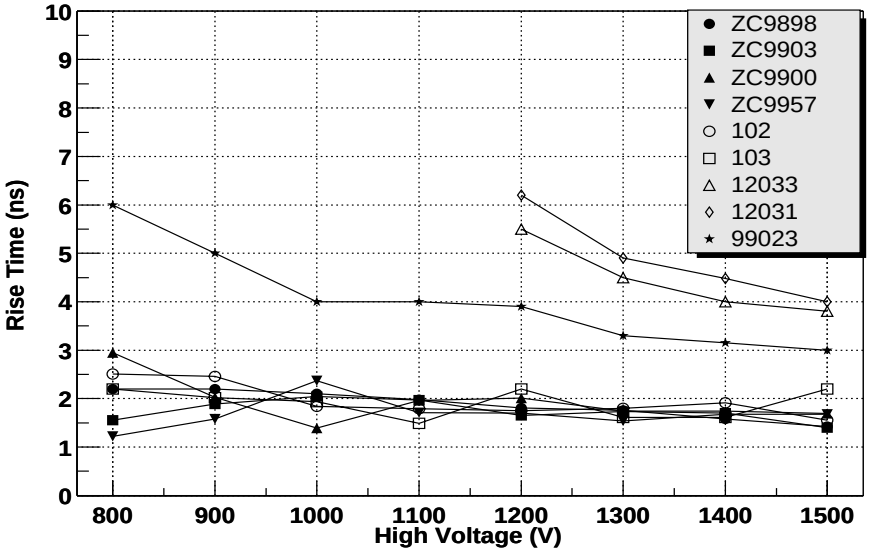

Figure 2.3: Rise times of the candidate PMTs as a function of high voltage.

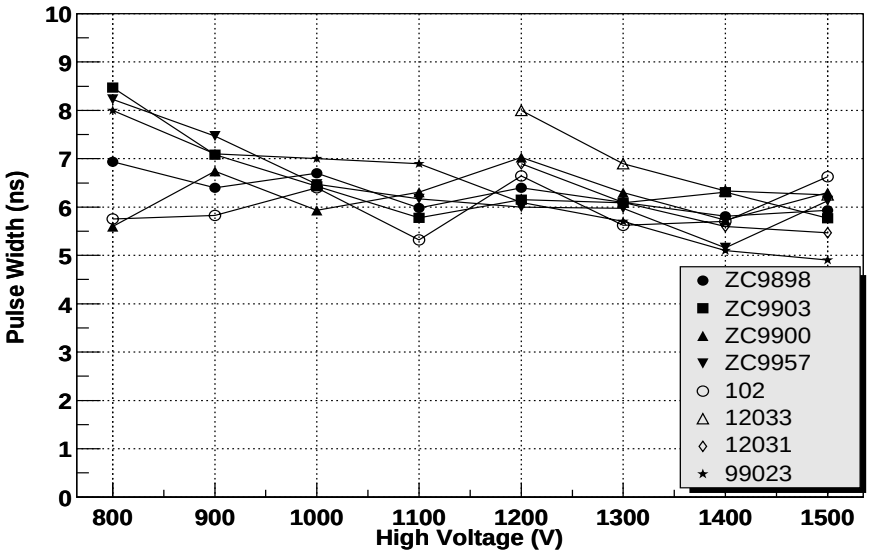

Figure 2.4: Pulse widths of the candidate PMTs as a function of high voltage.

through a 30/70 beam splitter and a neutral density filter. The transmitted light went to the PMT assembly and the reflected beam was directed into a PIN diode through another neutral density filter. The PIN diode signal was used as a reference for the transit time measurement and also for triggering the oscilloscope. By observing the PIN diode output in coincidence with the PMT signal on a 500 MHz Tektronix TDS-780 digital oscilloscope, we could measure the leading edge rise time, pulse width, and the transit time of the PMT. Results are shown in Figures 2.2, 2.3, and 2.4.

The transit time results showed good agreement with specifications. The transit times of the PMTs were in the 20 ns range at low gain. With increasing gain (voltage) the transit time values decreased to the 14 ns range (see Fig.2.2). Transit time spread (TTS), as measured with the digital oscilloscope, was less than 2 ns for all the PMTs.

The pulse width measurements showed us that the 15 ns limit set by the CMS HF requirements was not hard to reach. All the results were in the 5-8 ns range

(see Fig. 2.4).

Although almost all the PMTs were within the limits defined by the CMS HF specifications, Hamamatsu and Electron Tubes (see Fig.2.3) had shorter rise times; less than 2 ns. Photonis(XP3182/D1) PMT was right at the limit (5 ns), but the other two Photonis PMTs had rise times longer than 5 ns.

Overall, Hamamatsu and Electron Tubes had comparable timing characteristics suitable for the HF, but Photonis did not.

2.3.2 Dark Current

Dark current can be caused by various processes, such as, thermionic emission from the photocathode and the dynodes, leakage from the electrodes inside the PMT or the outside connectors, and field emission current, etc. Usually, most PMTs are designed and manufactured to minimize the effects of these processes. Dark current values for the HF PMTs should be as small as possible to maximize the signal/noise ratio.

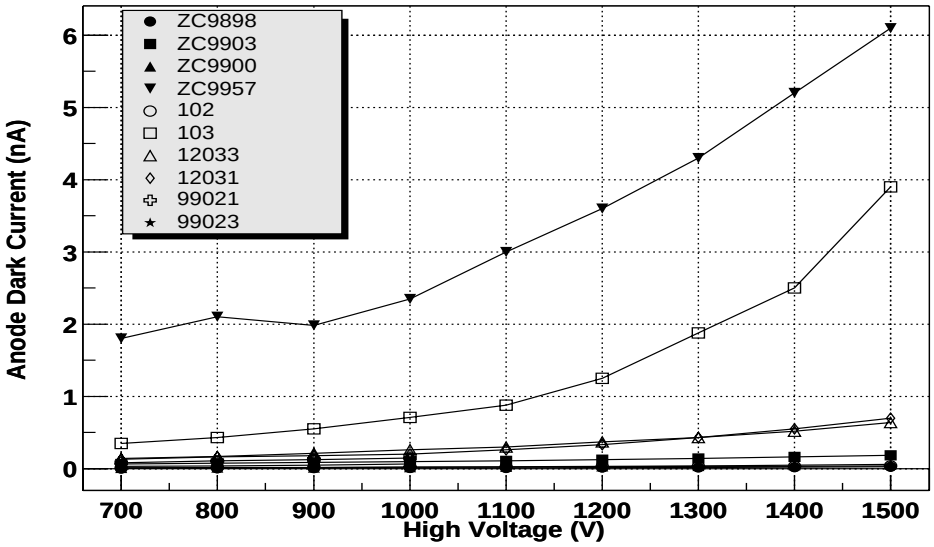

Figure 2.5: Anode dark current values of the candidate PMTs as a function of high voltage. Most of these results are within limits defined by the CMS HF specifications.

For dark current measurements, the PMTs were kept in a light-tight dark box for 30 minutes prior to data taking. Between the high voltage changes, we waited for the PMT output to stabilize. Dark current values were read by a picoammeter (Keithley 486).

Anode dark current measurements for almost all the PMTs were under 1nA (see Fig.2.5), except for one of the Hamamatsu PMTs (ZC9957) and the Electron Tubes (D844WSB) PMT. The former was an example of the tubes that would be rejected, the latter had high dark current possibly due to its high gain. Dark current measurements were not conclusive in our comparison.

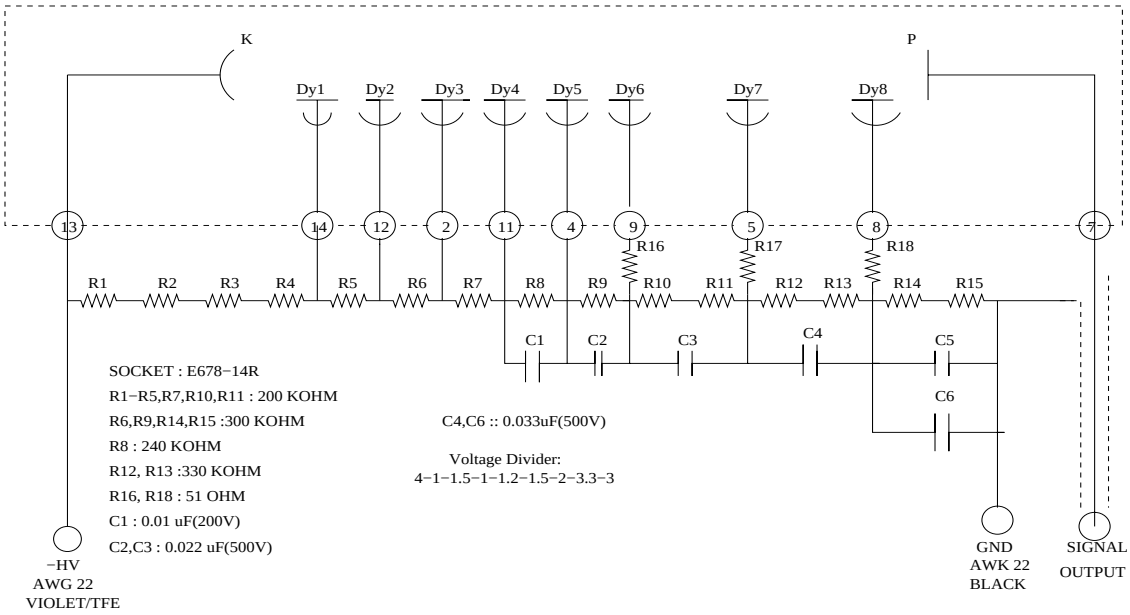

Figure 2.6: Block diagram of Hamamatsu E2624MOD resistive base.

2.3.3 Current Gain

The HF calorimeter dynamic range requires that the gain of the PMTs should be set to low values. The expected Cherenkov light intensity generated in quartz fibers and the input requirements for the readout electronics limit the PMT gain to be adjusted to the 10^4 range. However, the PMTs should still meet the requirements

set by the HF Forward Calorimeter design even if they are operated at such lower gains. Also, gain uniformity is imposed by the proposed HV distribution method. There will be 48 PMTs for each wedge in the HF calorimeter to optimize the cost. These 48 PMTs will be divided into two sets. The high voltage for each set of 24 PMTs will be provided by one HV power supply. All of the PMTs in the set should have the same gain to within a few percent.

Since the gain of a PMT is defined as: $G = I_a/I_k$, where I_a is the anode current due to a cathode photocurrent I_k, both anode and cathode currents need to be measured. For this purpose special resistive bases were manufactured for PMTs so that the current from the first dynode, i.e., the cathode current could be determined. All the dynodes and the anode were shorted together and the HV was applied between the cathode and the first dynode. A 100 kΩ resistor was added to limit the current. Anode currents were measured by using the regular resistive bases. Anode and cathode currents were corrected by subtracting the corresponding dark currents. Currents were read by the same picoammeter. A tungsten light bulb was used as a DC light source. Gain measurements were also performed in the light-tight dark box.

Gain values were expected to be similar for the candidate PMTs, because they were all 8-stage tubes, had the same cathode material, and were almost the same size except D844WSB, which was shorter than the others. The results showed that D844WSB PMT had much higher gain and quantum efficiency than the other PMTs (see Fig.2.7). The other candidate tubes were within the required limits.

Both Electron Tubes PMTs resulted in cathode dark current values which were much higher than anode dark current values. The manufacturer explained this anomaly as leakage current due to the ceramic they used in the PMT. All the other candidate PMTs had negligible cathode dark current values as expected. Photonis XP2960 PMT was not included in these measurements since we did not have the

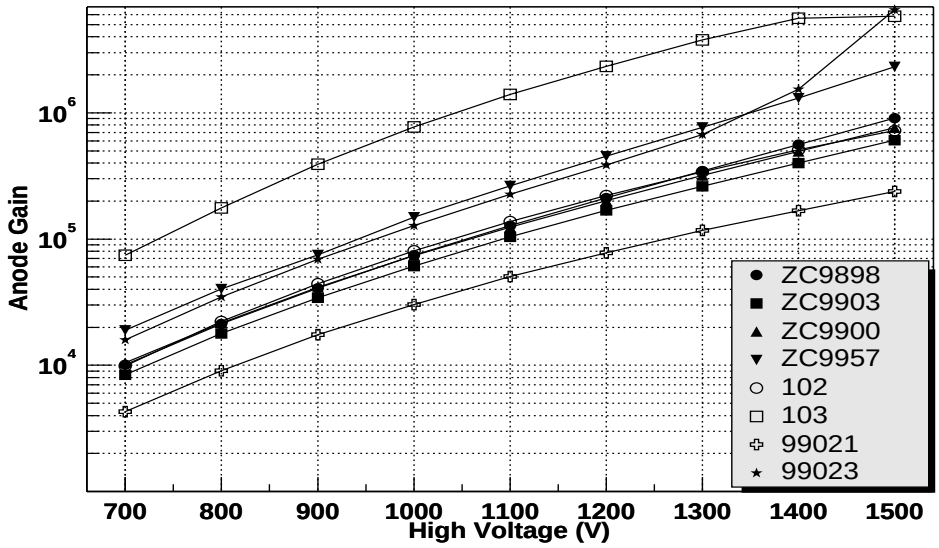

Figure 2.7: Gain measurements of the candidate PMTs as a function of high voltage.

modified bases for them to measure the cathode current.

2.3.4 Single Photoelectron Spectrum

The ideal electron multiplier system should provide a constant gain for all fixed energy electrons. But, in practice this is not possible because of the statistical nature of the secondary emission process. Single electrons of the same energy entering the system will produce different numbers of secondary electrons resulting in fluctuations in gain. This may be further amplified by variations in secondary emission factor over the surface of the dynodes, differences in transit time etc. A good measure of extent of the fluctuations in a given multiplier chain is the *single electron spectrum*. This is the spectrum of the photomultiplier output pulse heights resulting from single photoelectrons. This distribution essentially gives the response of the electron multiplier and can be measured by illuminating the PMT with a very weak light source such that the probability of more than one photoelectron entering the multiplier at the same time is small [26].

Single Photoelectron Spectrum can be described by several parameters:

- The amplitude corresponding to the centroid of the spectrum. This is, of course, the *mean* amplitude; if the secondary emission were free from any fluctuation, all pulses would have that amplitude.

- Peak-to-Valley (P/V) ratio. With a secondary emission coefficient for the first dynode of at least 6 to 8, single photoelectron spectrum will show a peak and a P/V ratio can be estimated. This can be used for monitoring the actual gain of the photomultiplier. The P/V ratio is often given in data sheets.

- Single-electron resolution. If the first dynode has a high secondary emission coefficient (above 12), the P/V ratio may exceed 2 and it is possible to estimate the single photoelectron resolution. This is defined as FWHM of the single-electron peak divided by the position of the peak on the multichannel analyzer (expressed as a percentage). Events producing 2 simultaneous photoelectrons will give a second peak with twice the pulse height [24].

We performed single photoelectron spectrum measurements on three candidate PMTs for the HF Calorimeter; Hamamatsu 7525HA, Electron Tubes D844WSB, and Photonis XP3182/D1. After extensive timing, dark current, gain, and linearity tests, it was quite important for the candidate PMTs to give reasonable resolution for single photoelectrons at the gain level of 10^4. None of the manufacturers listed SPER of their PMTs in the spec sheets.

To determine the SPER (Single Photoelectron Resolution) of the candidate tubes we built two main setups with four different versions while improving our results at each time. In all the setups, we used 337nm LSI Nitrogen Laser (model VSL-337ND) as a light source and the beam intensity is reduced to the level of one photon by using neutral density filters. LeCroy 7kV high voltage power system (Model HV4032A) provides HV for PMTs.

2.3.4.1 First Generation SPER Setup

In the first version of the setup, the SPES (Single Photoelectron Spectrum) has been obtained by triggering the laser externally: Two Gate and Delay Generator units are used to setup a pulser to trigger the laser. This pulser signal has been delayed and used as the external gate for LeCroy qVt multichannel analyzer (Model3001). Total delay was about 560ns, the LRS Octal discriminator (Model 623) was used to create a 40ns gate signal. The PMT signal has been amplified by LeCroy Model 612AM six-channel variable amplifier and then integrated by qVt (see Figure 2.8). The qVt is set to charge (q) mode.

The resulting spectrum was displayed on Tektronix 2245A 100 MHz analog oscilloscope and we took the photograph of the screen with a digital camera. However, due to fluctuations in producing the laser pulse when externally triggered, there was a jitter in the anode signal coming from the PMT with respect to pulser signal. Despite the large jitter in the anode signal, we had a promising result for the Hamamatsu 7525HA PMT with P/V ratio of 2 at 1500 V (10^6 gain) (see Fig.2.9).

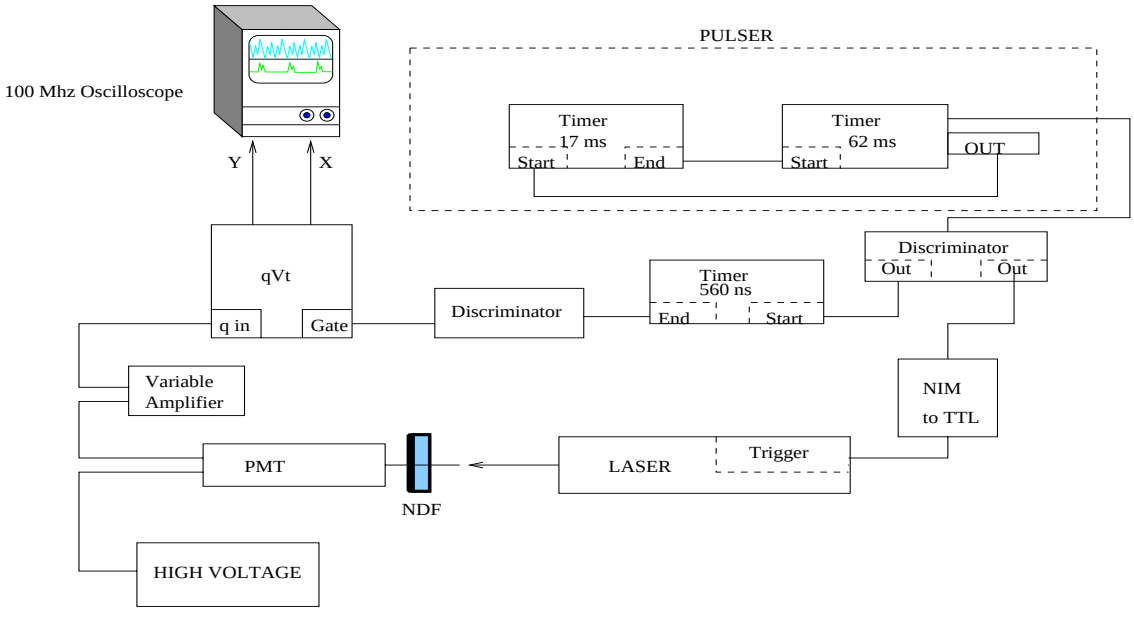

Figure 2.8: Block diagram of first generation SPER setup.

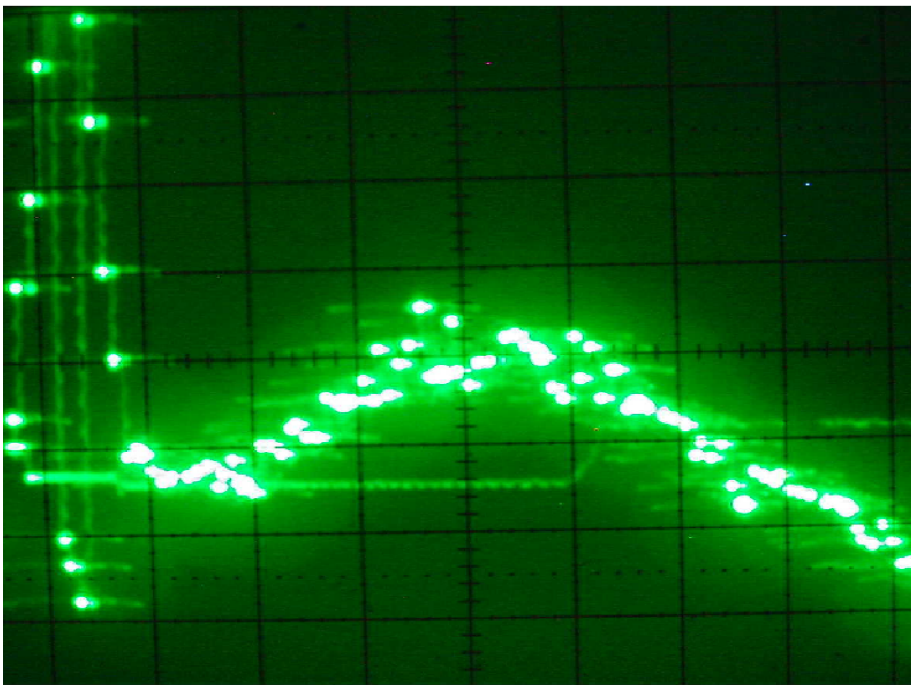

Figure 2.9: Scope view for SPES of Hamamatsu PMT with first generation SPER setup.

2.3.4.2 Second Generation SPER Setup

In the second version of the setup, we focused on decreasing the jitter in the signal. In this setup the laser was triggered internally (see Figure 2.10). Laser light was split into two beams, one beam went directly to the PMT through some neutral density filters and the other was directed to a PIN diode. We used PIN diode signal to produce a gate signal for the qVt. The width of the gate was 25 ns. These measurements resulted in less noise than the first version. The results were displayed on a 1 GHz Textronix digital oscilloscope. The picture on the screen was recorded as a JPEG file.

The Hamamatsu 7525HA tube gave almost the same result with the first setup at 1500 V (10^6 gain); estimated P/V ratio was about 2.2 and the resolution (FWHM/Peak Position) was about 60% (see Figure 2.11). SPES for the Electron Tubes D844WSB phototube gave an estimated P/V ratio of 1.4 and a resolution

of about 50% (see Figure 2.12). High voltage for D844WSB was set to 1200V (10^6 gain). Although the gain levels were the same, the count rate in case of D844WSB was much slower than 7525HA. This is probably due to the lower cathode efficiency. While Electron Tubes D844WSB and Hamamatsu 7525HA have comparable SPERs, measurements for Photonis under the same conditions (10^6 gain) were not successful (see Figure 2.13). It appears that the current gain for this tube was smaller than the others and the output was much more prone to noise. It was impossible to lower the light intensity to a level that will yield a single photoelectron and obtain an observable anode signal above the noise level at the same time.

We have observed that taping the metal parts, i.e., grounds, of both the signal and the HV connections coming from the tube to the optic table in contact with each other helps reduce the noise in the anode signal. In fact, it might be a good idea to ground the casing of these connectors properly by passing them through a small metal patch panel mounted on the side of the optic table.

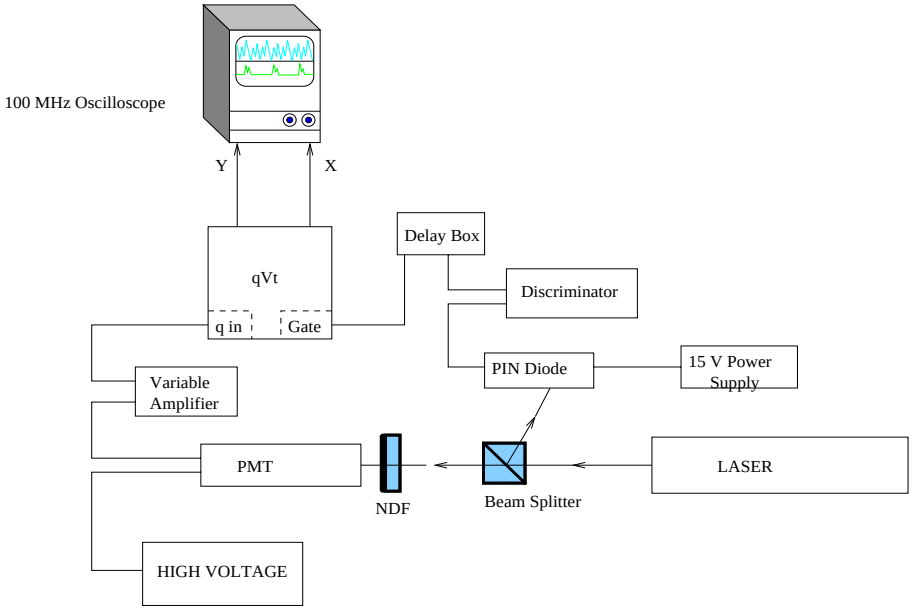

Figure 2.10: Block diagram of second generation SPER setup.

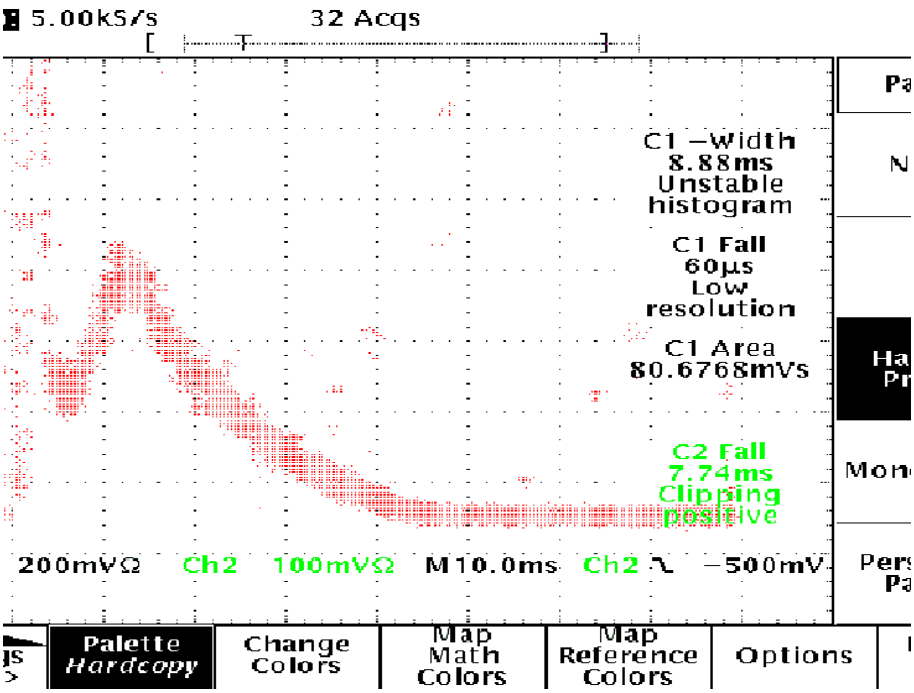

Figure 2.11: Scope view for SPES of Hamamatsu pmt with the second generation SPER setup.

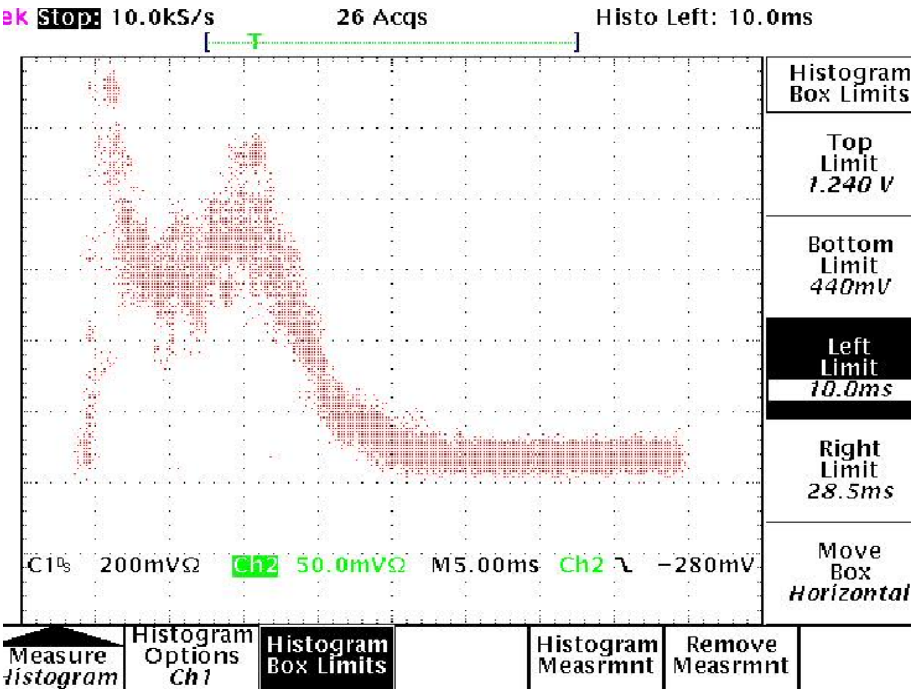

Figure 2.12: Scope view for SPES of Electron Tubes pmt with the second generation SPER setup.

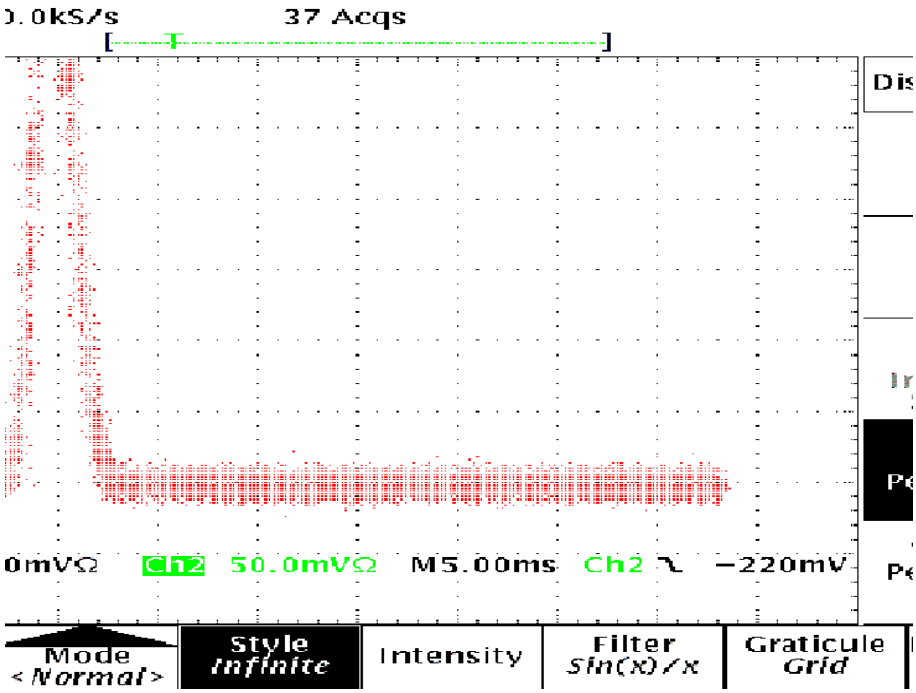

Figure 2.13: Scope view for SPES of Photonis pmt with the second generation SPER setup.

2.3.4.3 Third Generation SPER Setup

The third generation SPER measurements were performed by using LeCroy 2249A 12-channel ADC. The signal coming from the PMT was amplified by the variable amplifier and then transferred to the ADC. ADC was read out by LabView program. The gate signal for the ADC was provided by the same PIN diode arrangement as in the previous setup (see Figure 2.14) .

The third generation setup was constructed to obtain single photoelectron spectrum of the Photonis XP3182/D1 PMT. Consequently, with this setup we tested this tube and the Hamamatsu 7525HA only, the latter was for comparison of the setup with the previous versions. LabView gave us the opportunity to store and analyze the data more conveniently (see Figure 2.16).

The result for the Hamamatsu 7525HA was comparable with the previous measurements; a P/V ratio of 2.8 and a resolution of 60% at 10^6 gain (see Figure

2.15). The Photonis XP3182/D1 did not produce a reasonable single photoelectron spectrum.

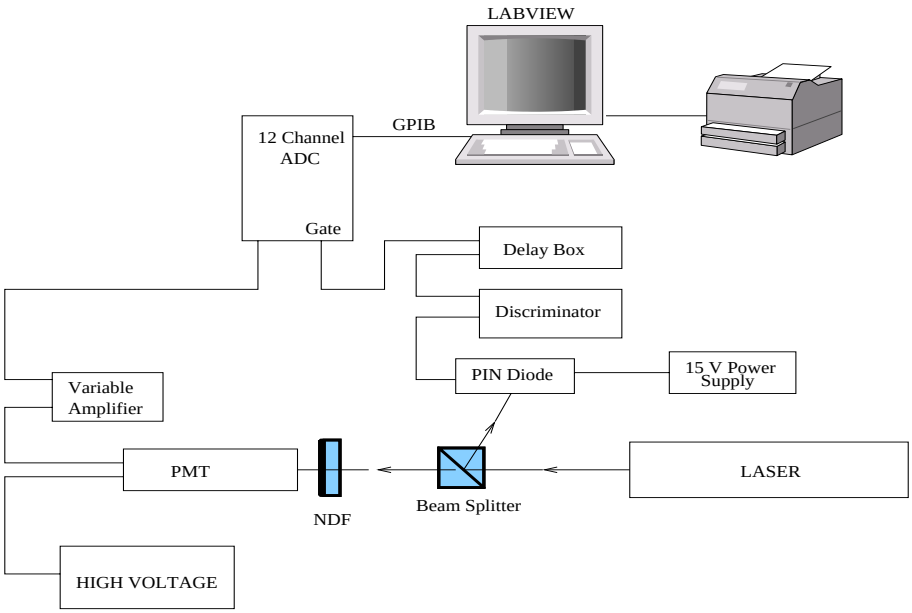

Figure 2.14: Block diagram of third generation SPER setup.

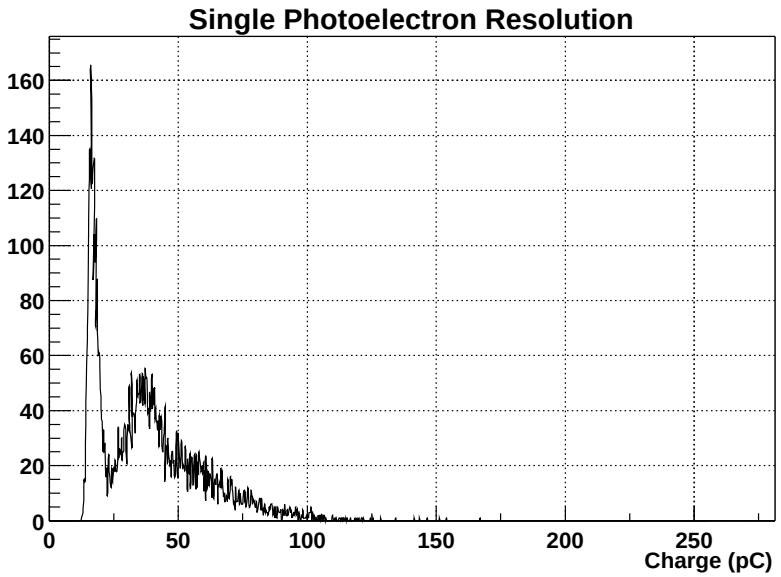

Figure 2.15: Hamamatsu SPES at 1500V from third generation SPER setup.

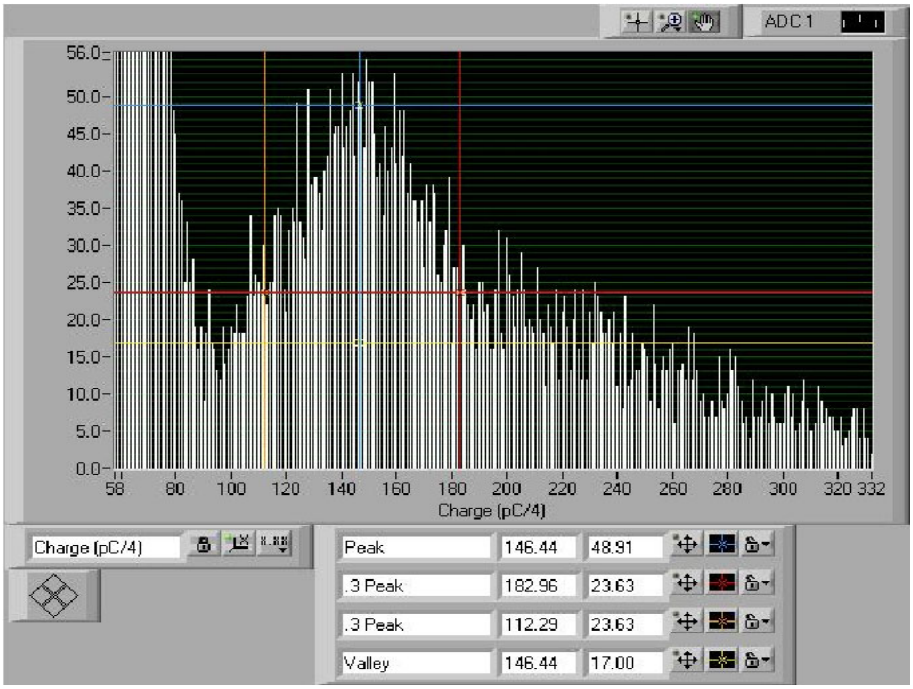

Figure 2.16: LABVIEW output of Hamamatsu SPES signal at 1500V from third generation SPER setup.

2.3.4.4 Fourth Generation SPER Setup

Obtaining the single photoelectron spectrum of the photomultiplier tubes is very difficult at low gains, because the signal coming from the tube is comparable to the noise level in the rest of the system. In the fourth generation setup (see Figure 2.17), we improved the previous setup by replacing the variable amplifier with a preamplifier. The preamplifier (see Figure 2.18) is manufactured in University of Iowa CMS laboratory and it has a gain of 5000.

With the preamplifier placed right at the base of the tube, we were able to see the single electron resolution for Hamamatsu 7525HA tube at 1100V (10^4 gain). This low gain measurement gave a P/V ratio of 2 and FWHM of approximately 54% (see Figures 2.19 and 2.20).

Improved setup also could not produce a reasonable spectrum for Photonis XP3182/D1 tube at 1500V (10^4 gain) (see Figure 2.21).

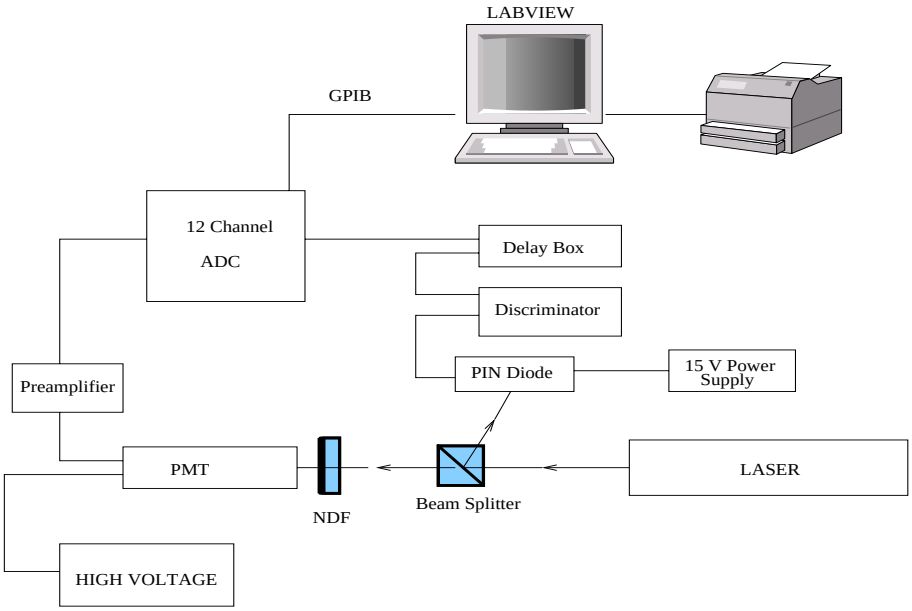

Figure 2.17: Block diagram of fourth generation SPER setup.

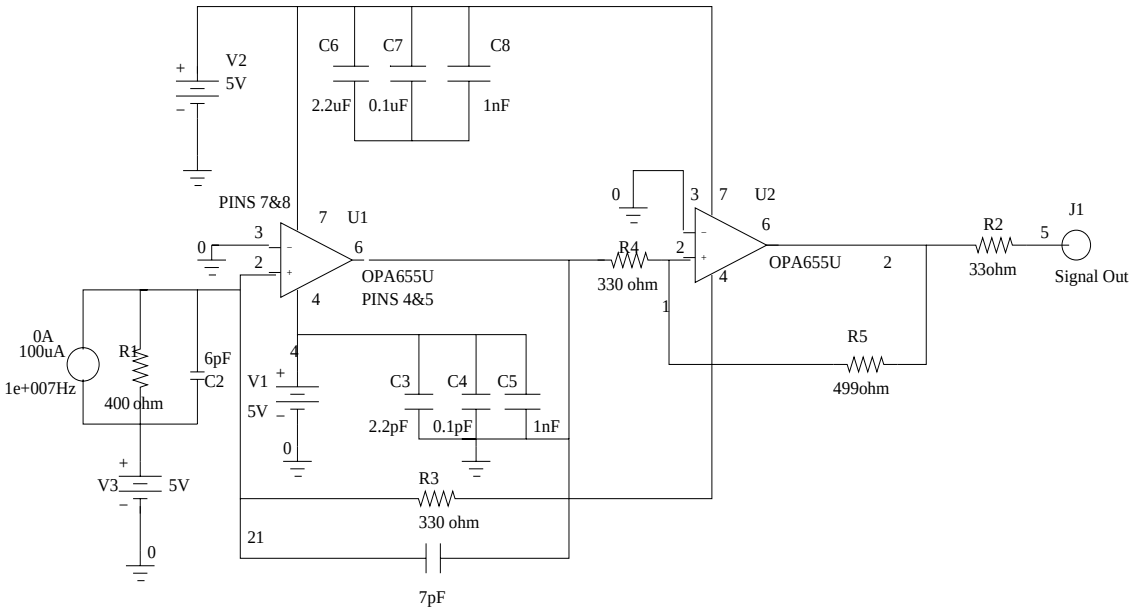

Figure 2.18: Block diagram of homemade preamplifier used in fourth generation.

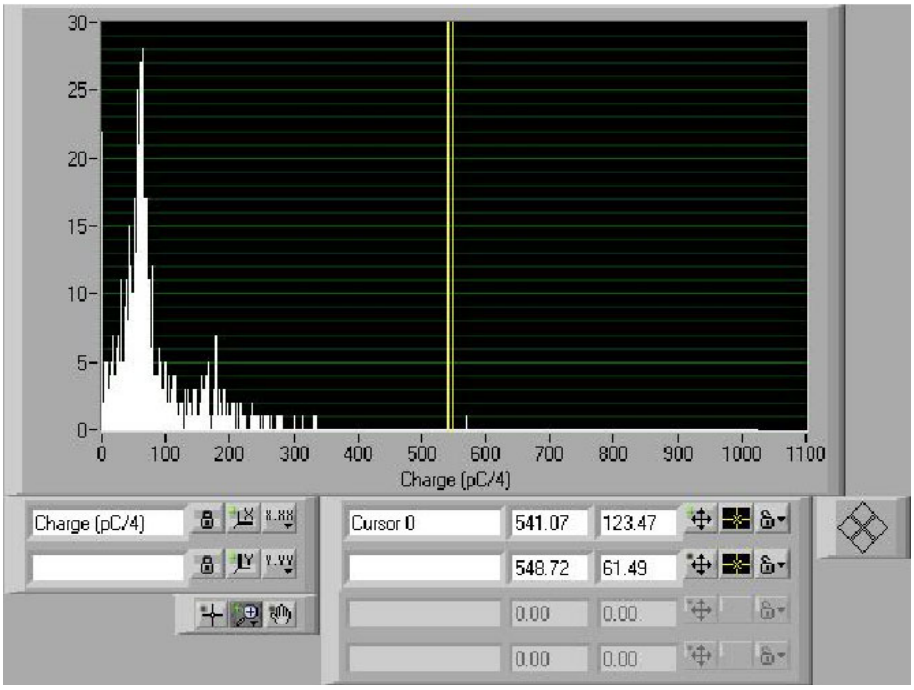

Figure 2.19: LABVIEW output of Hamamatsu SPES at 1100V from fourth generation SPER setup.

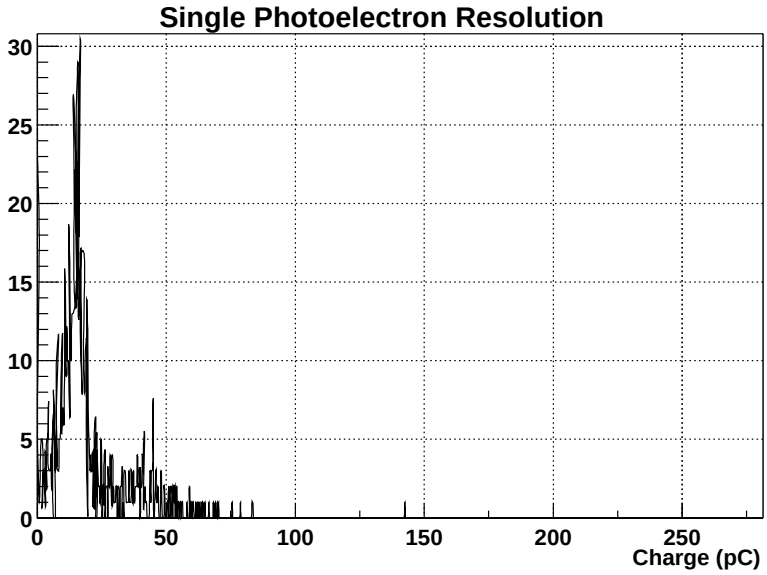

Figure 2.20: Hamamatsu SPES signal at 1100V from fourth generation SPER setup.

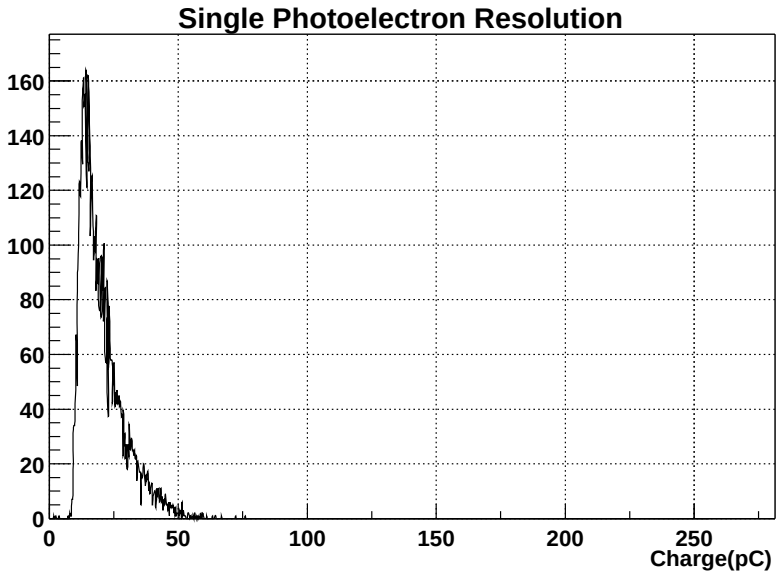

Figure 2.21: Photonis SPER signal at 1500V from fourth generation SPER setup.

2.3.5 Linearity Studies

Calorimeters extract energy information mostly through processing the pulses coming from the phototubes. Efficient and reliable operation of a calorimeter depends on phototubes that are linear over a wide range of light intensities.

Light produced in the fibers embedded in HF calorimeter is expected to vary in intensity. It is important to choose PMTs that are linear in producing pulses from light bursts shining on them. Another concern is the microstructure of the LHC beam. Collisions are to happen in bunch separated by 25 ns. Hence, the PMTs used in HF should continue to be linear under these circumstances.

Response of the candidate tubes has been tested with light pulses over a wide range of light intensities. Light pulses were well separated from each other. To further test the PMTs, double pulses simulating the proposed microstructure of the LHC collisions are used. Each double pulse is composed of two pulses separated by 25 ns and the amplitude of the second pulse is at approximately one fourth of the first pulse. Again each double pulse is well separated from each other (10 kHz).

Details and the results of these measurements are given below.

A phototube generates a signal proportional to the amount of light shining on the photocathode. In principle, this relationship is expected to be the same over a wide range of light intensities. However, due to space charge effects and drops in the high voltage due to light shining on the tube, the linearity may be adversely affected for that specific setup. At high intensities and rates, electrons left over from previous pulses will lower the effective potential difference between the anode and the dynodes and hence the electric field. Since the gain depends on the actual high voltage applied to the tube, a drop in the effective potential difference will mean a lower gain and a lower proportionality coefficient. Again, at high rates and intensities, HV power supply may not be able to maintain the same HV. Actual HV applied may start to drop due to high currents passing through the tube. This will also reduce the gain and cause a deviation from the regular response of the tube at low intensities.

Linearity measurement for a phototube is done to determine the point at which the tube starts to deviate from its regular response in a specific setup. Tube is linear if the output of the tube, in terms of total charge or current, is linearly proportional to the amount of light shining on it and the proportionality coefficient stays the same for different light intensities. Linearity can be measured in different ways. DC linearity is done with a continuous light source and mainly shows the dynamic range of the tube. Pulse linearity also shows the recovery characteristics of the tube.

2.3.5.1 Single Pulse Linearity Test

Pulse linearity of a tube can be measured by shining light pulses with varying intensities and measuring the output. Varying the light intensity can be achieved easily reproducibly by inserting neutral density filters in between the light source

and the tube. Plotting the total charge versus the neutral density filter factor would show us the behavior of the tube. In order to investigate the linearity of a tube over a large range of light intensities, we should plot the logarithm of the output peak voltage or the total charge, versus the light intensity. Since the neutral density filter factor is the power of ten for the attenuation factor, using the NDF factor instead of the light intensity is equivalent to taking its logarithm. It should be kept in mind that the higher NDF factor would correspond to lower light intensity. Hence, any deviations from linearity will show up as deviations from a straight line at lower NDF factors. Pulse linearity measurement done on a Hamamatsu tube is shown on Figure 2.22. In this measurement a pulsed nitrogen laser (337 nm) was used as the light source.

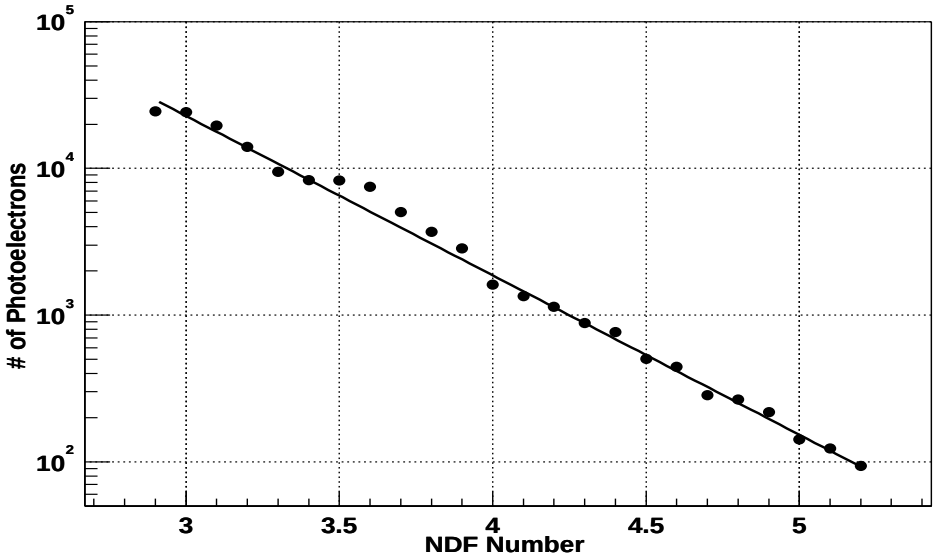

Figure 2.22: Single Pulse linearity measurement of a Hamamatsu PMT (serial number ZC9898).

2.3.5.2 Double Pulse Linearity Test

Another type of pulse linearity measurement is double pulse linearity. The double pulse linearity tests carried out here are different from the manufacturer suggested tests. Standard double pulse tests are done with two pulses where each pulse is well separated from the other. The amplitude of the second pulse is about one fourth of the first pulse. The second pulse is used as the reference. Our modification to this standard test was to bring the two pulses closer so that the two pulses are separated by 25 ns. Amplitude ratios are not changed. This way we could also study the recovery characteristics of different tubes under LHC conditions. Figure 2.24 is the resulting anode signal when a LED driven by a waveform shown on Figure 2.23. Even though the driving waveform is very sharp, anode signal has a large tail due to both the fact that LED is not fast enough to go back to zero level and the timing characteristics of the tube tested. Space-charge effects limit the fast recovery of the tube long before the second pulse, hence the non-linearity of the tube. To reduce the LED contribution, a few volts of reverse bias is applied. It seems that the LED effects are negligible since the results show a large sensitivity to PMT types and we only need relative measurements.

Figure 2.25 shows that Hamamatsu PMT (SN:9957) is linear within a few percent up to 45 mA peak current at about 4×10^4 gain. Here, the deviation from linearity versus the peak current in the tube is plotted. Peak current is defined as the instantaneous current produced by the first (large) pulse in a 50 Ω resistor. Deviation from linearity is defined as the percentage difference between the peak height ratio at a given peak current value and a reference ratio. Reference ratio is the peak height ratio at a very low peak current. Peak height ratio is calculated as the ratio of the peak amplitude of the larger pulse to the smaller pulse. Since the range of peak currents that we can safely get from the tube is not that wide, a linear plot is sufficient.

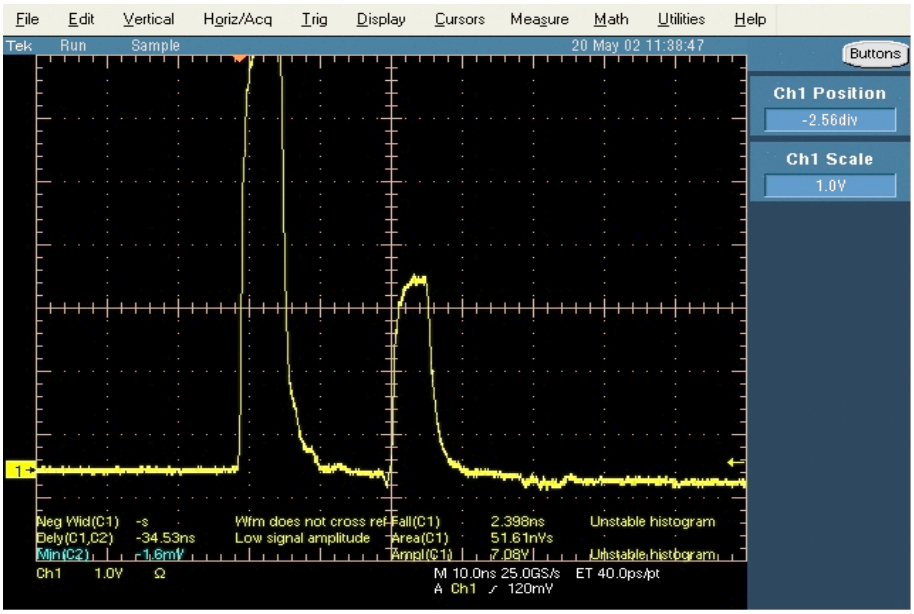

Figure 2.23: Waveform driving the LED for double pulse linearity measurements.

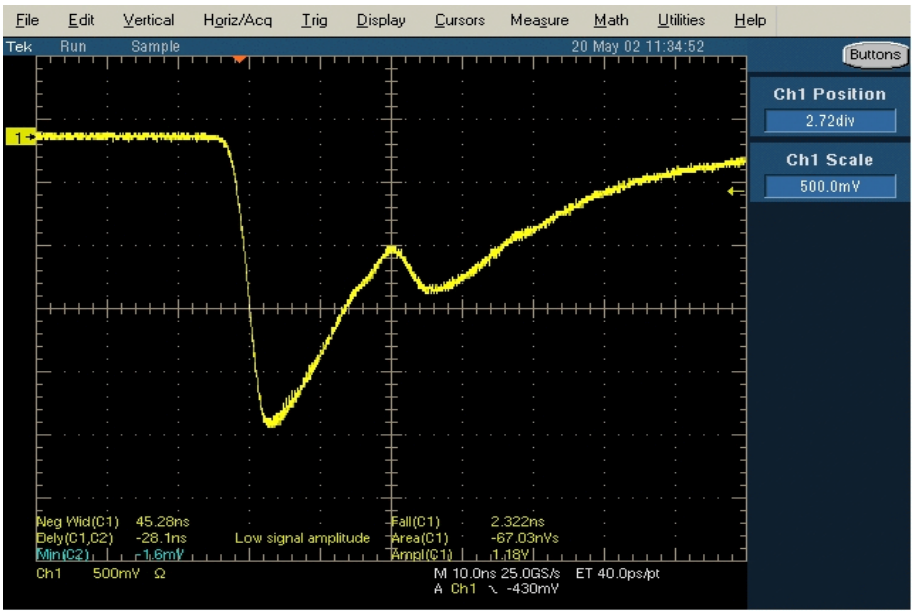

Figure 2.24: Anode signal of PMT when the LED is driven by the waveform shown on Figure 2.24. HV applied is 1100 V resulting is 5×10^4 gain with the resistive base.

Similar measurements are done with the Cockroft-Walton (CW) base developed at Fermilab (See Figure 2.26). Linearity in CW base case is good up to 20 mA within 5%.

The space charge effect is worse in case of the Photonis tube (type: 3182) as shown on Figure 2.27. For this tube, as the peak current increases, the peak height of the second pulse seen in the anode signal starts to decrease after a certain peak current value. This could be due to the space charge effects. The tube may not be recovering fast enough for the second pulse.

Figure 2.28 displays further results of double-pulse linearity tests, comparing Hamamatsu with both resistive and CW bases and EMI with CW base. Hamamatsu seems to be slightly better than EMI.

In all these double pulse linearity tests, different light intensities are obtained by varying the distance between the tube and the LED.

CMS-HF requires the tubes to be linear in a range of 1-3000 photoelectrons or up to a few mA peak currents. When we consider the above results, it looks like the Hamamatsu tubes have better linearity since they are linear up to a few tens of mA peak currents for the double pulse linearity and also linear in the 1-3000 photoelectron range.

EMI tubes meet CMS-HF requirements also, but they start to deviate at lower peak currents. They are somewhat marginal.

Photonis tubes, on the other hand, are not as linear as requirements ask since they do not seem to recover fast enough even after a not so large pulse. For this reason, double pulse linearity tests performed on these tubes do not have much meaning.

Using different type of bases, such as, resistive and Cockroft-Walton type, does not change the conclusions reached above. However, in case of CW bases, the tubes start deviating at an earlier peak current value.

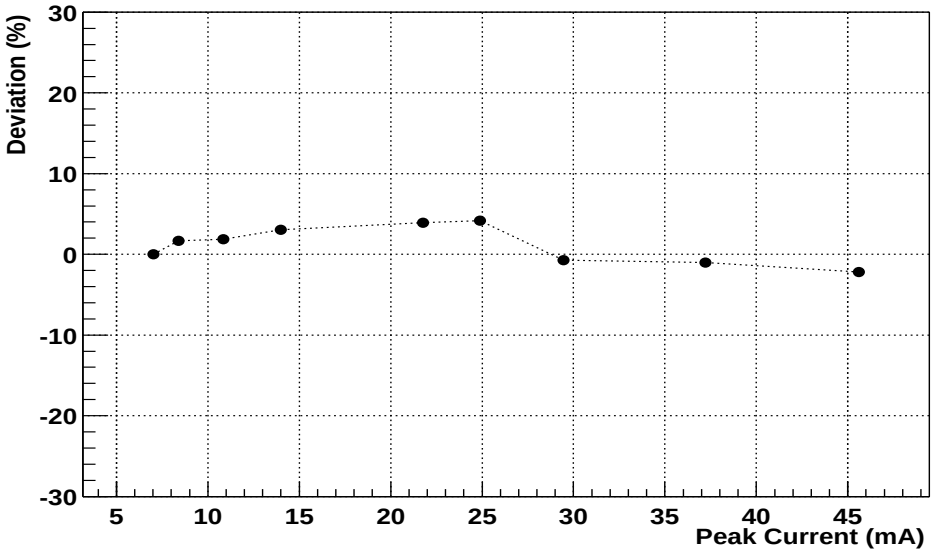

Figure 2.25: Double pulse linearity plot for a Hamamatsu Tube (S/N:9957) with resistive base.

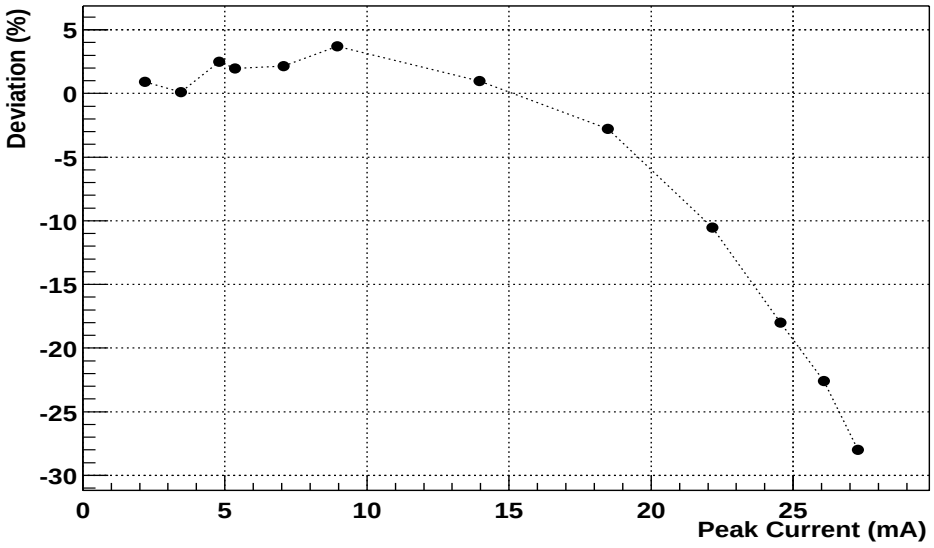

Figure 2.26: Double pulse linearity plot for a Hamamatsu Tube (S/N: 9957) with CW base.

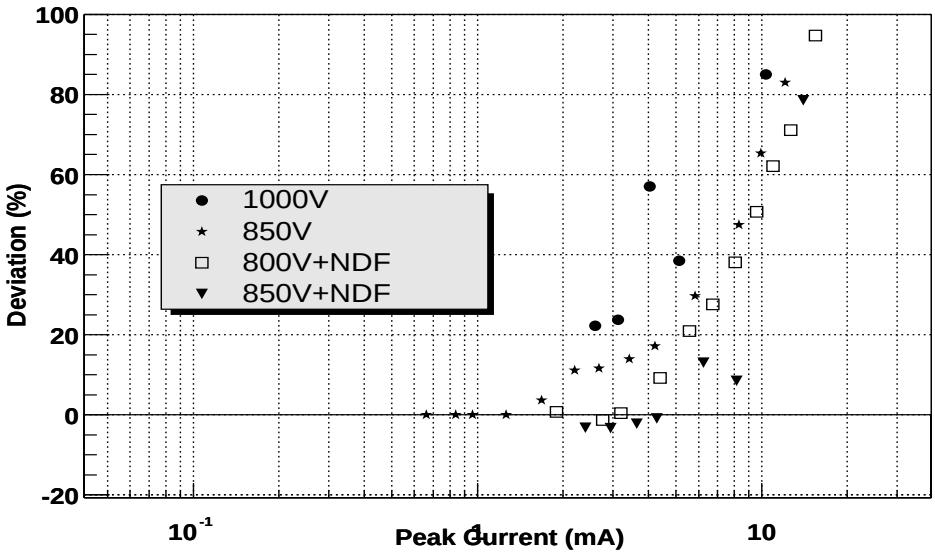

Figure 2.27: Double pulse linearity plot for a Photonis PMT.

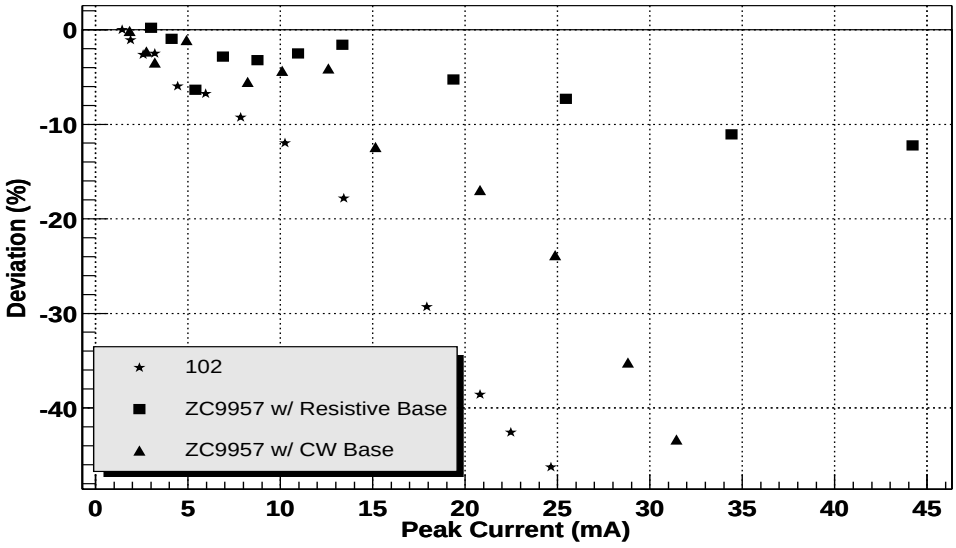

Figure 2.28: Double pulse linearity tests for Hamamatsu and Electron Tubes PMTs.

2.3.6 X-Y Variation of Photocathode

Uniformity of the photocathode surface is important since the individual fiber core diameters are 600 μm. Fibers attached to the same tube but coming from different sections of a tower might correspond to different charge amounts for the same light intensity if there is spatial nonuniformity. This might introduce systematic effects that would be difficult to correct for.

A setup is designed to scan the photocathode surface both vertically and horizontally. In this setup, light coming from a tungsten bulb shines on a mask. The mask is a completely opaque screen made of black kapton with a small (3 mm diameter) pinhole drilled into it. This mask is stationary and the PMT behind it can be moved in both vertical and horizontal directions. The PMTs are positioned so that the first dynode is horizontally oriented.

The anode current can be measured as a function of position when the PMT was being moved by the computer with the help of a stepper motor. Scan results show that the tubes meet the HF requirement for x-y uniformity. However, it turns out that the uniformity is not really that important since the fibers will not be directly attached to the tubes. There will be a 42 cm long (nominal) light guide between the fibers and the tube which mixes and disperses the light to the PMT cathode. Scans with a light guide show that any nonuniformity that might exist on the photocathode surface disappear because of the diffusion of the light beam when it reaches the photocathode surface (see [23] for details).

CHAPTER 3
COMPLETE TESTS OF THE HF CALORIMETER PMTS

3.1 Introduction

Each of the HF calorimeters consists of 18 wedges (see Fig 3.1) and there will be 48 PMTs per wedge. The PMTs will be located in the read-out boxes (see Fig 3.2) with light-guides, magnetic shields, and high voltage boards. They will be powered by HV boards (see Fig 3.3) in groups of eight.

The characteristics and the quality of the phototubes are closely related to the successful operation of the HF Calorimeter. Table 2.1 summarizes all the requirements relevant to the mechanical design and the operation of the HF calorimeter. Furthermore, the electronics system to be used to process the PMT signals requires very low amplitude signals. Therefore the PMTs should be operated at a low gain but still satisfy all the timing, gain, efficiency, and resolution requirements.

Manufacturers were asked to make suggestions for specific PMTs conforming to HF requirements. Hamamatsu, Electron Tubes, and Photonis responded. They provided some phototubes whose specifications seemed to agree with the HF requirements. These suggested PMTs were tested under varying conditions to determine the dynamic range of their operating parameters (see Chap.2 and [27]).

Hamamatsu R7525HA PMT was chosen after these measurements, since its overall performance was better than all the others. The 2300 Hamamatsu R7525HA PMTs were delivered by the manufacturer in 2002-2003 in batches of 20 to 300. The quality control and check on these PMTs were performed at the University of Iowa PMT Test Station. In this chapter we are giving the details of the PMT Test Station and the testing procedure.

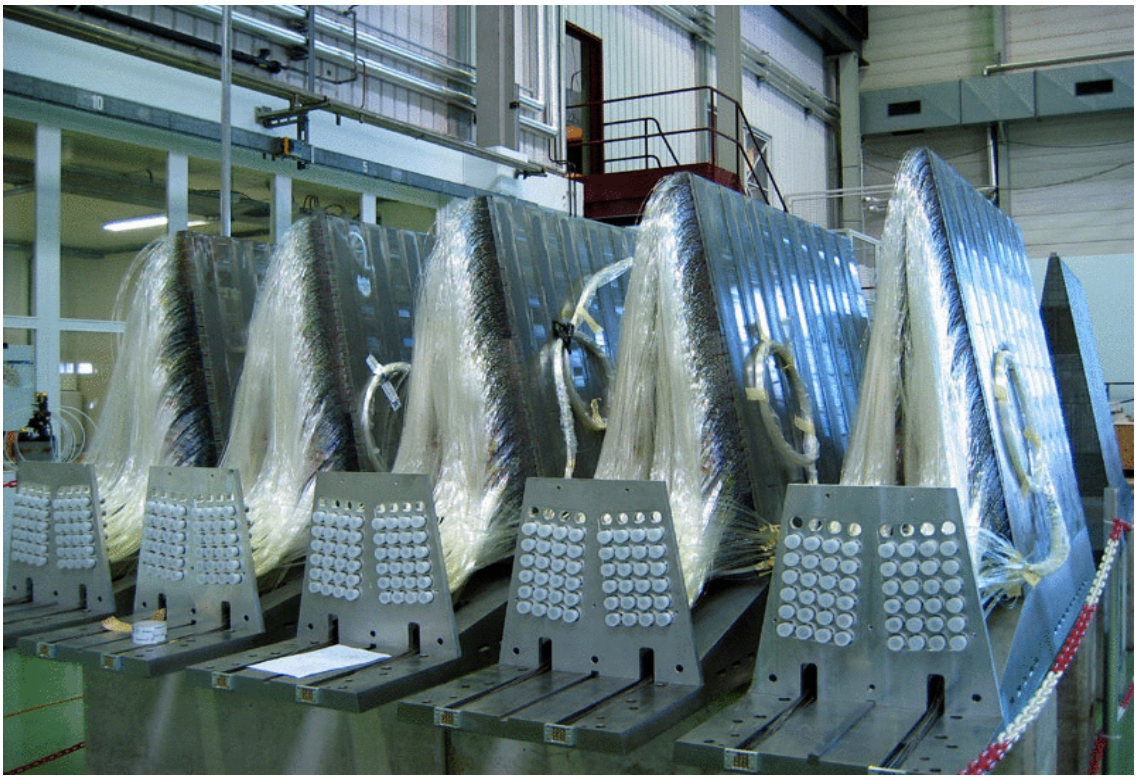

Figure 3.1: CMS HF calorimeter production wedges.

3.2 The University of Iowa PMT Test Station

The University of Iowa PMT Test Station was designed initially for PMT comparison measurements for the CMS-HF Calorimeter. It evolved during those measurements and finalized by the time the PMTs started arriving from the manufacturer.

To expedite the overall testing, all the tests are streamlined and computerized as much as possible. Also we prepared dark boxes and developed a LabView program for data acquisition.

There are three dark boxes (see Fig.3.5). They are made of plywood and inside surfaces are covered with light absorbing black cloth. An optical table forms the bottom side of first two dark boxes. First box houses the timing and single pulse linearity setup. It is also used for double pulse linearity and single photoelectron resolution measurements with minor modifications. Relative gain and dark current

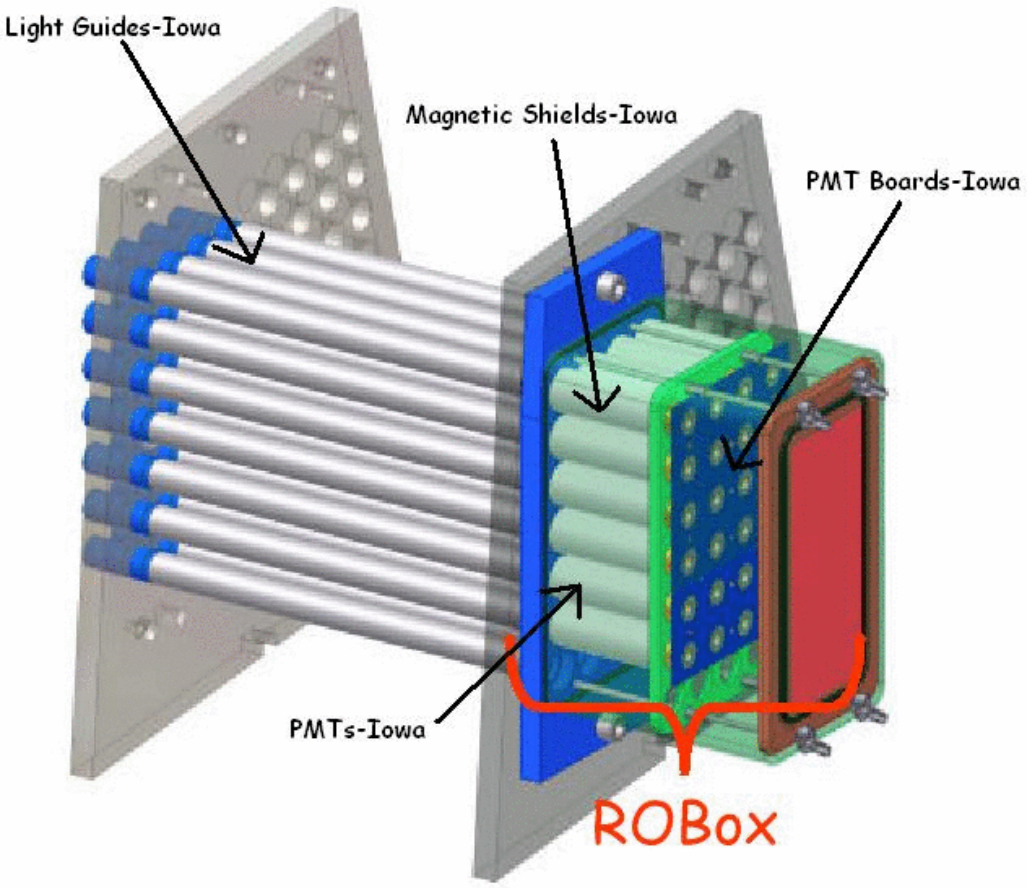

Figure 3.2: CMS HF calorimeter Read-Out Box (ROBOX) design.

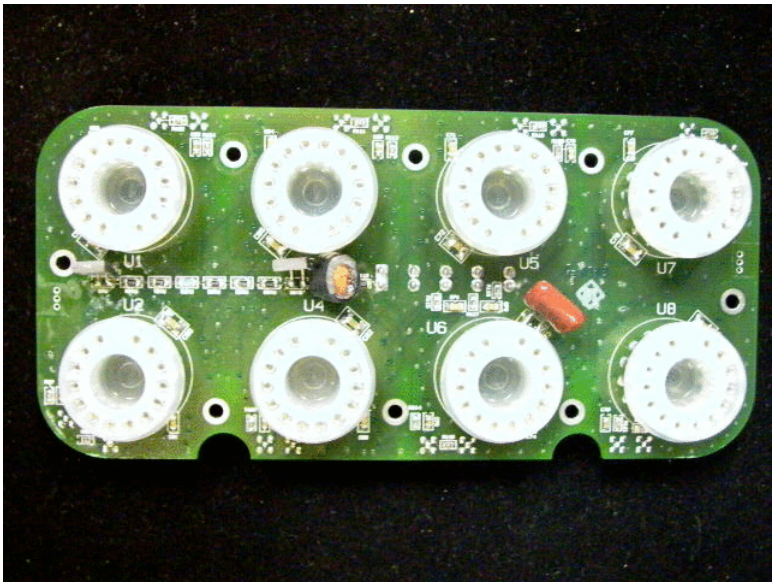

Figure 3.3: CMS HF calorimeter PMT HV base board.

Figure 3.4: Hamamatsu R7525 PMT.

measurements are done in the second dark box. Full gain versus HV measurements are also done in the second box with some modifications. Third dark box is independent of these two and used only for the lifetime test. Each dark box has a patch panel on the side for signal and HV cables.

A Tektronix Oscilloscope (TDS5104 digital oscilloscope with 1GHz Bandwidth and 5 Gs/s sampling rate) and a PC combination are used for timing and pulse linearity measurements. A Visual Basic Program controls the data acquisition. Gain and dark current measurements are done using an ADC and a picoammeter controlled by a LabView program. Further details of the test station, specific to each type of measurement, will be given in the relevant section below. Our rejection limits, based on the HF requirements are listed in Table 3.6.

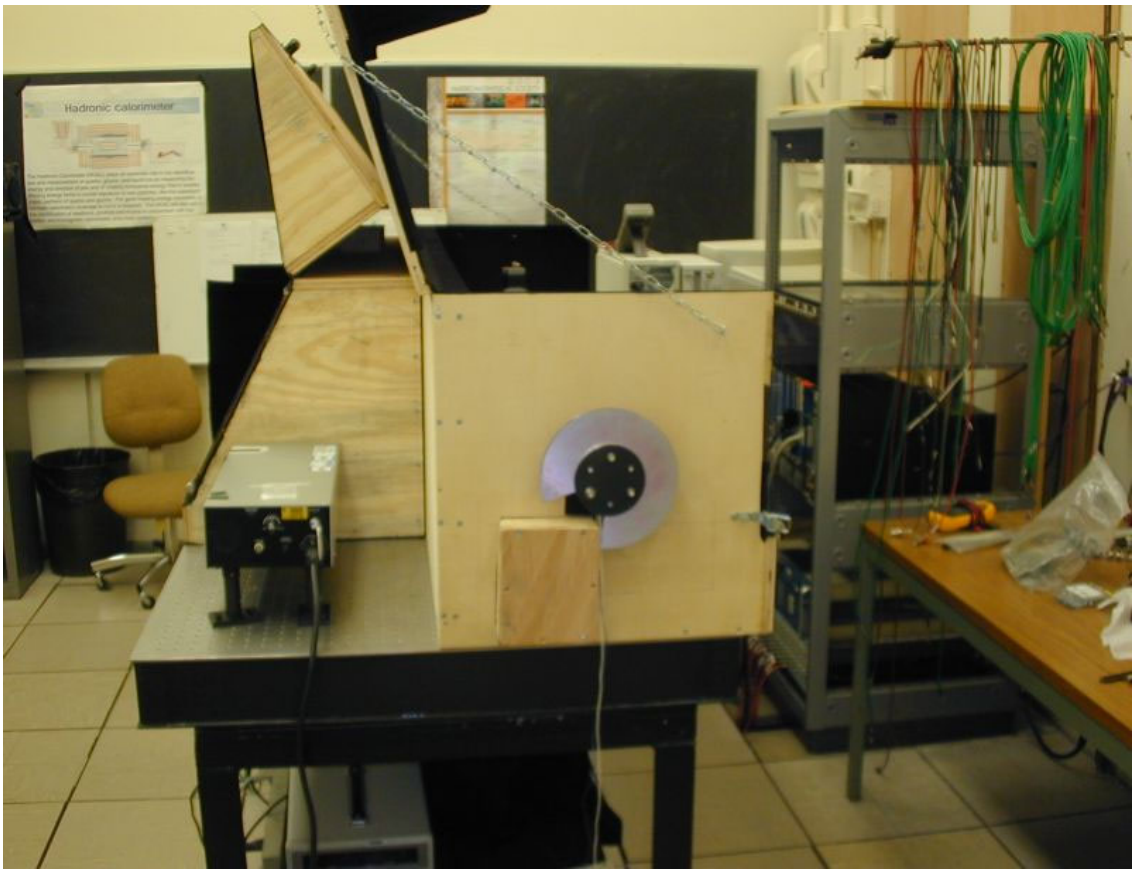

Figure 3.5: The University of Iowa PMT Test Station.

3.3 PMT Tests and Results

There were two types of tests; complete and sampling. Complete tests were done on all the tubes. These included the measurements on the timing response: transit time, transit time spread, pulse width, and rise time. There were also measurements for single pulse linearity (deviation from linearity), dark current, and relative gain. Second group of tests were done only on a small sample of PMTs selected randomly. Single photoelectron resolution, double pulse linearity, spatial uniformity of the photocathode surface, and gain vs HV measurements were done on this small sample of PMTs. We decided not to perform these measurements on all the tubes because of time limitations. We had to finish these tests in a short time so that the tubes would be ready to install in the calorimeter. The lifetime test was done only on a few PMTs since this test was a terminal one.

In addition to these tests, each tube was logged in upon arrival and inspected visually prior to the general tests mentioned above. Any cracks, scratches, etc. were noted. Envelope was checked for HV conductive coating and opaqueness. After this the tubes were ready for testing. Algorithm of the testing procedure was summarized in Fig.3.6.

3.3.1 Timing Characteristics

Well defined time response of the PMTs is crucial for the smooth operation of the calorimeter. PMTs should be able to generate corresponding signals for each event in time and recover before the next collision event occurs. Since the successive collisions will occur in 25 ns intervals, combined width and transit time should be less than this. Hamamatsu R7525HA provides this kind of time response. Typical transit times of about 15 ns and widths below 5 ns reduce the pile-up effects due to successive hits in the same fiber bundle.

Setup used in timing measurements was developed during the comparison

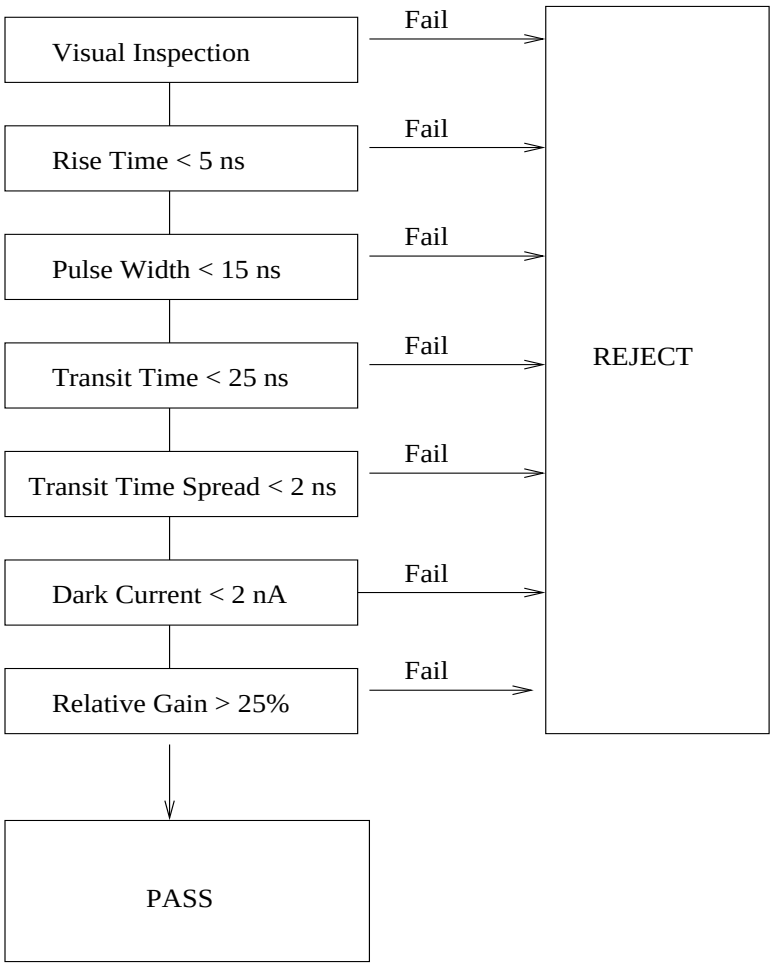

Figure 3.6: Testing algorithm.

process and finalized for the tests (see Fig. 2.1). In this setup, a 337 nm Nitrogen pulsed laser is used as the light source. The laser light passes through a neutral density filter (NDF) and falls on a 50/50 beam splitter. The reflected light goes to a PIN diode to provide the trigger and reference signal (see Fig.3.7). The transmitted light passes through more NDFs before hitting the PMT. These NDFs are used for providing appropriate attenuation levels. This is especially important for single pulse linearity measurements. NDFs are placed on a wheel that is controlled by the data acquisition program. Identical cables bring the PIN diode signal and the PMT anode signal to the oscilloscope. Since the transmitted light travels 70 cm further than the reflected light, 2.3 ns additional time delay in the transmitted light is taken into account in the analyzing program.

Figure 3.7: Timing setup, pin diode, beam splitter configuration.

The HV is provided by a LeCroy HV power supply (see Fig.3.20). A standard Hamamatsu resistive base is used for the PMTs (Fig.2.6). Since the electronics that will process the PMT signals require small signals, tubes will be running at low gains like $10^4 - 10^5$. For these tubes 1100 V seems to give an average gain of about

5×10^4.

Additional partitions are placed inside the dark box separating each part to prevent reflections. All the surfaces are covered with black, light absorbing cloth. On the partitions there are small holes for the light to pass through.

PIN diode signal provides both the reference signal for the timing measurements and also the trigger signal for the digital oscilloscope. The transit time is measured as the time difference between the PIN diode and the PMT signals when both signals reach 50% of their peak values successively. Rise time is defined as the time interval when the signal goes from 10% of the peak value to 90%. (What we mention here as rise time is actually the fall time since the signal is negative.) Width is simply the FWHM of the PMT signal. All these measurements are done automatically by the oscilloscope. For the transit time, pulse width, and rise time measurements, oscilloscope takes data in the single sample mode. It acquires 100 signals and then the program calculates the averages. On the other hand, the transit time spread is simply the standard deviation of the 100 transit time values.

We have performed these measurements on one tube about 50 times to get an idea of our statistical uncertainty. Uncertainties we have determined this way are; less than 0.4% for transit time, 9% for the pulse width, 8% for the rise time, and about 30 or 40% for the transit time spread.

Transit time values show a narrow distribution around 15 ns (see Fig.3.8). Given the 0.1 ns statistical uncertainty in our measurements, this narrow distribution shows that all the tubes have almost the same transit time. This is very good for the smooth and stable operation of the calorimeter.

Rise time (Fig.3.9) and pulse width (Fig.3.10) distributions, on the other hand, are somewhat wider. This is partly because of our larger statistical uncertainty. In fact, taking these larger uncertainties into account, we can also conclude that pulse width and rise time values for different tubes are also almost the same.

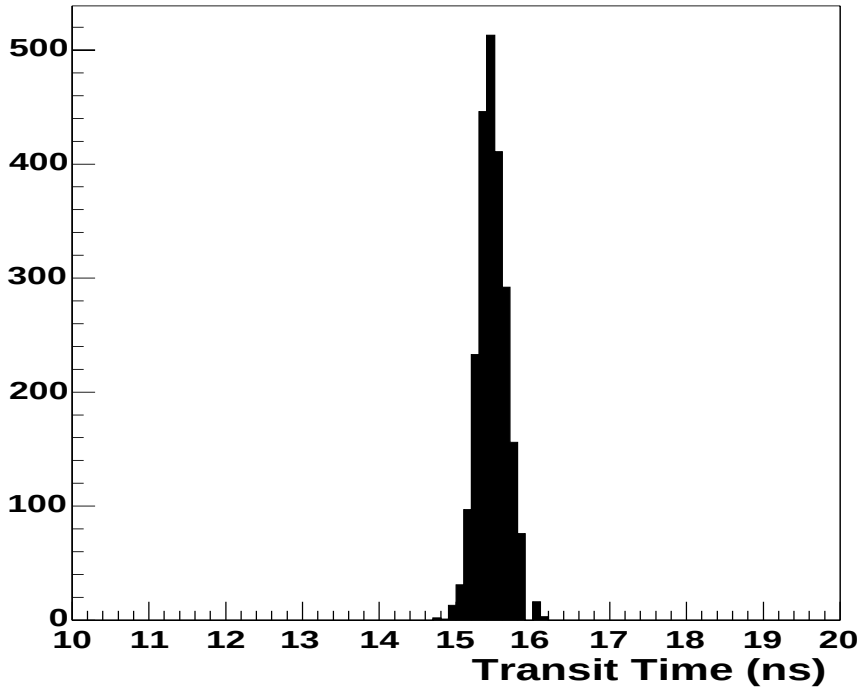

Figure 3.8: Transit time distribution for all the PMTs tested.

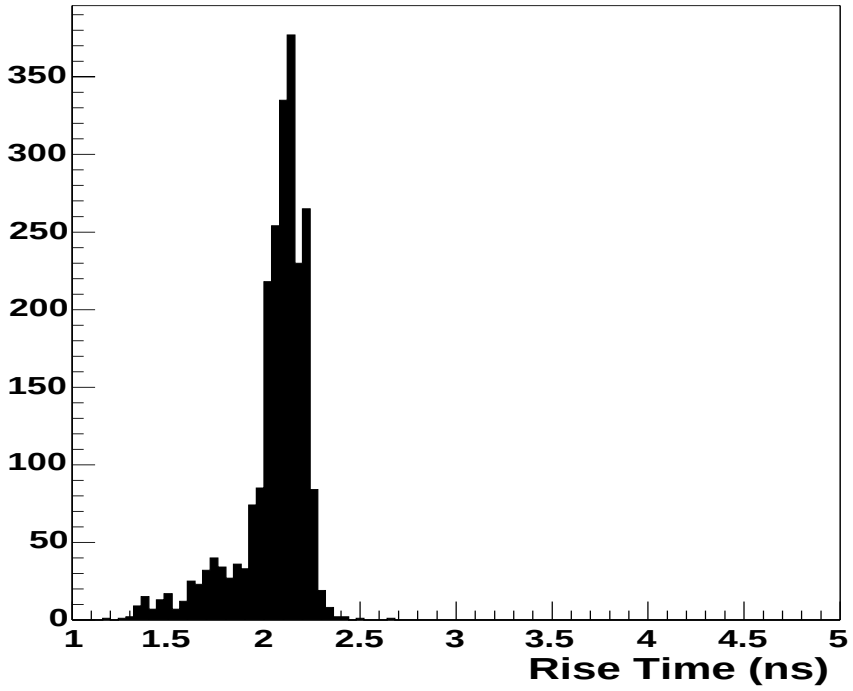

Figure 3.9: Rise time distribution for all the PMTs tested.

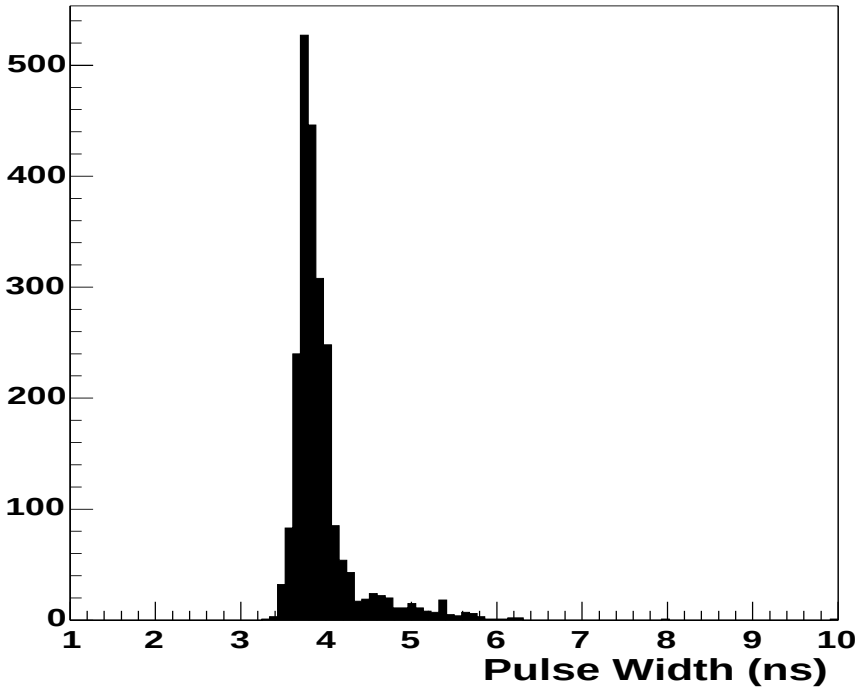

Figure 3.10: Pulse width distribution for all the PMTs tested.

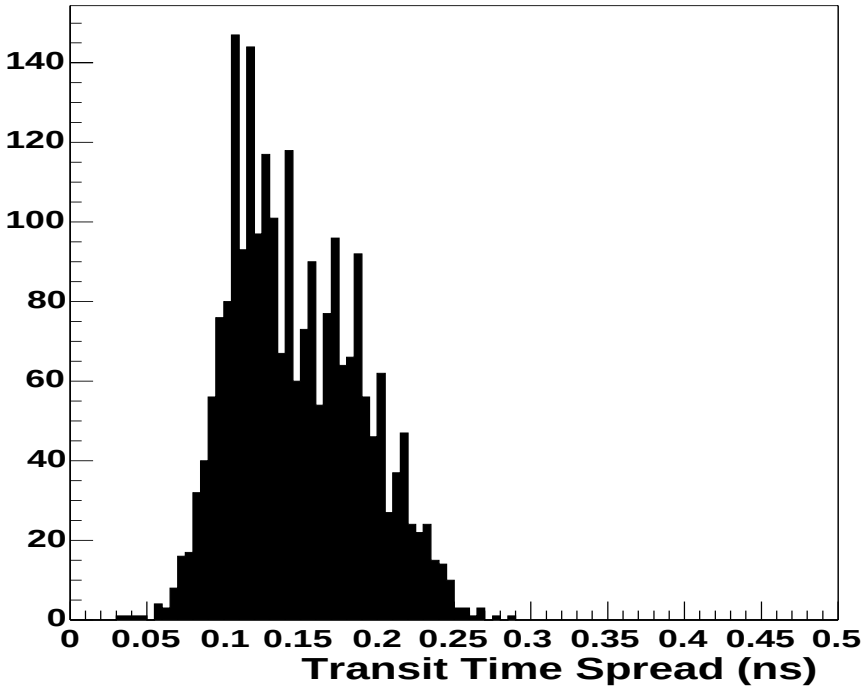

Figure 3.11: Transit time spread distribution for all the PMTs tested.

Transit time spread has a wider distribution (Fig.3.11), but again the overall distribution width we observe can be attributed mostly to the 30% statistical uncertainty.

3.3.2 Single Pulse Linearity

Since the intensity of the Cherenkov light pulses are expected to vary, the PMTs should be able to provide correct energy information over the range of light intensities that we expect from the quartz fibers. They should be linear over a range of 1 to 3000 photoelectrons as mentioned in the HF requirements (Table 2.1).

In principle, the number of photoelectrons emitted from the photocathode is proportional to the light intensity, which is related to the energy deposited. Then these photoelectrons are multiplied in the tube and the final number of electrons that reach the anode forms the anode signal. However, the efficiency in producing the photoelectrons depends on the photocathode characteristics, impact position of the initial light ray on the photocathode, etc. The multiplication factor and the final number of electrons also depend on the voltage applied on the tube or the actual effective voltage on the anode-dynode-cathode system and the impact points of the photoelectrons and subsequent secondary electrons on the dynode surfaces. Effective HV might be lower depending on the amount of light shining on the PMT or because there are residual charges left over from previous pulses. Usually, a combination of these effects contributes at higher intensities and causes the tube to deviate from a linear response. Deviations observed at lower intensities are usually due to statistical fluctuations.

There are two types of linearity measurements; DC and pulse. DC linearity measurements are done for DC applications where there is a continuous light beam shining on the tube, which is not the case in our calorimeter. Pulse linearity measurement is more relevant to our detector. Light pulses at varying intensities fall

on the tube and the energy response of the tube is measured as a function of the light intensity. When the effects mentioned above start to become significant, tube response will start to deviate from the linear response. In these measurements, intensity of the light pulses should be determined accurately. Otherwise, it will show false deviations from the linear response. This is usually achieved by sending alternate pulses at 25% of the total magnitude. Using the ratio of the outputs for the full and fractional signals cancels the intensity and amplification factors. These pulses should be well separated so that there should be no residual effect from the previous pulse. However, in our complete measurements we did not use the method explained above. We used the full magnitude pulses only in the single pulse linearity tests.

Single pulse linearity is defined as the average absolute percentage deviation from the linear response over a fixed range. The setup used in the timing measurements is also used for pulse linearity measurements. The intensity of the light shining on the photocathode is varied by changing the NDFs in front of the PMT. NDF factors can be set to a value between 1.0 and 3.0 at 0.1 steps. (For example, a NDF factor 2.0 means an attenuation factor of 10^2.) This means that the attenuation factor can be varied from 10 to 1000. The NDFs with different factors are mounted on a wheel which is controlled by the computer. Data acquisition program sets the filter wheel to a specific position and takes data. Number of photoelectrons emitted from the photocathode is calculated by dividing the total charge accumulated at the anode by the current gain. A constant current gain of 5×10^4 is assumed in the data acquisition program. The actual light intensities are monitored with the help of the PIN diode signal area and determined by using the actual measured attenuation factors. Then the number of photoelectrons versus the corrected light intensity data is fitted to a straight line. We call the average percentage deviation from the straight line for each tube, up to 3000 photoelectrons, as single pulse

linearity. Fig. 3.12 displays the single pulse linearity distribution for all the tubes.

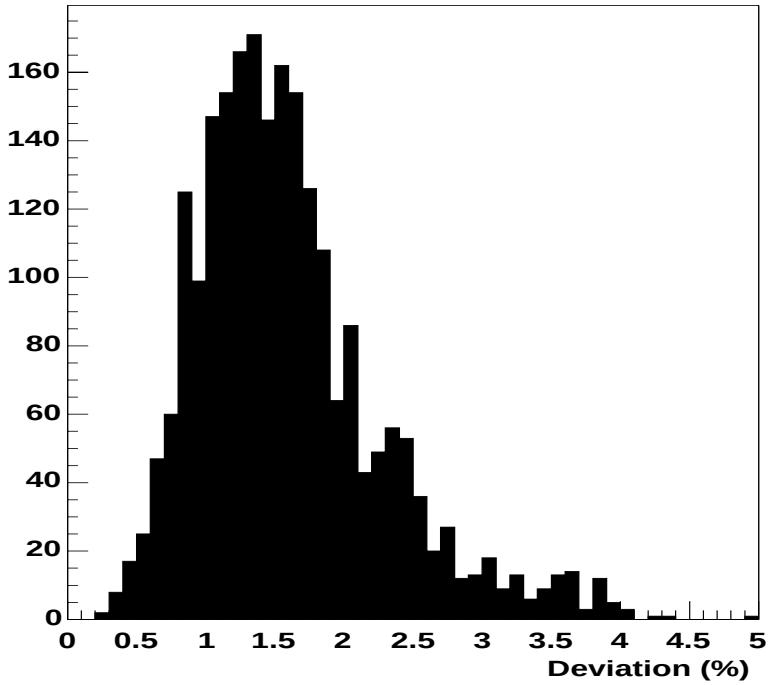

Figure 3.12: Distribution of single pulse linearity results for all the PMTs. x-axis is percentage deviation from linearity.

In the measurement mentioned above where we have measured various quantities for 50 times for the same tube, we have also determined the statistical uncertainty for the single pulse linearity to be about 6% of the measured percentage. Single pulse linearity histogram (Fig.3.12) of all the tubes shows a wider distribution than that can be attributed to statistical uncertainty. However, we also know that we have systematic effects that introduce additional fluctuations to the results, thereby increasing the width. This is mainly from the constant gain assumed in the number of photoelectron calculation. Correcting for this effect and repeating the fits with the corrected number of photoelectrons narrows the distribution. Without the gain correction, we would be including those data points with corresponding

intensities above 3000 photoelectrons. At higher NDF factors or at low light intensities, noise also introduces false deviations. These can be avoided by stopping at a maximum NDF factor. We also take our measurements at a single oscilloscope setting to reduce the systematic effects coming from the scope calibration between different scales. Overall, we seem to have about 1% systematic effect remaining in the system, so we should set our rejection limit to above 3%. However, even those tubes resulting in a higher linearity (nonlinear) value yield lower values when they are retested. There seems to be more systematic effects and higher statistical uncertainties in the system. For this reason, we decided not to include the single pulse linearity results in the rejection decision.

3.3.3 Dark Current and Relative Gain

The second dark box houses the dark current, relative gain, gain versus high voltage, and spatial uniformity measurement setups. In fact, a PMT-holder designed to hold eight phototubes is used in all these measurements. PMT-holder is a 10 cm diameter circular metallic piece (see Fig. 3.13). There are eight holes for the PMT bases, where standard Hamamatsu resistive bases are installed. For both dark current and relative gains, the same reference tube (serial number CA0017) is used. Position of the reference tube is always the same. Its gain as a function of high voltage is measured several times and these measurements result in a standard deviation of about 10-15%. It has a gain of 5×10^4 at 1100 V. Its dark current at this voltage is about 0.003 nA.

A set of seven PMTs to be tested are installed in the remaining positions. High voltage for all the tubes is set to 1100 V, which is the nominal HV for 5×10^4 gain. Then we wait until the dark current for the reference tube reads about 0.003 nA. Then the data acquisition program written in LabView reads the dark currents for all the seven tubes using a Keithley picoammeter. Program switches between

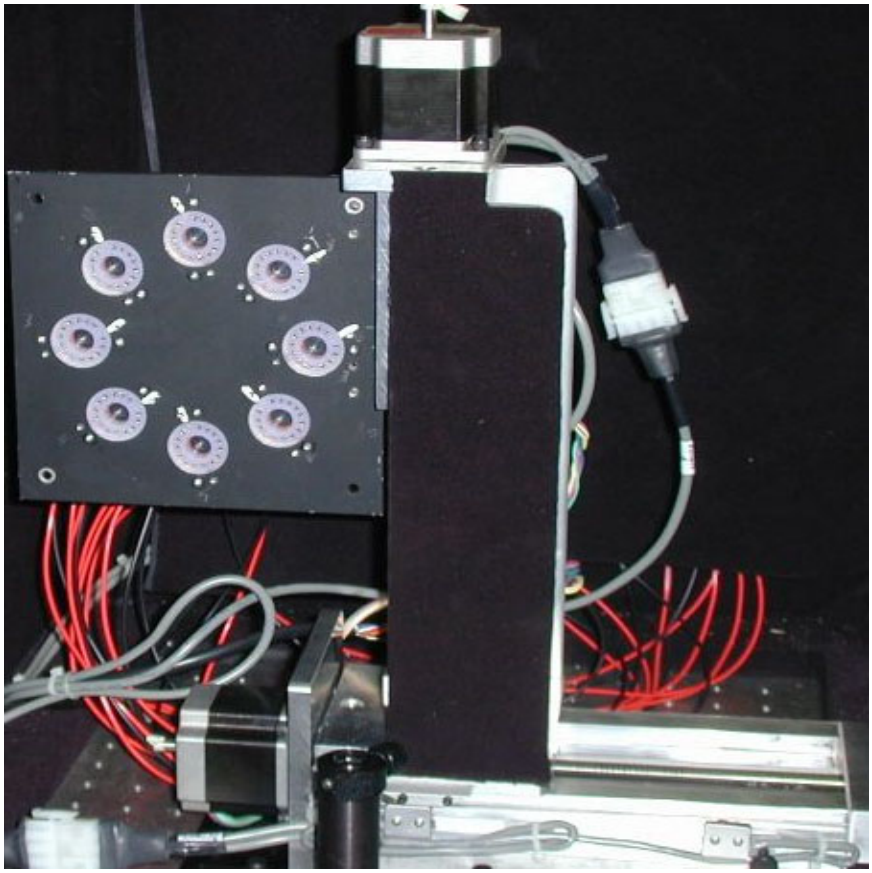

Figure 3.13: The PMT-holder used for dark current, relative gain measurements.

the seven tubes with the help of a switcher (custom built at the University of Iowa). Ten readings at 0.5 second intervals are taken and the average of these ten readings is recorded. If there is a reading that seems to be very high, another reading is taken after waiting for some additional time. This dark current measurement is probably a more stringent test than the standard way of measuring the dark current by waiting for at least half an hour for the tube to settle down.

Dark current distribution (Fig.3.14) shows that majority of the tubes are below 1 nA, which is below the value (2 nA) in the HF requirements (Table 2.1).

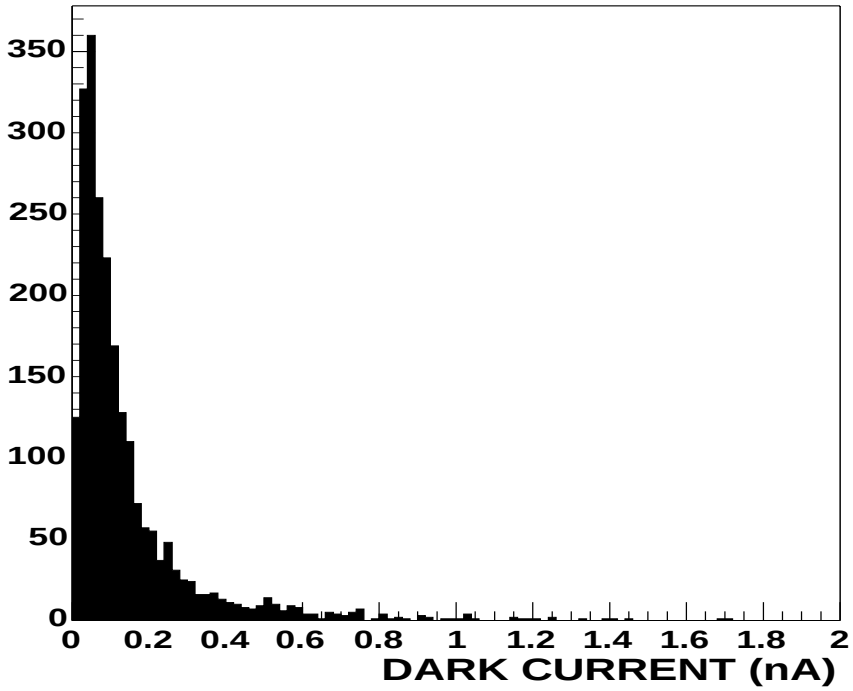

Figure 3.14: Dark current distribution of all the PMTs tested.

After the dark current measurements, tungsten lamp at the other end of the dark box is turned on. There is a NDF (factor = 3) and a blue filter in front of the lamp. The distance between the lamp and the holder is 90 cm. Lamp is rated for 6 V but operated at 5 V to ensure a stable light intensity. Light intensity over all the

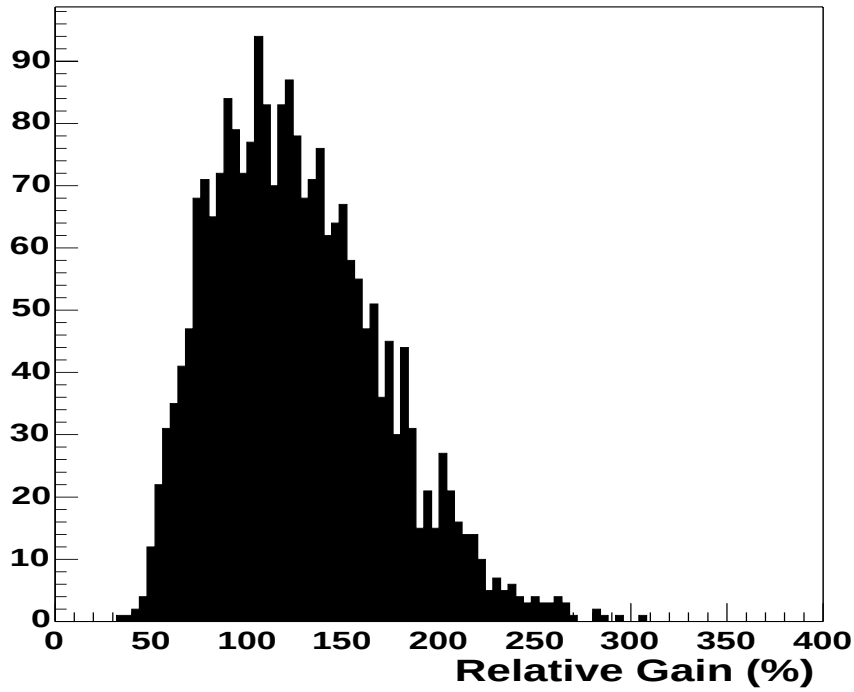

Figure 3.15: Relative gain distribution of all the PMTs tested.

PMT positions in the holder is almost the same within about 2%. Anode currents for all eight tubes, including the reference tube, are measured as explained above and recorded. Percentage relative gain (with respect to the reference tube) for each tube to be tested is calculated from these values and recorded. Current ratio of a specific tube to the reference tube is the relative gain. Relative gain defined this way is actually a combination of gain and quantum efficiency of the tube. For this reason, the histogram seen in Fig. 3.15 shows a broader distribution. The statistical uncertainty or the fluctuations in the reference tube also broadens the distribution.

3.3.4 Sampling Tests

The following tests take longer to perform. We have decided to do these measurements only on a sample of tubes. By studying the results of these measurement,

we can understand the specific operational characteristics of the tubes better. However, we will not be using the results of these measurements to accept or reject a tube.

We use the first dark box or the timing dark box for double pulse linearity and single photoelectron spectrum (SPES) measurements. Detailed gain versus high voltage measurements, the relative quantum efficiency calculations, and horizontal and vertical scans of the photocathode surface are done in the second dark box or the relative gain dark box. In addition to these tests, we have kept a few tubes under a controlled light intensity to measure their half-life. We have a separate third dark box completely for this purpose.

3.3.4.1 Gain versus High Voltage

PMT gain is defined as the ratio between the anode and the cathode currents. Gain usually depends on the dynode characteristics, number of dynodes, voltage applied on the PMT and the voltage between individual dynodes, etc. It depends on the overall high voltage roughly as:

$$Gain = AV^B \tag{3.1}$$

where A and B are just constants and V is the high voltage applied on the tube. By measuring the anode and cathode currents at varying high voltages and then calculating the gain, we can obtain a set of gain versus high voltage values. When these data are plotted logarithmically, we see almost a straight line. The slope of the straight line in this logarithmic plot is the parameter B in the above expression. The Figure 3.16 shows the change in the gain values of about 220 PMTs with respect to the high voltage. This plot gives $A = 1.155 \times 10^{-14}$ and $B = 6.143$.

During the gain versus HV measurements we went up to 10^6 gain, but due to the restrictions on the read-out electronics the HF calorimeter is going to run the

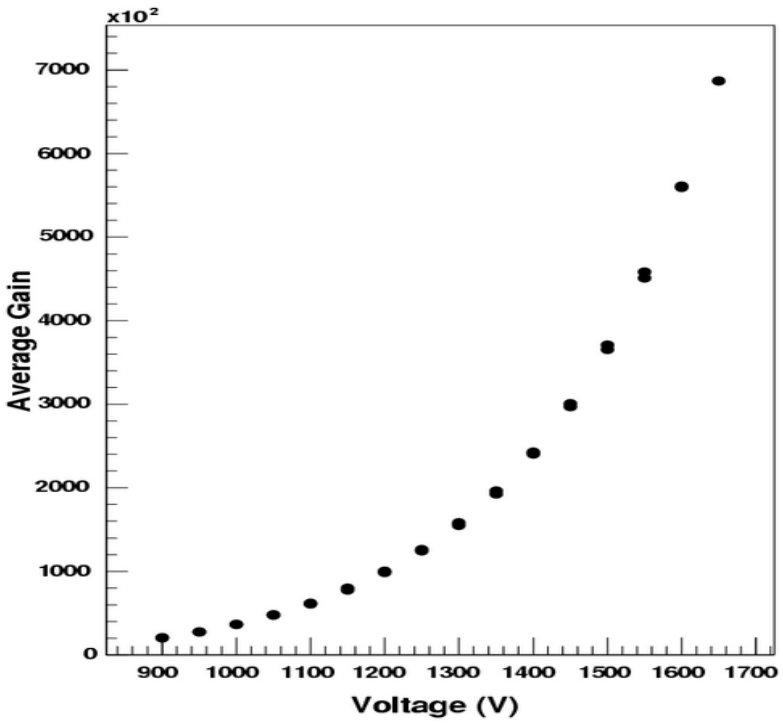

Figure 3.16: The gain of 220 PMTs versus high voltage.

PMTs at lower gains (5×10^4). The Figure 3.17 gives the gain distribution of the 220 PMTs at 1100V, the mean value is 6×10^4.

These measurements are performed by using two PMT holders. Each one is identical in shape but holds different bases. One has eight standard Hamamatsu bases and the other has eight simpler homemade bases for measuring the cathode current. In these homemade bases, all the dynodes and the anode are connected together, practically shorting the anode and all the dynodes except the first one. This way we can easily measure the cathode currents by applying the corresponding voltages between the cathode and the first dynode. For each high voltage applied to the anode-cathode circuit there is a corresponding voltage for the cathode- first dynode circuit. These voltages can be calculated by using the voltage divider ratio of the cathode-first dynode and the cathode anode resistor circuit. Keeping the light intensity constant is important to reduce the systematic effects even though it

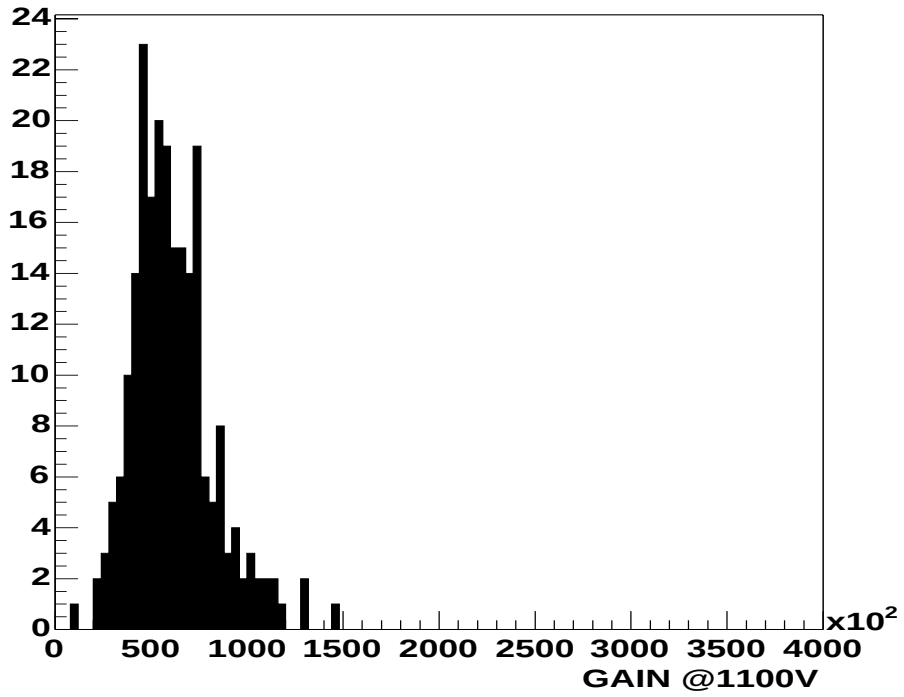

Figure 3.17: The gain of 220 PMTs at 1100V.

cancels in the calculation. Supplying a constant voltage to the tungsten light bulb that we use and positioning the PMT holders exactly the same way for both types of measurements ensure more or less a constant light intensity.

3.3.4.2 Relative Quantum Efficiency

We performed relative gain tests on every PMT, and gain versus HV tests on 220 PMTs. The relative gain of the PMT is combined result of its quantum efficiency and gain properties. In our PMT Test Station we do not perform quantum efficiency tests but by using the relation 3.2 we can find the ratio of 220 PMTs' quantum efficiencies with respect to that of reference PMT (CA0017). We call this ratio Relative Quantum Efficiency (RQE).

$$RQE = \frac{QE_i}{QE_{ref}} = \frac{RG_i \times Gain_{ref}}{RG_{ref} \times Gain_i} \tag{3.2}$$

Where QE_i and QE_{ref} are the quantum efficiencies of PMT i and reference PMT, respectively, and RG_i is the Relative Gain of the PMT i. The RG_{ref} is taken as 100%.

The results showed that the quantum efficiency value of the PMTs does not vary as much as the gain values. Our conclusion is confirmed by the manufacturer.

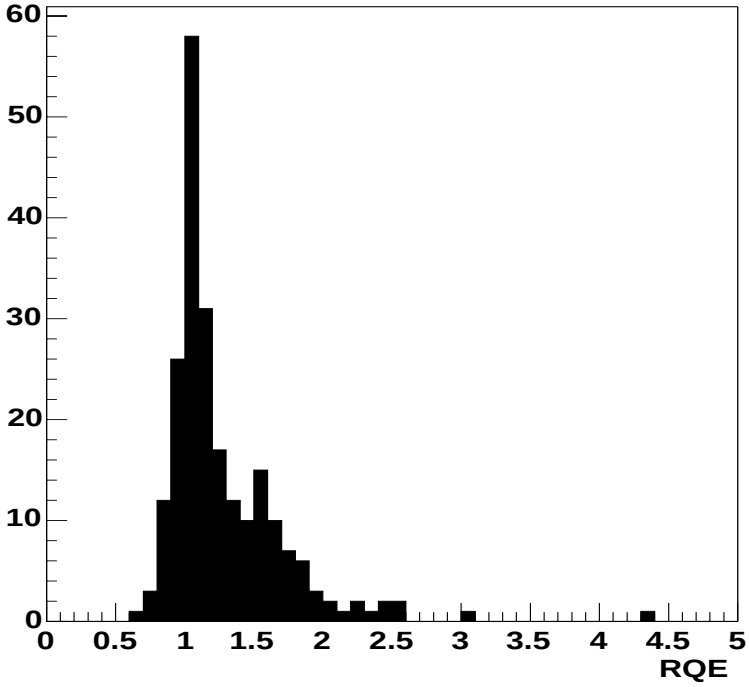

Figure 3.18: Relative quantum efficiencies.

The distribution of the relative quantum efficiencies for 220 PMTs is shown in figure 3.18.

3.3.4.3 Spatial Uniformity

Another test performed in the relative gain dark box is the horizontal and vertical scans or x-y scans. The HF requirement for the x-y uniformity is about 30%. Spatial uniformity is initially thought to be important since 24 fibers will be

bundled and read out by the same phototube. It is essential to get the same value for the same light intensity whether the light shines on one specific location on the photocathode surface or another. Otherwise, the overall energy resolution of the calorimeter will be worse. A single PMT is placed on the x-y scanner so that its first dynode is oriented horizontally. Our x-axis is along the first dynode and y-axis is perpendicular to that. x-y scanner can move the tube horizontally and vertically according to the commands issued from the data acquisition program. An opaque sheet made of black kapton is placed right in front of the tube and a 3-mm diameter circular hole drilled into it. This sheet does not move. The phototube currents are integrated with the help of a LeCroy 2249A ADC controlled by the LabView program. Scanner moves the tube in 1.25 cm steps at a time in both directions. At every position, 200 readings are taken and averaged. These averages, plotted as a function of position are displayed in Figure 3.19 for one tube (CA0058).

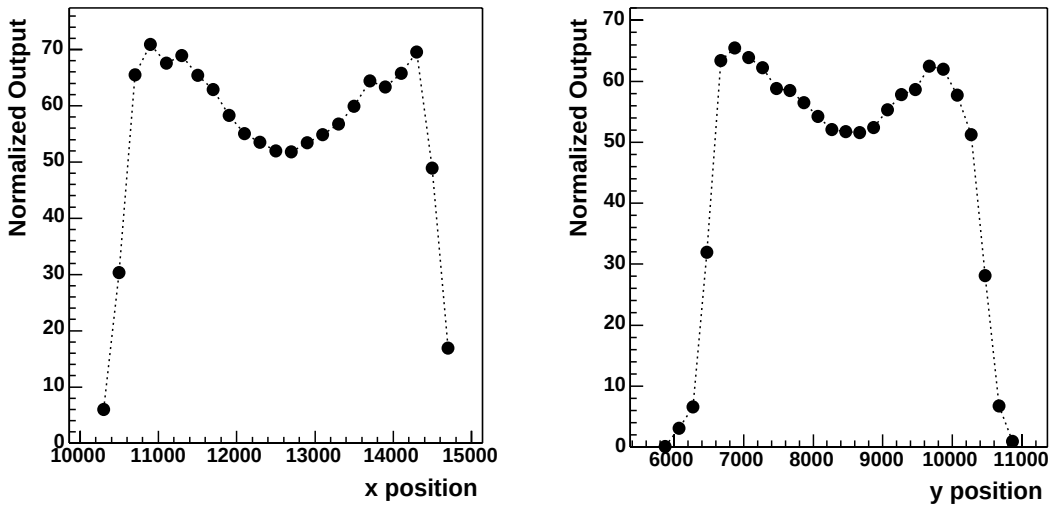

Figure 3.19: The x and y direction spatial uniformities.

A small sample of measurements resulted in spatial nonuniformities of less than 20%, which is better than the HF requirement. However, since we will be

using a 42-cm light pipe between the fiber bundle and the PMT, light coming from different fibers will be diffused enough by the time it reaches the photocathode surface so that spatial variations will have very small effect [23] [28] [29].

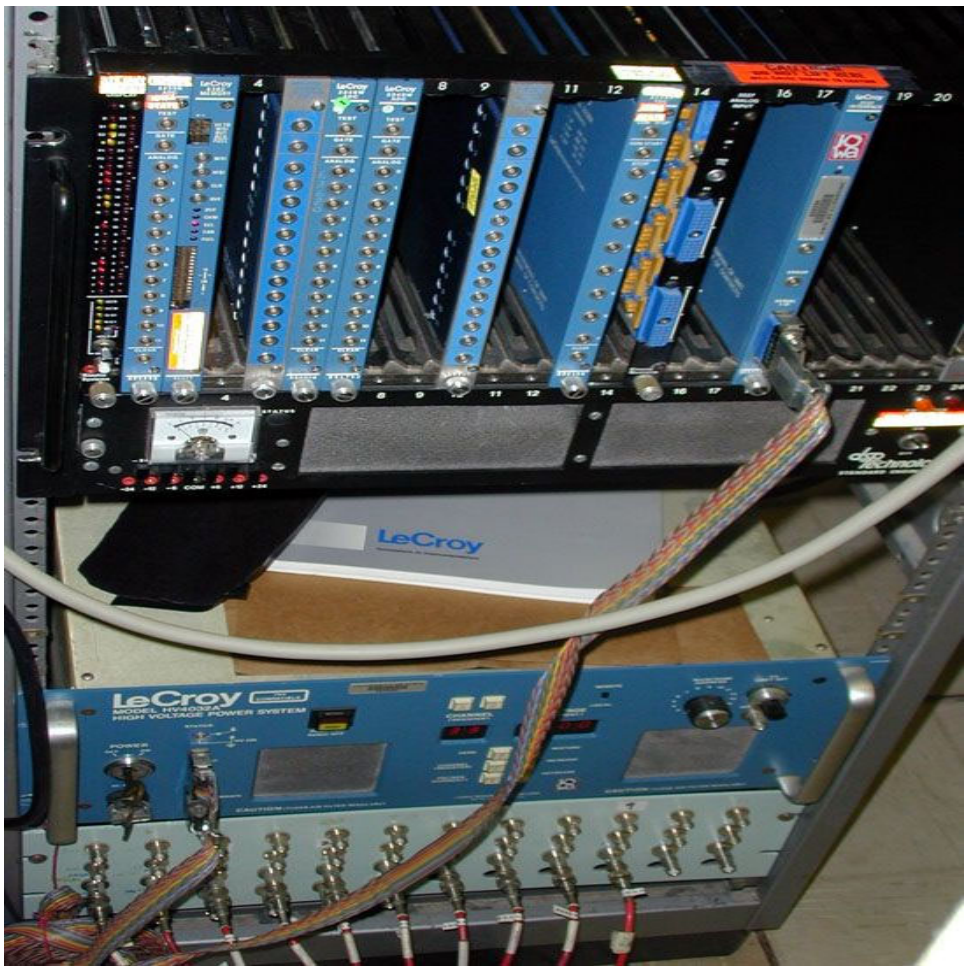

Figure 3.20: The CAMAC system and the HV power supply used in PMT Test Station.

3.3.4.4 Single Photoelectron Resolution

In principle, current gain for a PMT should be constant. However, when we look into how a PMT amplifies the photoelectrons, we see that the amplification factor might have some uncertainty due to the statistical nature of the amplification process.

A single photoelectron emitted from the photocathode surface will produce some number of secondary electrons from the first dynode and these will generate more electrons from the second dynode and so on until all the electrons reach the anode. On the average a specific number of electrons are released from each dynode surface when an electron hits. However, the actual number of electrons released each time is not constant. It fluctuates according to a Poisson process. Since the number of electrons generated at each dynode fluctuates respectively, the total number of electrons reaching the anode shows a distribution for single photoelectrons. Even though the width of the distribution for multiple a photoelectron case is equal to the single photoelectron width divided by the square root of the number of photoelectrons, it is still no negligible. So the better the single photoelectron resolution is, the better the overall PMT resolution. To achieve a good energy resolution for the calorimeter, it is important to use PMTs with good single photoelectron resolutions.

There are a few parameters that define the single photoelectron spectrum (SPES). We can either use the mean amplitude (or the centroid of the spectrum) and peak to valley (P/V) ratio or the single photoelectron resolution (SPER). The centroid is the weighted average of all the amplitudes including the noise and photoelectrons inelastically backscattered from the first dynode. Peak to valley ratio is the ratio of the peak height to the valley. Peak mentioned here is the peak corresponding to single photoelectron events. Valley is the local minimum between this peak and the lower peak caused by noise and inelastic photoelectrons. SPER is the percentage ratio of FWHM to the peak position. On the other hand, HF requirements dictate a 50% or better resolution defined in terms of rms/centroid which corresponds to, since FWHM $= 2.534\sigma$ for a Gaussian, about 40% resolution value defined in our way, namely FWHM/peak position (see Fig.3.21).

Single photoelectron spectra are accumulated by using the same setup that is used in the fourth generation SPER setup shown in Fig.2.17). Details are also

given in reference [27].

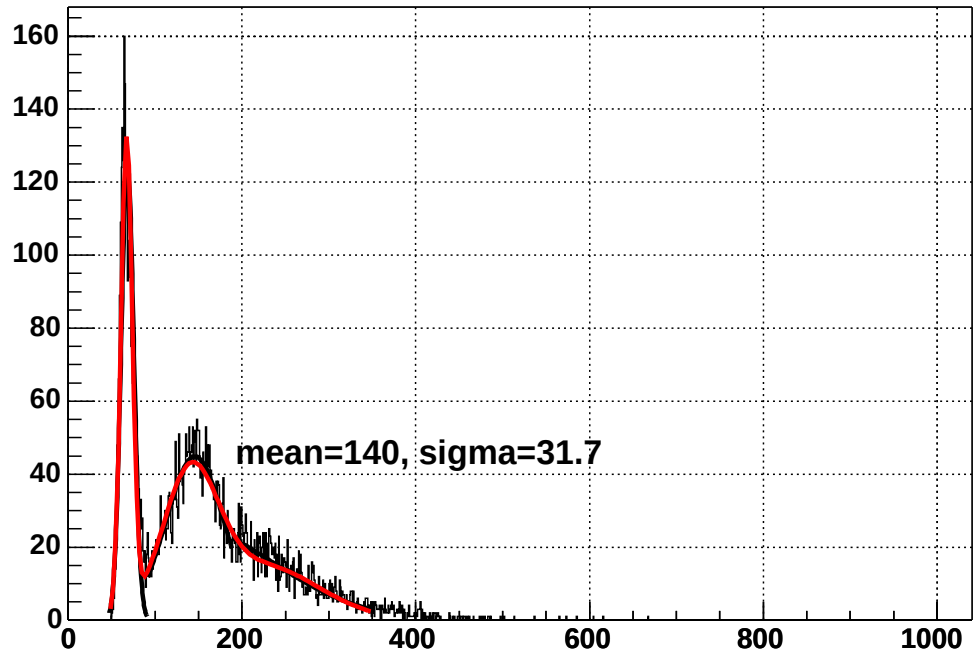

Figure 3.21: SPES of Hamamatsu R7525HA at a gain of 10^4.

The operating voltage of the PMTs in HF calorimeter will be around 1100V, so it is important to show that the PMTs have single photoelectron detection ability at this voltage. We performed SPER a test on 30 Hamamatsu R7525HA PMTs, the resulting distribution is shown in Figure 3.22, the mean of this distribution is less than 40%.

3.3.4.5 Double Pulse Linearity

Double pulse linearity measurements avoid the problems inherent in absolute determination of the light pulse intensity. They are also more relevant to our operation. In these type of measurements, there are two pulses separated well enough so that there is enough time for the PMT to recover between pulses. Light pulse

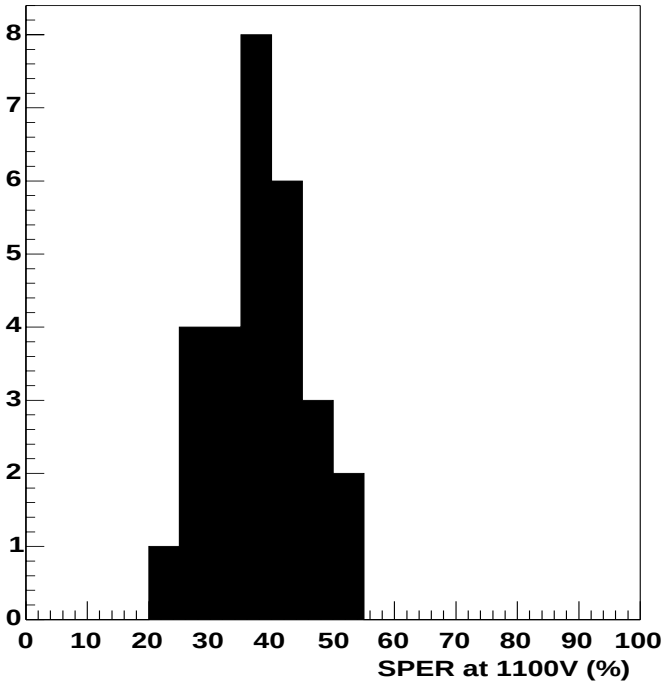

Figure 3.22: Distribution of the single photoelectron resolution of Hamamatsu R7525 PMTs at 1100V.

intensities are adjusted so that one pulse is four (or a known factor) times larger than the other. So when the tube becomes nonlinear for the larger pulse it is still relatively linear for the smaller pulse. In fact, we measure the relative or the differential linearity of a PMT in this method. When the ratio of the responses to both type of pulses are used to study the linearity, all the normalization factors for determining the light intensities will cancel out. So the nonlinearities that can be observed in the single pulse linearity measurements will not be present in double pulse linearity measurements. With the modifications we have made to the double pulse linearity measurements, this is actually a more relevant test of linearity for our detector. Instead of the large delay between the two subsequent pulses, we set the two pulses close to each other. The two pulses are separated by 25 ns, similar to the LHC beam structure. This modification actually amplifies the effect of tube

recovery on the linearity.

Deviation from linearity (Δ) is defined as:

$$\Delta = \frac{r - r_0}{r_0} \tag{3.3}$$

where r_0 and r are the current ratios at a very low light intensity and at other light intensities, respectively. The current ratio is

$$r = \frac{I_l}{I_s} \tag{3.4}$$

where I_l and I_s corresponds to peak currents produced in 50 Ω resistors due to large and small light pulses, respectively. At low light intensities, we expect the tubes to be linear. In principle, when we plot the deviation from linearity (Δ) as a function of the peak current due to the larger pulse, we should see a flat line at low intensities. In fact, with the exception of a slight positive deviation at low intensities, this is the case. When the intensity starts to go above a certain value, tube response becomes nonlinear and the deviation starts to increase in the negative direction. It is negative, because at higher intensities, the PMT cannot respond quickly and the space charge effects become important.

Mainly the timing setup explained above is used for the double pulse linearity measurements. However, instead of the laser, we use a blue LED (460nm) driven by an AVTECH pulser that can provide two pulses coming at 25 ns intervals. Frequency of the double pulses is set to 10 kHz. Pulser is adjusted so that the larger pulse comes first (Fig.2.23). Fig.2.24 displays a typical PMT anode signal resulted when the LED is driven by the signal in Fig.2.23. Light intensity is varied by changing the NDFs in front of the PMT (see [27] and Chap.2).

We performed double pulse linearity test on 100 Hamamatsu R7525HA PMTs. Fig.3.23 shows a sample deviation versus peak current measurement. It seems that the deviation stays below a few percent up to 70 mA. We expect the deviation to

be less than 2% up to 15 mA peak current.

Average values of the percentage deviations up to 50 mA peak currents are averaged and these double pulse linearities are histogrammed (see Fig.3.24).

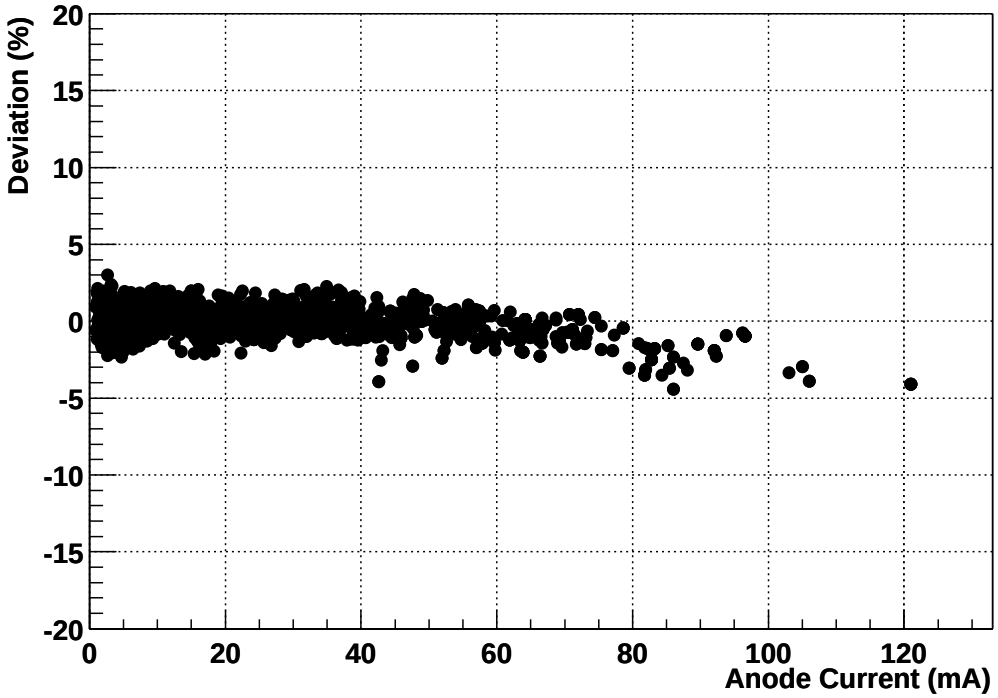

Figure 3.23: Deviation from linearity versus peak current for 100 PMTs on double pulse linearity tests.

3.3.4.6 The Lifetime Test

CMS will be operating five to ten years and maybe longer. During this whole period, every element in the detector should continue to operate within the parameters defined in the specific requirements for that part. This is also true for the PMTs. However, the PMTs will start to degrade after a while and eventually will not work within their specifications.

In our case, the lifetime is defined in terms of the accumulated charge collected from the anode when the tube gain drops to half value.

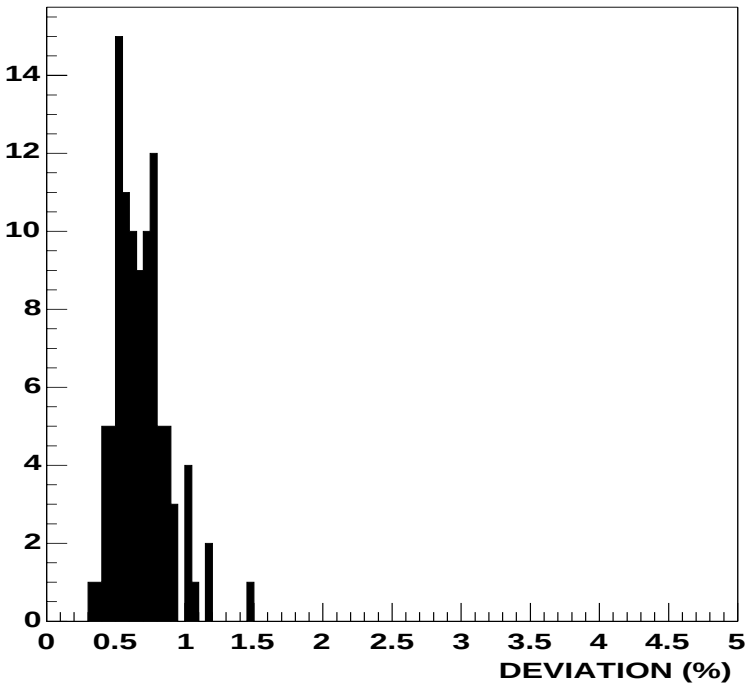

Figure 3.24: Double pulse tests, percentage deviation from linearity of the PMTs up to 50 mA peak current.

The lifetime measurements are done in the third dark box. The setup consists of a tungsten bulb as the light source and a power meter to monitor the light intensity. Phototubes are placed in the dark box and the tungsten light illuminates them. There is a neutral density filter and a blue filter (420nm) in front of the tungsten bulb. High voltage on the tubes is 1100V, which gives us a nominal gain of 5×10^4. Light intensity and phototube currents are recorded in 24-hour periods.

For 14 months we accumulated total 3000 C on one PMT (serial number CA0252) and 3250 C on the other (serial number CA0472). The gains of the PMTs were measured before and after the lifetime tests, and are shown on Figure 3.25. The gain of the PMTs dropped to 50% or less of the initial values, with around 3000 C of charge accumulation. In 10 years of operation CMS we are expecting around 1500 C.

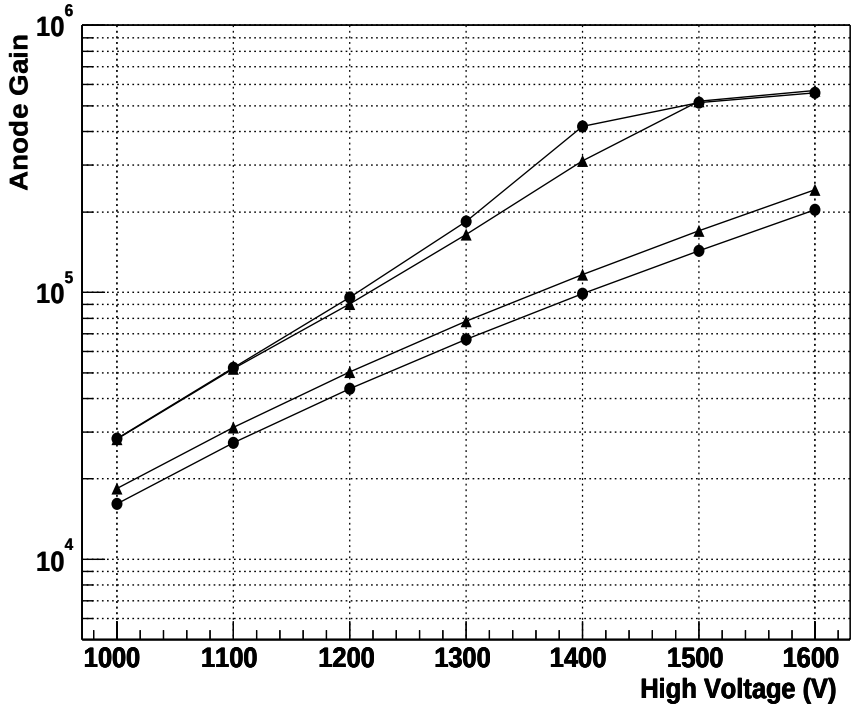

Figure 3.25: Gain versus HV values of the two PMTs before and after the lifetime test.

CHAPTER 4
SELEX (E781) EXPERIMENT

E781, SEgmented LargE X baryon spectrometer (SELEX), was a Fermilab experiment. It was commissioned and run during the 1996-97 Fermilab fixed target program. The collaboration composed of 115 physicists and 20 institutions from USA, Russia, Turkey, Brazil, China, Germany, Israel, Mexico, UK and Italy. The main goal of the SELEX experiment was to produce high statistics of charm baryon decays containing at least one charm quark using a variety of incident beam particles and targets. The SELEX experiment was composed of a five stage spectrometer: Beam, Vertex, M1, M2, M3. Each spectrometer, other than Vertex which is designed to create high resolution tracking near target, contained a bending magnet.

4.1 SELEX Physics Reach

SELEX experiment has a wide physics program which included both charm and non-charm physics topics.

4.1.1 Charm Physics Program

The main goal of the SELEX experiment is to study charm baryon production and decay mechanisms. The data set that SELEX has can be very useful to understand the perturbative and non perturbative QCD mechanisms. Production of heavy quarks can be described by the perturbative QCD, but the hadronization of heavy quarks is non-perturbative process. The complete particle identification of hadrons, electrons, and gammas makes it possible to normalize branching ratios to the semileptonic rates. SELEX also has the ability to measure π^0 and η^0 states which helps in analyzing these ratios for evidence of resonant substructure, a dominant feature of meson decay.

The SELEX experiment can study charm hadroproduction in three different

beams: Σ^-, π^- and p beams, which makes it a unique experiment. The experiment was designed to detect decays in the wide momentum range ($x_F > 0.1$), where x_F is approximately the fraction of the beam momentum carried by the charm particle. Study of the large x_F region is especially valuable, because that is the region where charm and anti-charm particle production differs the most [30].

In the SELEX experiment we study x_F and P_t distributions for charm and anticharm particles, charm-anticharm production asymmetry [31]. The SELEX experiment also plans to study production of charm excited states, as well as charm pair production.

The production polarization of the charm baryons is similar to hyperons and is predicted by some models. A study of this effect is an important input in the understanding of heavy quark production and hadronization dynamics. Experimental data on this question is very limited [32].

Having a large sample of charm decays allowed us to do precision measurements of charm lifetimes. For control of systematic errors it is important that the lifetimes of all stable charm particles be measured in the same apparatus. These lifetimes provide a valuable input to test the Heavy Quark Expansion calculations

Another important topic is the study of new decay modes and their branching ratios. Theoretical calculation of branching ratios of explicit decays of heavy quarks is still one of the most challenging areas of hadron physics. Experimental input is vital to understand decay dynamics.

The state-of-the-art particle identification system in the SELEX greatly helped in the study of Cabibbo-suppressed decays. These studies investigate the role of final state interactions in hadronic decays. The SELEX experiment was the first experiment to observe the decay $\Xi_c^+ \to pK^-\pi^+$ [33]. Semi-leptonic charm decays are theoretically better understood than hadronic decays, and new experimental data can push theoretical calculations to new levels of accuracy.

The majority of charm excited states can be detected and measured in the SELEX experiment. We plan to study excited state characteristics, such as mass and width. For example, the mass splitting of Σ_c and Λ_c^+ is an important test of HQET [34]. Widths of excited states are valuable input to HQET, and there is little experimental data available [35]. Confirmation of Ξ_c' states observed only by CLEO [36] would be an important accomplishment. We also plan to search for new excited states, especially for charm baryons.

4.1.2 Non-Charm Physics Program

The hadronic total cross section is one of the most fundamental measurements of the strength of hadronic interactions. The total cross section initially decreases as a function of center of mass energy, and after about 10 GeV starts to grow again. SELEX measured Σ^- and π^- total cross sections on beryllium, copper, carbon and polyethylene targets. Also the total cross section was measured for protons on beryllium and carbon targets [37]. All measurements were done at 600 ± 50 GeV beam energy. These data were used to extract Σ^--p and π^--p total cross sections. This is the highest energy Σ^--p total cross section measurement. The previous highest energy measurement was done at 140 GeV [38]. The measurements clearly showed a rise of the Σ^--p cross section as a function of the center of mass energy.

The charge radius provides information about the internal structure of hadron. This measurement is important to verify models which describe confinement of quarks inside the hadron. Different theoretical calculations of charge radii give quite different answers and experimental input can clarify the situation [40]. Charge radii of π^-, Σ^-, p were measured in the SELEX experiment by studying π^--e [39] Σ^--e [40] and p-e [41] scattering.

The discovery of the interaction of an unpolarized proton beam with unpolarized target which produced polarized hyperons in 1976 came as a complete surprise [42]. Even after 24 years extensive experimental data still remain widely unexplained [43]. Hadronization is expected to play a major role in this process. SELEX measured production polarization of Σ^+ [44] and Λ^0 [45] as a function of x_F and p_T.

Other topics of the non-charm physics program include Primakoff production of excited states, pion polarizability, chiral anomaly tests and search for exotic states.

4.2 SELEX Apparatus

4.2.1 Detector Overview

The heart of the experiment was the Vertex Silicon Strip Detector (SSD) capable of $4\,\mu$m transverse position resolution at 600 GeV. The vertex separation L was measured with precision $\sigma_L \simeq 0.5\,$mm . It is very important to have small a error on vertex separation, as its significance L/σ_L is by far the most powerful cut to separate the charm signal from the background.

The SELEX experiment had an extensive particle identification system. Beam particles ($\Sigma^-/\pi^-, p/\pi^+$) were tagged with the Beam Transition Radiation Detector (TRD). The 3000 phototube Ring Imaging Cherenkov Counter (RICH) was used to identify the secondary particles: electrons, muons, pions, kaons, protons and even hyperons. The RICH detector was capable of K/π separation up to 165 GeV. The separation of the kaons from the pions is a vital feature for any charm experiment, because charm decays usually have kaons in the final state. The Electron Transition Radiation Detectors (ETRD) were used to separate electrons from the hadrons, which is important for the semileptonic decay physics. Three lead glass detectors were used to identify and measure the energy of the photons and electrons.

SELEX also has a precise tracking system and 3 analyzing magnets to measure particle momentum. Eight Beam SSD planes with hit resolution $\sigma \sim 6\,\mu$m were used to measure track parameters. The downstream tracking system included 26 proportional wire chambers (PWC) planes with hit spatial resolution $\sigma \sim 0.6 - 1\,$mm. It also included three Vector Drift Chambers (VDC) each having 8 sensitive planes with hit resolution $\sigma \sim 100\,\mu$m. And finally there were 18 large SSDs with hit resolution $\sigma \sim 14\,\mu$m to measure very high-momentum tracks. In total SELEX the SSD system has 74,000 strips (see Fig.4.1).

4.2.2 SELEX Coordinate System and Spectrometers

The origin of the coordinate system is chosen to be in the middle of the downstream surface of the downstream target (Figure 4.2). The z-axis is along the beam direction, the y-axis is vertically up and the x-axis completes a right-handed coordinate system. Most detectors measured tracks in x, y projections, or in u, v projections, which form $\pm 45^0$ angle with respect to x, y axis.

The beam spectrometer included apparatus between the exits of the hyperon magnet and target region. The vertex spectrometer was between the targets and M1 magnet. The M1,M2,M3 spectrometers were located after the corresponding analyzing magnets.

4.2.3 Analyzing Magnets

SELEX apparatus has 3 analyzing magnets that were used to measure track momentum. The magnetic fields for each magnet were measured with a flip-coil apparatus that determined B_x, B_y and B_z components on a 1-inch grid with a precision of 0.1%. These maps were used to propagate the particle tracks inside the magnets. Main parameters of the magnets are summarized in Table 4.1.

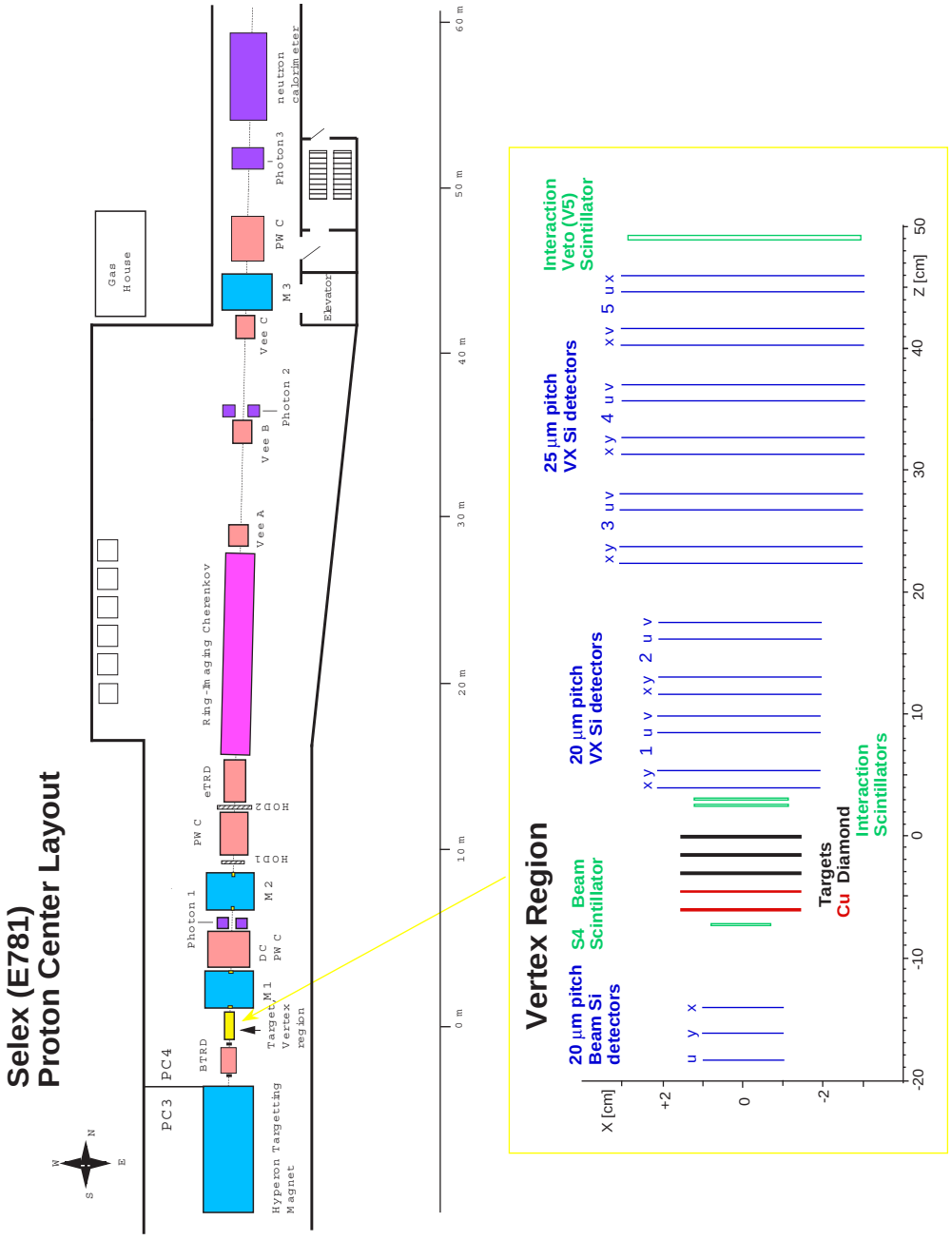

Figure 4.1: Schematic view of SELEX spectrometer and vertex region.

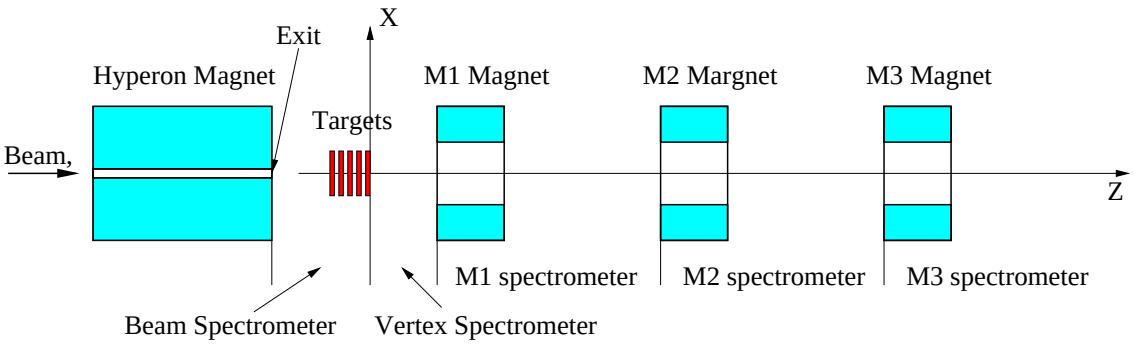

Figure 4.2: Schematic view of SELEX spectrometers (Off-scale).

name	z	aperture	B	p_t
	[cm]	$[cm] \times [cm]$	[kG]	[GeV]
M1	190	61 x 51	11.98	0.73
M2	745	61 x 25	14.66	0.84
M3	4240	61 x 51	6.85	0.42

Table 4.1: Parameters of magnets.

4.2.4 Beam Spectrometer

The beam spectrometer consisted of the hyperon production target, the hyperon magnet (see Fig.4.3), the beam particle identification detectors, beam tracking detectors and the scintillators which were used for the trigger.

4.2.4.1 Hyperon Production Target

800 GeV protons from the Fermilab Tevatron accelerator hit $1 \times 2 \times 400\text{mm}^3$ (one interaction length) beryllium target. The forward going secondary particles enter a narrow 7.3m long curved channel inside the 3.5T hyperon magnet that only allows the particles with high energy ($600 \pm 50\,\text{GeV}$) to go through. The radius of the curvature of this tungsten channel was 619m. At the target region, the 600 GeV negative secondary beam consisted of approximately 50.9% π^-, 46.3% Σ^-,

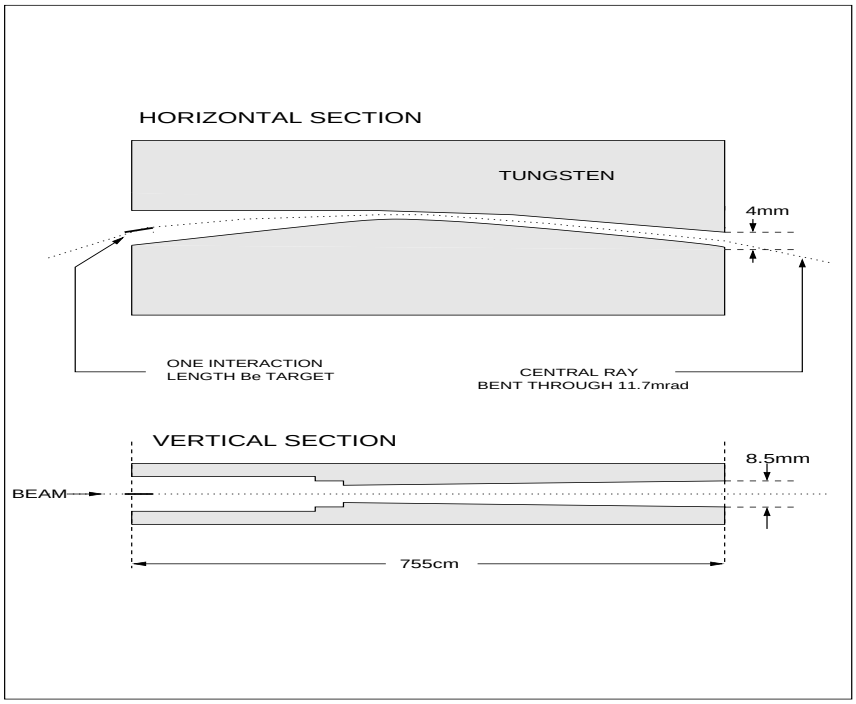

Figure 4.3: Schematic layout of the hyperon beam magnet.

1.6% K^- and 1.2% Ξ^-. With the opposite polarity of the magnetic field secondary beam consisted of approximately 89.2% protons, 5.7% π^+, 2.7% Σ^+ and 2.4% K^+. Once the beam left the hyperon magnet, it passed through the Beam Transition Radiation Detectors (BTRD).

4.2.4.2 Beam Transition Radiation Detectors

Particles in the hyperon beam were tagged in the 10 Beam Transition Radiation Detectors (BTRDs). Each BTRD has a radiator made of 200 polypropylene foils 17 μm thick three proportional chambers filled with the mixture of Xe + 30% CH4 gas to detect transition radiation [47].

A relativistic particle crossing the boundary of media with different dielectric constants emits transition radiation photons. Typically the energy of such photons is a few keV. The probability of radiating those photons proportional to Lorentz γ

factor (i.e. the energy) hence particles with the same energy but different masses produces different numbers of hits. This enables the identification of relativistic beam particles at high energies (see Fig.4.4).

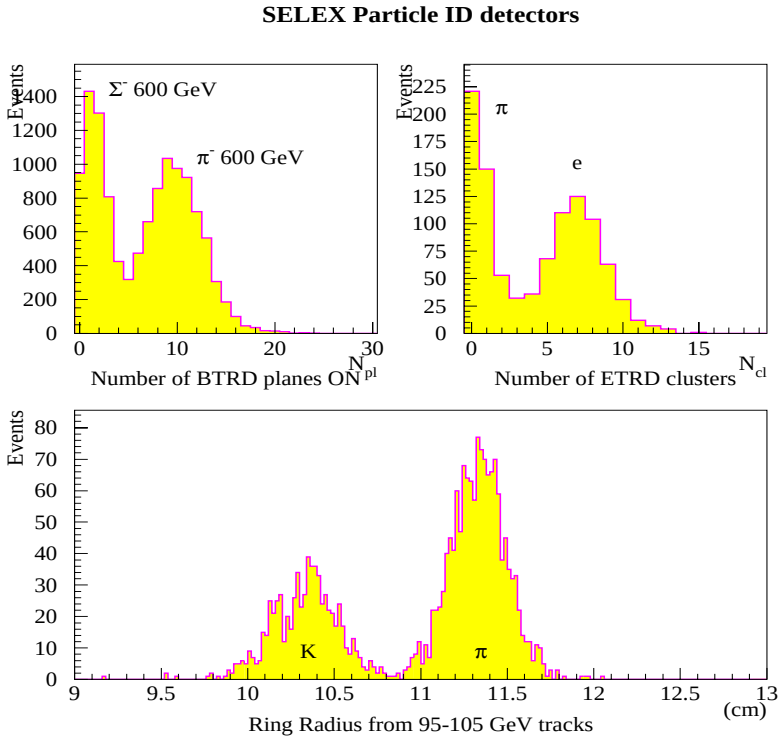

Figure 4.4: Particle ID separation ability of SELEX.

The position of the beam tracks in the charm targets were measured with eight planes of 20 μm pitch Beam Silicon Strip Detectors (SSD) with 4 μm resolution. Each SSD has 1024 strips read out by SVX chips and has 2x2 cm2 sensitive area. The beam tracks, which triggered the interactions were identified by four 50 μ pitch hardware scattering trigger silicon detectors (HSD) [16]. The beam track candidates were extrapolated from the Beam SSD to the HSD planes. The track that had two or more matching hits in the HSD was identified as the trigger beam track. The beam particles interacted in five targets with combined interaction length 4.3%. Target spacing was 1.5 cm.

Beam TRD information was used in the T1 trigger to increase the fraction of Σ^- beam particles in the recorded interactions.

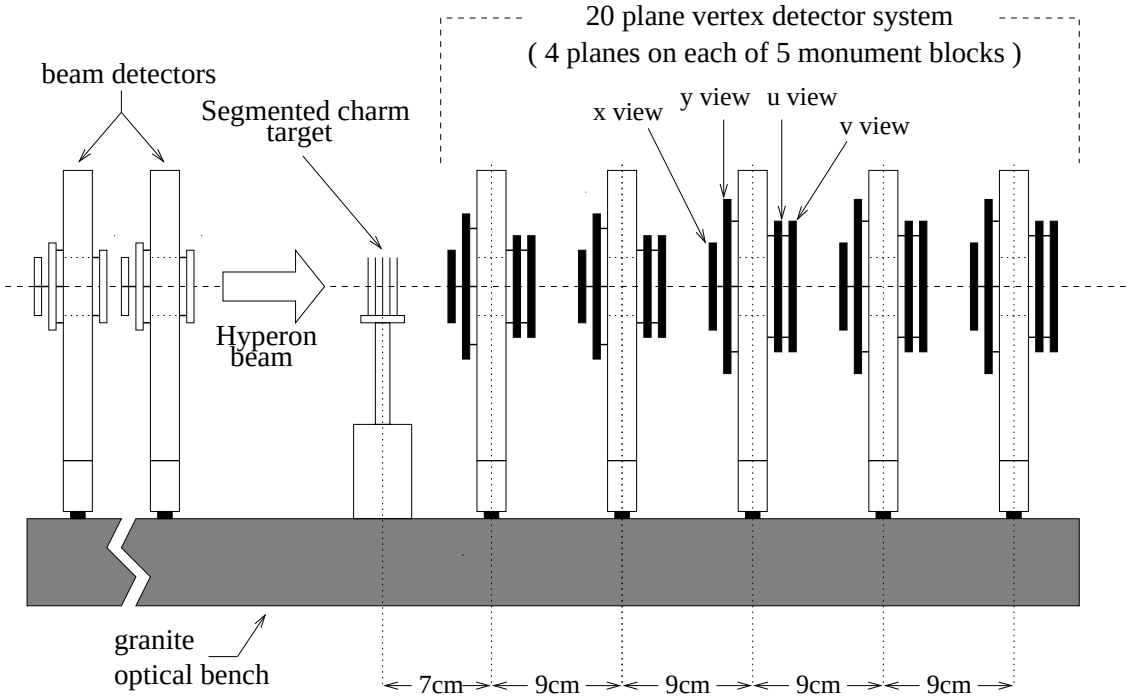

Figure 4.5: Beam and vertex silicon layout.

4.2.4.3 Hardware Scattering Trigger Silicon Detectors

The Hardware Scatter Trigger (HST) detector was composed of six silicon detectors placed after the targets, and before the M1 magnet. The silicon detectors had 50 μm-pitch strips and short 80 ns gates which allowed only the hits from the triggering beam particle to be read. These detectors were installed for Primakoff physics and used as a supplement to the other detectors for tracking purposes. Beam track candidates were extrapolated from the Beam SSD to the HSD planes. The track that had 2 or more matching hits in the HSD was identified as the trigger beam track [48].

4.2.4.4 Beam Silicon Strip Detectors

Beam tracks were measured with 8 planes of 20 μm pitch silicon strip detectors (SSD). Beam SSDs determined position of the beam track in the charm targets with about 4 μm resolution. Each detector has 1024 strips read out via 8 SVX chips and has 2×2 cm sensitive area. The detectors were mounted on three stations with stations 1 and 3 containing 3 detectors and station 2 containing 2 detectors. The hit efficiency for a single detector was $> 98\%$ with overall tracking efficiency of $> 95\%$. Because the integration gate of the readout electronics was set up to 10μs long, information about several beam tracks from the 1 MHz beam was stored in the beam SSD hit output. The beam track which triggered the event was identified using the hardware scattering silicon detectors and also using hit information from the vertex SSD.

4.2.4.5 Charm Targets

Beam particles interacted in 5 targets with combined interaction length 4.3% for protons. The 1.5 cm target spacing was set along the beam line so as to allow the determination of the target in which the interaction occurred. The targets were removed from the beam line remotely to allow the alignment data to be taken using the non-interacted beam tracks.

Target properties are summarized in Table 4.2. Different materials were used to study charm production as a function of A.

4.2.5 Vertex Spectrometer

The Vertex spectrometer starts at the downstream end of the last target and ends at the middle of the M1 spectrometer. It is consisted of 20 Vertex Silicon Strip Detectors (SSDs), mounted to five station, four SSDs at each. 300μm thick single sided SSDs detected the secondary tracks with high spatial resolution. The

target	material	thickness [mm]	z [cm]	Atomic number A	Density [g/cm^3]	Inter length [%]
1	copper	1.6	-6.13	63.5	8.96	1.06
2	copper	1.1	-4.62	63.5	8.96	0.76
3	diamond	2.2	-3.10	12	3.20	0.82
4	diamond	2.2	-1.61	12	3.20	0.82
5	diamond	2.2	-0.11	12	3.20	0.82

Table 4.2: Charm target properties.

first 8 detectors, called 5-cm detectors, have 20 μm pitch and $5.1 \times 5.0\,\mathrm{cm}^2$ active area. The downstream 12 detectors, called mosaic detectors, have 25 μm pitch and $8.3 \times 9.6\,\mathrm{cm}^2$ active area. The detectors were mounted on special granite optical bench, and measured tracks in x, y, u and v projections (see Figure 4.5). Five-cm type detectors read out every strip in the $3.1 \times 5.0\,\mathrm{cm}^2$ middle area of the detector, where the hit density is the largest. On the edges they have every-other strip readout, because the hit density is quite small there and only low energy tracks, which resolution is dominated by multiple scattering, can hit that region. Mosaic detectors were build out of three $8.3 \times 3.2\,\mathrm{cm}^2$ pieces of silicon. The detector in the middle has every strip readout, and the two edge detectors have every other strip readout.

Each of the detectors has greater than 98% hit detection efficiency and spatial resolution about 6.5 μm (see Figure 4.6 [46]).

The Beam silicon, Vertex silicon, charm targets and the trigger scintillators were enclosed in a light tight aluminum box for RF shielding.

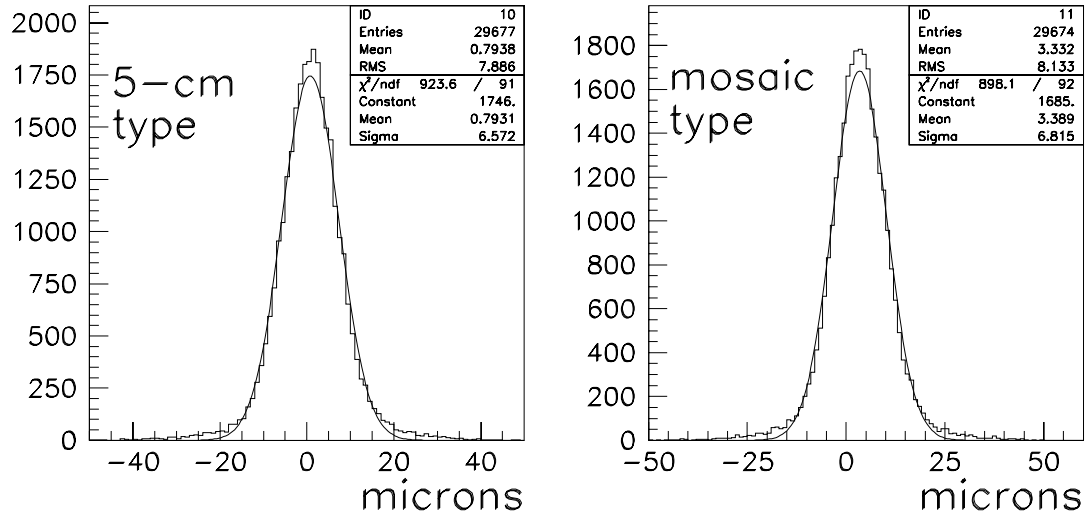

Figure 4.6: Typical resolution of vertex detectors.

4.2.6 M1 Spectrometer

.

The M1 spectrometer consisted of M1 magnet and the detectors between M1 and M2 spectrometers. The M1 spectrometer was designed to analyze the particles from 2.5 to 15 GeV/c momentum range. The M1 magnet was operated with a field strength of 1.35 T giving a Pt kick of 0.74GeV/c. The particles with momentum value below 2.5 GeV/c were swept aside by M1 magnet. The tracking in the spectrometer was done by Multiwire Proportional Chambers, Drift Chambers and Large Area Silicon Strip Detectors and there were Lead Glass Electromagnetic Calorimeters placed at the end of the spectrometer.

4.2.6.1 Large Area Silicon Strip Detectors

There were 3 stations of Large Area Silicon Detectors (LASDs) located at the end plates of M1 and M2 magnets therefore they were designed to function

correctly in the fringe magnetic field (Fig.4.7). Each LASD consisted of two single-sided silicon strip detectors (SSD) and two double-sided silicon strip detectors. The double-sided SSDs had 50 μm strip pitch and $3.2 \times 2.6\text{cm}^2$ sensitive area. Double-sided SSDs measured hits in x and y projections. The single-sided SSDs with 50 μm strip pitch and $3.2 \times 3.2\text{cm}^2$ sensitive area and they measured hits in u and v projections. Detectors have 95-99% hit detection efficiency and the spatial resolution about 15 μm [39], [49]. Including the LASDs the total silicon system accounted for approximately 74,000 channels of readout in the experiment.

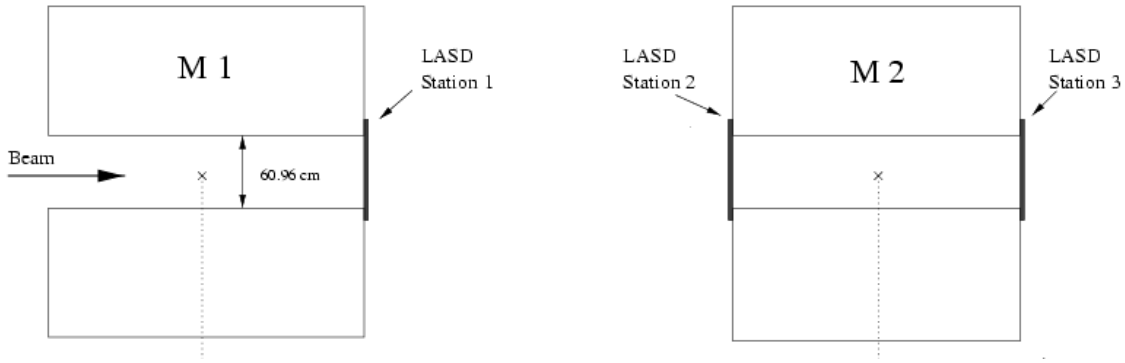

Figure 4.7: Position of the three LASD stations.

4.2.6.2 Multiwire Proportional Chambers

The M1 Multiwire Proportional Chambers (PWC), were designed to track the 'softer' particles from the interaction. The PWCs consisted of equally spaced anode wires centered between the cathode planes. In M1 spectrometer there were 3 PWCs with 3 mm wire spacing and about $2 \times 2\,\text{m}^2$ active area. The chamber was filled 'magic gas'(75% argon, 24.5% isobutane, and 0.5% freon). Each chamber has 4 sensitive planes in 4 projections (Figure 4.8). Chambers have greater than 90% hit detection efficiency with 0.9 mm spatial resolution.

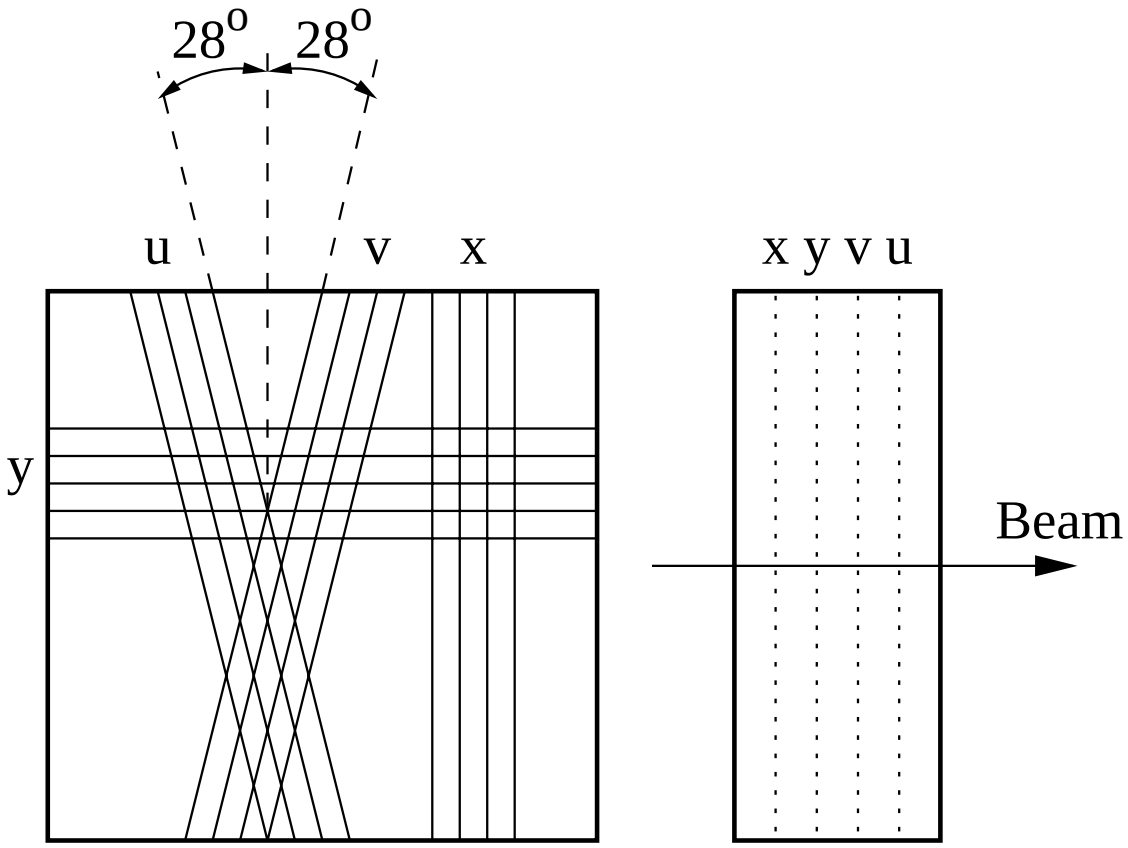

Figure 4.8: Schematic layout of M1 PWC chamber.

4.2.6.3 Drift Chambers

There were 2 drift chambers placed between the M1 PWCs. Each drift chambers had 2 sensitive planes measuring hits in x projection. Chambers have $2.4 \times 1.7\,\mathrm{m}^2$ acceptance, they are about 80% efficient and has about 0.7 mm resolution [50].

4.2.6.4 Lead Glass Electromagnetic Calorimeters

There were three electromagnetic calorimeters positioned at the end of M1, M2 and M3 spectrometers (Figure 4.1). The Cherenkov radiation created by the charge particles in the calorimeters were collected by the photomultiplier tubes (pmts). Each calorimeter has a hole in the middle to let beam and high energy particles through. Lead glass has density $4.1\,\mathrm{g/cm}^3$ and radiation length 2.5 cm. One advantage of using lead glass calorimetry was their radiation hardness. The first 2 calorimeters were composed of blocks of 2 different sizes, smaller size blocks $4.25 \times 4.25 \times 34\,\mathrm{cm}^3$ covering inside of the detector and bigger size blocks $8.5 \times 8.5 \times 34\,\mathrm{cm}^3$ covering the outside of the detector [51]. The third calorimeter was built out of the same size blocks $3.8 \times 3.8 \times 45\,\mathrm{cm}^3$ [52].

4.2.7 M2 Spectrometer

.

The M2 spectrometer was designed to track, and identify the particles with momentum higher than 15 GeV/c. The M2 spectrometer composed of the M2 magnet and all the detectors between M2 and M3 magnets. The M2 magnet had the magnetic field of 1.54 T which corresponds to a Pt kick of 0.845 GeV/c.

4.2.7.1 Hodoscopes

There were two hodoscopes in the M2 spectrometer that used scintillation counters to give a fast response on the sign, number and the momentum of the particles passing through the spectrometer. This information was used by the trigger in deciding whether to trigger on an event. The hodoscopes consists of three regions covering the negative-charge, central and positive-charge regions of the M2 spectrometer. Sign of the charge was assumed based on the region on the detector. The spectrometer bent the negatively charged particles to the right as they traveled down the beam line.

4.2.7.2 Multiwire Proportional Chambers (PWC)

Most of the tracking in the M2 spectrometer was done using the M2 PWCs and the M2 drift chambers. There were 7 PWCs with 2 mm wire spacing in the M2 spectrometer. The 3 upstream chambers have a $60 \times 60\,\mathrm{cm}^2$ active region and filled with magic gas. The 4 downstream chambers have a $60 \times 100\,\mathrm{cm}^2$ aperture, these chambers also used a form of magic gas.(see Figure 4.9). Each chamber has 2 sensitive planes in 2 orthogonal projections. The chambers have greater than 95% hit detection efficiency with 0.6 mm spatial resolution [53].

4.2.7.3 Electron Transition Radiation Detectors

The Electron Transition Radiation Detectors (ETRDs) were designed to give good electron identification. There were 6 ETRDs, in the M2 spectrometer, and each used 200 sheets of 17 μm polypropylene foils, positioned in front of chambers, to generate the transition radiation. The radiation was detected by $103 \times 63\mathrm{cm}^2$ MPWC chambers with 4 mm wire spacing and filled with the mixture of Xe and methane [53]. The electrons have much higher γ-factor, then the same energy π, thus they have a larger number of clusters in TRD chambers, compared to π The

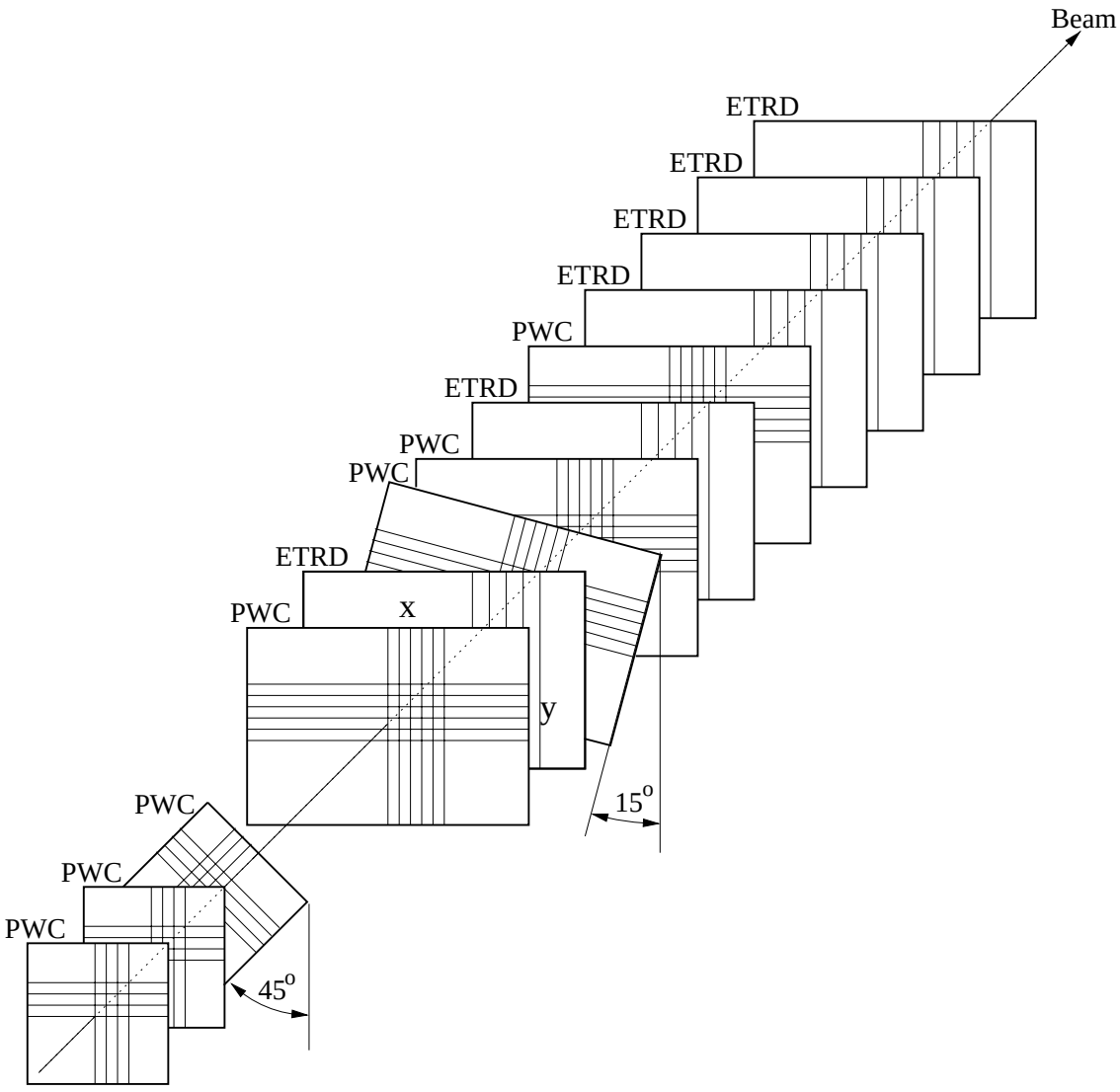

Figure 4.9: Schematic layout of M2 PWC chamber.

ETRDs were most efficient at distinguishing between the electrons and pions around 20 GeV/c momentum, which was 95%, for higher electron momentum the efficiency was 91%. (see Figure 4.4).

4.2.7.4 Ring Imaging Cherenkov Counter

The E781 Ring Imaging Cherenkov Counter (RICH) detector was the major particle identification device in the apparatus. Particles passed through 10 m long vessel filled with Ne gas, noble gas to provide a clean signal, emitting Cherenkov radiation along the way (see Figure 4.10). The downstream end of the vessel consisted of 16 hexagonally shaped spherical mirrors of total area $24m \times 1.2m$ with focal length of 10m. The mirrors were used to reflect the Cherenkov radiation back to 2848 phototube array forming rings on its surface.

The ring radius grows with the velocity of the particle (Figure 4.11). The $\beta = 1$ particle has a ring radius of 11.5 cm, with 13.6 hits on the ring. Each hit was measured with spatial resolution 5.5 mm, and ring radius r was measured with $\sigma_r = 1.8$ mm resolution in multi-track events, which allowed π/K separation up to $165\,GeV$ [54]).

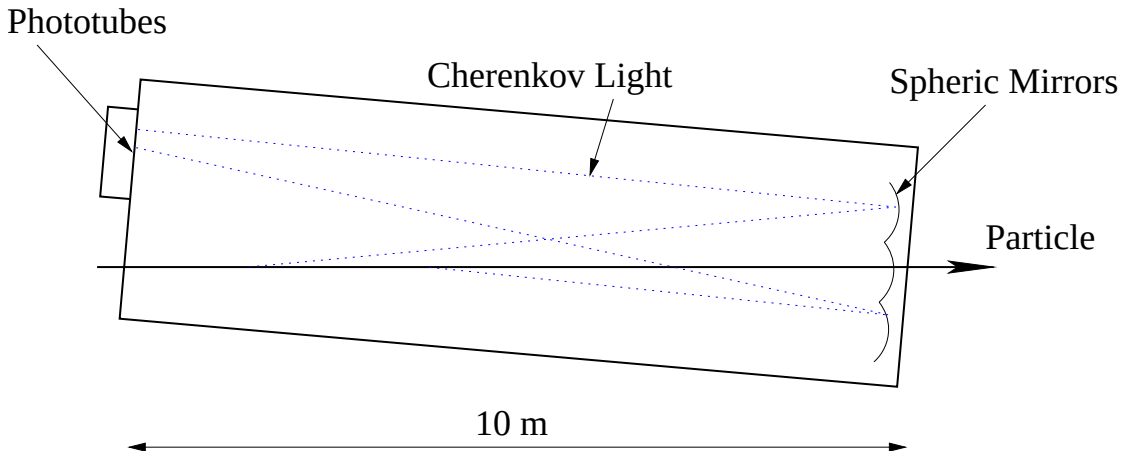

Figure 4.10: Schematic view of RICH detector.

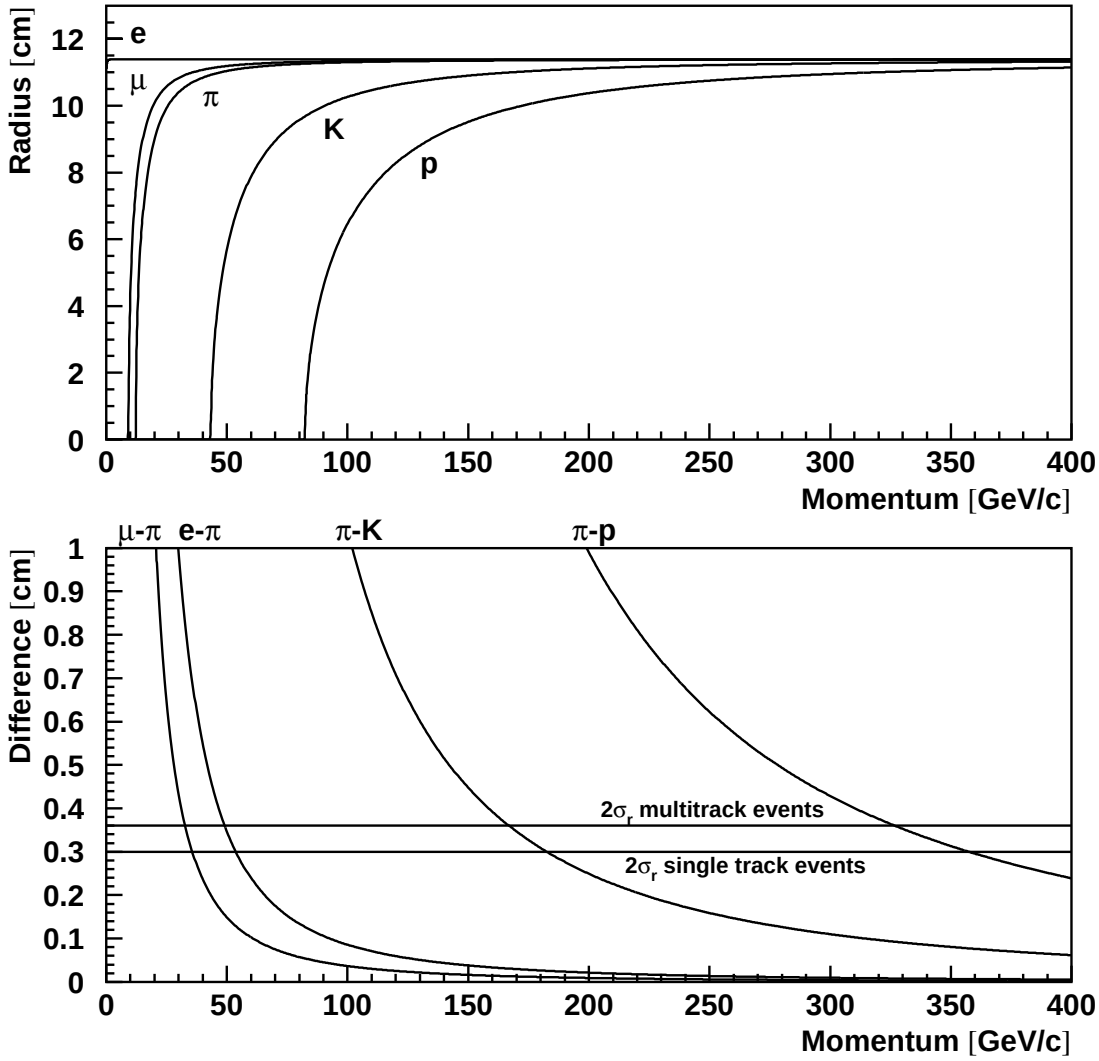

Figure 4.11: The Ring Radii and separation for different particles. The horizontal lines on the lower plot show the achieved resolutions for the single track and multiple tracks respectively.

4.2.7.5 Vector Drift Chambers

There were 9 Vector Drift Chambers (VDC) in SELEX experiment, united in 3 stations VeeA, VeeB, VeeC [55]. First 2 stations were located in M2 spectrometer and the third one in M3 spectrometer (Figure 4.1). The VDCs were designed to provide the short track segments of downstream decay products, charged particles, as well as the position information. Stations had $116 \times 116\,\mathrm{cm}^2$ aperture, about 90% efficiency and $\sim 100\mu$m resolution. The stations measured tracks in x, y, u or in x, y, v projections. Each chamber has 8 sensitive planes in the fine cells of the center region of the chamber. In the coarse cells it has 6 sensitive planes. So each chamber measured a track at 6 or even 8 points and hence measured a track vector, not just its position. After the second VDC station was the second Lead Glass Electromagnetic Calorimeter (Photon 2).

4.2.8 M3 Spectrometer

The M3 Spectrometer was the place the momenta of the decay products of long-range hyperons were measured. M3 magnet had a 1.3 T magnetic field strength providing a Pt kick of 0.72 GeV/c. The M3 spectrometer consisted of two Multiwire Proportional Chambers (PWC) of $64\times64\,\mathrm{cm}^2$, a third PWC of $115\times89\,\mathrm{cm}^2$, followed by a vector drift chamber and a lead glass electromagnetic calorimeter.

4.2.9 Neutron Calorimeter

The last detector in SELEX apparatus is the Neutron Calorimeter (NCAL). The NCAL was designed to distinguish between beam particles and the decay product neutrons. The NCAL consisted of 50 scintillator planes sandwiched between 50 iron sheets and 17 PWCs.

4.2.10 Trigger and Data Acquisition System

The primary goal of the SELEX is to study the production and decay of charm baryons at high Xf. The main trigger configuration was called the charm trigger. One of the biggest challenges of charm experiments, other than vertex displacement, is the events with charm particles do not have distinctive kinematic features. The charm mass is not big enough to make an efficient trigger on events with large transverse momentum p_T, which is common in b-physics experiments. Most charm experiments use very loose triggers [56, 57] , selecting just events with interactions. SELEX also used an open trigger requiring an interaction in the targets.

The trigger system in SELEX used a set of scintillation counters (S1-S4), veto counters (VH1,VH2), interaction counters (IC) and 2 hodoscopes (H1,H2) shown on Figure 4.12.

The charm trigger had three levels of hardware trigger, referred to as T0, T1 and T2. The first level trigger, T0, defined a beam particle as the coincidence of S1,S2,S4 counters with no hits in veto counters VH1 and VH2. Trigger T1 required existence of T0 trigger, an interaction in the targets, a signal from the Beam TRD and 2 hits in the positive region of the H1 [58], [59]. The third level trigger T2 was formed by a coincidence of T0, and some signals from slower detectors like Vee Scintillators, Photon3, and downstream TRD.

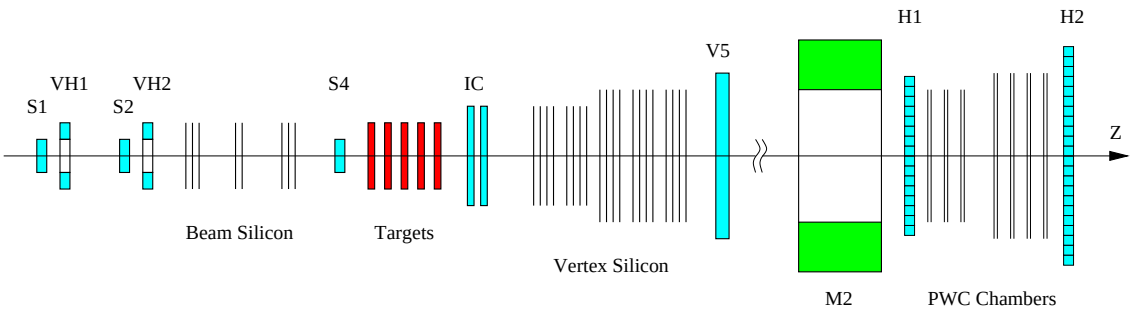

Figure 4.12: Schematic view of SELEX trigger elements

If an event passed the trigger, it was digitized, packed and read out into dual-ported memories [59]. There were about 80000 events read out in each 20-second spill. They were processed in 40-second periods between spills by a 17-processor SGI Challenge computer by the SELEX Online Filter code. The Online Filter passed about 1 event in 8. These events were written out to disk. Events on disk were sampled by the monitoring program to check the apparatus performance during data-taking. The size of one event was about 6.5 kB. Events from disk were combined in 200 MB files, which were written to tapes and stored for the further processing. SELEX charm trigger rates are summarized in Table 4.3.

trigger/beam	definition	rate
proton beam	800 GeV protons from Tevatron	$4 \cdot 10^{10}$ Hz
Σ^-/π^- beam	600 GeV secondary beam	600 kHz
T0	$\mathrm{S1} \cdot \overline{\mathrm{VH1}} \cdot \mathrm{S2} \cdot \overline{\mathrm{VH2}} \cdot \mathrm{S4} \cdot \mathrm{V5}$	20 kHz
T1	$\mathrm{T0} \cdot (IC > 3) \cdot \mathrm{BTRD} \cdot (\mathrm{H1}, \mathrm{H2} > 2\,\mathrm{pos})$	4 kHz
Online filter	Event has more than just a primary vertex	500 Hz

Table 4.3: SELEX charm trigger rates.

One of the innovations of the SELEX experiment was the online filter. This is a program which ran between the beam spills and processed data to reject events that did not have evidence for a secondary vertex.

CHAPTER 5
Ξ_C^+ LIFETIME ANALYSIS

5.1 Charm Baryon Overview

There are number of theoretical works that have focused on calculation of the lifetimes of charm hadrons. However the experimental results are very limited. Lifetime of a particle gives us information about its decay dynamics.

Lifetime measurements of the charm baryons help to determine the contributions on non-spectator weak interaction effects like W-annihilation and W-exchange process without the helicity suppression that limits their role in charm meson decays.

From point of view of Heavy Quark Effective Theory and Perturbative QCD, the charm baryon lifetimes can be expressed in terms of a set of matrix elements that contain the corrections to the fundamental expansion of the decay amplitude in terms of $1/m_c$ [60] [61]. We present a new measurement from hadro-production data taken by the SELEX (E781) experiment at Fermilab.

Experimental measurements of charm particle lifetimes have been used in the study of strong interaction physics. The measurements provide some guidance for theoretical calculations of non-perturbative strong interaction process. The steady improvement in the precision of the measurements has not only helped to improve our theoretical understanding of the strong interactions, but also to help stimulate the development of better theoretical tools. These have progressed from the spectator model to various quark models and currently to Heavy Quark Expansion methods [62]. These calculation tools are the same or similar to those used in the other areas, for example to determine the size of the V_{ub} CKM element through inclusive semileptonic B decays [63]. More precise measurements of all the charm particle lifetimes will help continue this process of improvement and extension of

applicability. Precise charm lifetime measurements are now beginning to emerge from e^+e- collider experiments [64]. The effects of lifetime and vertex resolution are also important in mixing and CP violation experiments [65] [66]. It is crucial to have accurate lifetime measurements from fixed target experiments to act as a standard to evaluate any relative systematic differences.

The lifetime hierarchy of the weakly decaying charm mesons is well established [67]. However, the pattern of the predicted lifetimes for the weakly decaying charm baryons agrees only qualitatively with the experimental results. Interestingly baryon sector lifetime measurements provide information on quark interference and W-exchange. The essential difference from the mesons is that W-exchange among the valence quarks of the baryon is neither color nor helicity suppressed. The measured lifetime is larger than the theory predicts, but there is a large experimental uncertainty. A more precise measurements could be conclusive in testing predictions in this sector.

Charm baryon lifetime measurements provide insight into the dynamics of nonperturbative heavy quark decays. The theoretical situation is rich with possibilities. Unlike the case of charm mesons the exchange mechanism is not helicity suppressed and therefore can be comparable in magnitude to the spectator diagram. In addition the color suppression is only active for particular decay channels. Thus spectator decays alone cannot account for the hadronic width in charm baryon decay. The hadronic width is modified by at least three effects: (a) destructive interference between external and internal spectator diagrams, (b) constructive interference between internal spectator diagrams, and (c) W-exchange diagrams. Effects (a) and (b) are expected to be operative in the decay of the Ξ_c^+, (a) and (c) play a role in Λ_c^+ decay. While several models [68] [69] can account for the apparent lifetime hierarchy $\tau_{\Xi_c^+} > \tau_{\Lambda_c^+} > \tau_{\Xi_c^0} > \tau_{\Omega_c^0}$, experimental results are necessary to advance our understanding of the various contributions to the hadronic width. The lifetimes of

charm baryons are not measured as precisely as those of charm mesons (D^0, D^+, D_s), which are measured, by individual experiments [70] [71], to a precision of $1-3\%$. The Λ_c^+ lifetime is the first [72] [73] [74] [75] and the most precisely measured of the charm baryons. Recently FOCUS, CLEO, and SELEX measured the precision of 5% [76] [77] [78]. After Λ_c^+, Ξ_c^+ [79] [80] [81] [82], and Ξ_c^0 [83] [84] lifetimes were measured. First Ω_c^0 lifetime measurements [85] [86] followed them.

Recently the charm baryon lifetimes (Ξ_c^+, Ξ_c^0, and Ω_c^0) are measured to $15-30\%$ uncertainty [87] [88] [89] [90] [91] [92].

The total decay rate for a charmed hadron is determined by three contributions:

$$\tau_{Tot} = \tau_{SL} + \tau_{FL} + \tau_{Had} \tag{5.1}$$

τ_{FL}, the fully leptonic decay rate, is zero for baryons and small for mesons due to helicity suppression. τ_{SL}, the semi-leptonic rate is expected to be the same for all the mesons, but enhanced for charmed strange baryons. τ_{Had}, the hadronic decay rate is the primary source of the difference between the decay rates for the various charmed species. Several different contributions to τ_{Had} must be considered. In the meson sector, it is experimentally observed that the D^0 is much shorter lived than the D^+. This difference is primarily due to destructive interference between the internal spectator decay (which is helicity and color suppressed in mesons)and the external spectator decay. This interference arises due to the presence of two $\overline{d}$ quarks in the final state. Similarly, the D_s^+ and D^0 lifetimes should be similar except for the effects of W-exchange (for D^0) and W-annihilation (for D_s^+, but helicity suppressed) [93]. The measurement of the ratio $\tau_{D_s^+}/\tau_{D^0}$ can shed light on the relative strength of these contributions. In the baryon sector, the situation is even more interesting. First, the semi-leptonic decay rates of the charmed strange mesons are expected to be enhanced due to the presence of two s quarks in the final state. Additionally, the

presence of a u valence quark in baryons leads to destructive interference with the external spectator decay, while the presence of an s valence quark in the strange-charmed baryons gives rise to constructive interference. These contributions are not color or helicity suppressed, so they play a larger role in baryon decays. Finally, the W-exchange process is not helicity suppressed in baryons and is found to be very important in calculating the Λ_c^+ and Ξ_c^0 lifetimes. This brief discussion has considered only Cabibbo-favored processes, but recent calculations have begun to consider Cabibbo-suppressed processes as well with encouraging results.

Charm Baryon	Lifetime (Bag Model)	Lifetime (NMR Model)
Ξ_c^+	0.44 ps	0.37 ps
Λ_c^+	0.37 ps	0.23 ps
Ξ_c^0	0.28 ps	0.15 ps
Ω_c^0	0.28 ps	0.14 ps

Table 5.1: Theoretical results for lifetimes.

Weak decays of hadrons depend on the fundamental parameters of the Standard Model, in particular on the KM parameters and quark masses. It is very important to have a reliable measurement on their values from data, but it is not theoretically or experimentally easy. On the lifetimes of singly charmed weakly decaying baryons B.Guberina, R.Ruckl and J.Trampetic obtained the predictions summarized in Table 5.1 using the Bag Model of the baryon wave function and using the Non-Relativistic Model for baryon wave function. The predictions of B. Blok and M. Shifman on the lifetimes of charm baryons are given in Table 5.2.

Charm Baryon	Lifetime
Ξ_c^+	0.28 ps
Λ_c^+	0.22 ps
Ξ_c^0	0.10 ps
Ω_c^0	0.09 ps or 0.071 ps

Table 5.2: Theoretical results for lifetimes.

5.2 SELEX Ξ_c^+ Data

The first charm baryon lifetime analysis of SELEX experiment was on Λ_c^+ [78] with PassI data. SELEX Experiment has observed the Cabibo-Suppressed Ξ_c^+ decay at passI analysis [33]. In PassII the mass window for $\Xi_c^+ -> p^+K^-\pi^+$ increased so we can have sidebands on both side of the signal to understand the behavior of the background better. The Cabibbo-favored decay channels, $\Xi_c^+ -> \Sigma^+K^-\pi^+$ and $\Xi_c^+ -> \Xi^-\pi^+\pi^+$ were observed and well established in PassI analysis, In PassII we increased the significances of the samples by different sets of cuts and reduced the background level for a better lifetime analysis.

5.3 Event Selection

So as to understand the behavior of Ξ_c^+ sample under different cuts we did the Monte Carlo study first. We created the perfect events of three channels with QQ, then embedded these events into SELEX data by SOAP. Then we converted the reconstructed events into ROOT files. We used these Monte Carlo events for cut optimization study. We scanned all the possible cut values to see where we can maximize the significance. This process has been done for every decay channel in this analysis, the cut optimization results for $\Xi_c^+ -> \Xi^-\pi^+\pi^+$, $\Xi_c^+ -> p^+K^-\pi^+$, and $\Xi_c^+ -> \Sigma^+K^-\pi^+$ are given in Section A.1.

$$Significance = S_{mc}/\sqrt{S_{data} + B_{data}} \tag{5.2}$$

Where S_{mc} is the number of signal events on the Monte Carlo events after the cut is applied, S_{data} and B_{data} are the signal and the background events in the signal region of the real data sample, respectively. Signal region is defined to be the $\pm 20 MeV/c^2$ around the mean mass value.

The cut we used or considered to use are;

(i) L/σ_L : L is the distance between the primary and the secondary vertices (see Fig 5.1). Since the charm baryon angles of deflection are very small, around 10 mrad, $L = z_{sec} - z_{prim}$ is an excellent approximation. The secondary vertex position is defined by the fit of the secondary vertex tracks to the common vertex. The primary vertex position is defined by the fit of the tracks from primary vertex. The definition of σ_L is;

$$\sigma_L = \sqrt{\sigma_{prim}^2 + \sigma_{sec}^2} \tag{5.3}$$

(ii) *Pvtx* : The charm track was reconstructed as the vector sum of its secondary tracks, and this summation vector is extrapolated to the primary vertex, the misdistance with respect to the primary vertex is calculated. The misdistance divided by its error is called Pvtx, point back.

(iii) *Scut* : The secondary vertex tracks are extrapolated back to the z_{prim}. The second largest miss-distance with respect to primary vertex is called s_2, and σ_{s_2} is the extrapolated error, calculated using the track error matrix. Scut is defined to be s_2/σ_{s_2}. This cut suppresses the background events generated by the secondary vertex tracks extrapolated back to the primary vertex.

(iv) ΣP_t^2 : Sum of the squared transverse momentum of the secondary particles with respect to the charm track.

(v) P_{π^+} : The momentum of the π^+ is required to be greater than some value

this cut helps to reject the soft pion that cause high background.

(vi) *Smin* : Smin is the very similar to the Scut, but Smin gives the spatial distance for the second biggest misdistance in unit of cm. In Pass1 analysis Smin was applied to the Ξ_c^+ sample (see [33]), but in Pass2 sample we found Scut more powerful to reduce the background.

(vii) χ^2 : In the reconstruction package the second vertex reconstruction was attempted when the χ^2 per degree of freedom (χ^2/dof) for the fit of ensemble of the tracks to a single primary vertex exceeds 5. We did not need to apply this cut again in the analysis code, it was already applied as a default value in reconstruction package.

(viii) x_f : When the Feynman x distribution of the particles are required to be higher, we tend to reduce the background by eliminating the soft particles. This cut is powerful to reduce the background but we did not include it in out cut sample for lifetime analysis.

(ix) *RICH probability* : For the decay channels that has protons, sigmas and kaons we required the RICH identification probability of these particles to be equal or greater than pion probability.

(vi) Δz_{tgt} : Most of the events in the experiment were not charm, but rather secondary interactions in the targets, where tracks could accidentally form a mass close to a charm mass. Removing events which have a secondary vertex z_{sec} close to one of the targets significantly reduced that background. This cut discriminate against secondary interactions and multiple scattering effects. So, for some of the decay channels we required the secondary vertex z position to be at least $500\mu m$ away from the closest target.

To separate the charm signal from non-charm background we required;

For $\Xi_c^+ -> \Xi^-\pi^+\pi^+$ sample: $L/\sigma > 9$, $Pvtx < 2.5$, $Scut > 6$, $\Sigma P_t^2 > 0.2$, $P_{\pi^+} > 6GeV/c$. These cuts give us 157 ± 21 $\Xi_c^+ -> \Xi^-\pi^+\pi^+$ events, see Fig. 5.8.

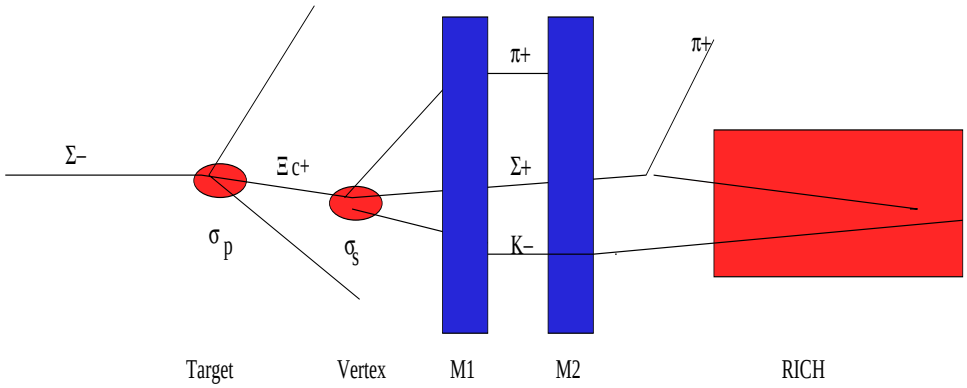

Figure 5.1: An example of a charm event topology and selection in SELEX.

For $\Xi_c^+ -> p^+K^-\pi^+$ sample: $L/\sigma > 8$, $Pvtx < 2.5$, $Scut > 6$, $\Sigma P_t^2 > 0.2$, $P_{\pi^+} > 6GeV/c$, the RICH identification probability of protons and kaons are required to be equal or greater than pion probability, and the secondary vertex z position is required to be at least $500\mu m$ away from the closest target. These cuts give us 98 ± 17 $\Xi_c^+ -> p^+K^-\pi^+$ events, see Fig. 5.9.

For $\Xi_c^+ -> \Sigma^+K^-\pi^+$ sample: $L/\sigma > 10$, $Pvtx < 5$, $Scut > 6$, $\Sigma P_t^2 > 0.3$, $P_{\pi^+} > 7GeV/c$, the RICH identification probability of Σ^+ and Kaon are required to be equal or greater than pion probability, and the secondary vertex z position is required to be at least $500\mu m$ away from the closest target. These cuts give us 46 ± 11 $\Xi_c^+ -> \Sigma^+K^-\pi^+$ events, see Fig. 5.10.

The shaded areas in Fig 5.8 and Fig.5.10 are estimated reflection from $\Lambda_c^+ -> \Sigma^-\pi^+\pi^+$ and $\Lambda_c^+ -> \Sigma^+\pi^-\pi^+$ respectively. The shapes are determined by Monte Carlo simulations and the areas are normalized to the observed number of signal events in Λ_c^+ data. The reflection plots for $\Xi_c^+ -> \Xi^-\pi^+\pi^+$ are shown in Figures 5.2 5.3 5.4. In this case we assumed that the reconstruction code will misidentify all the Σ^-s as Ξ^- and reconstructed the invariant mass with Ξ^- mass again. The mass spectrum has shifted toward Ξ_c^+ mass region. Then this Monte Carlo based distribution is normalized with respect to the data events coming from passII sample. The reflection plots for $\Xi_c^+ -> \Sigma^+K^-\pi^+$ are shown in Figures 5.5 5.6 5.7.

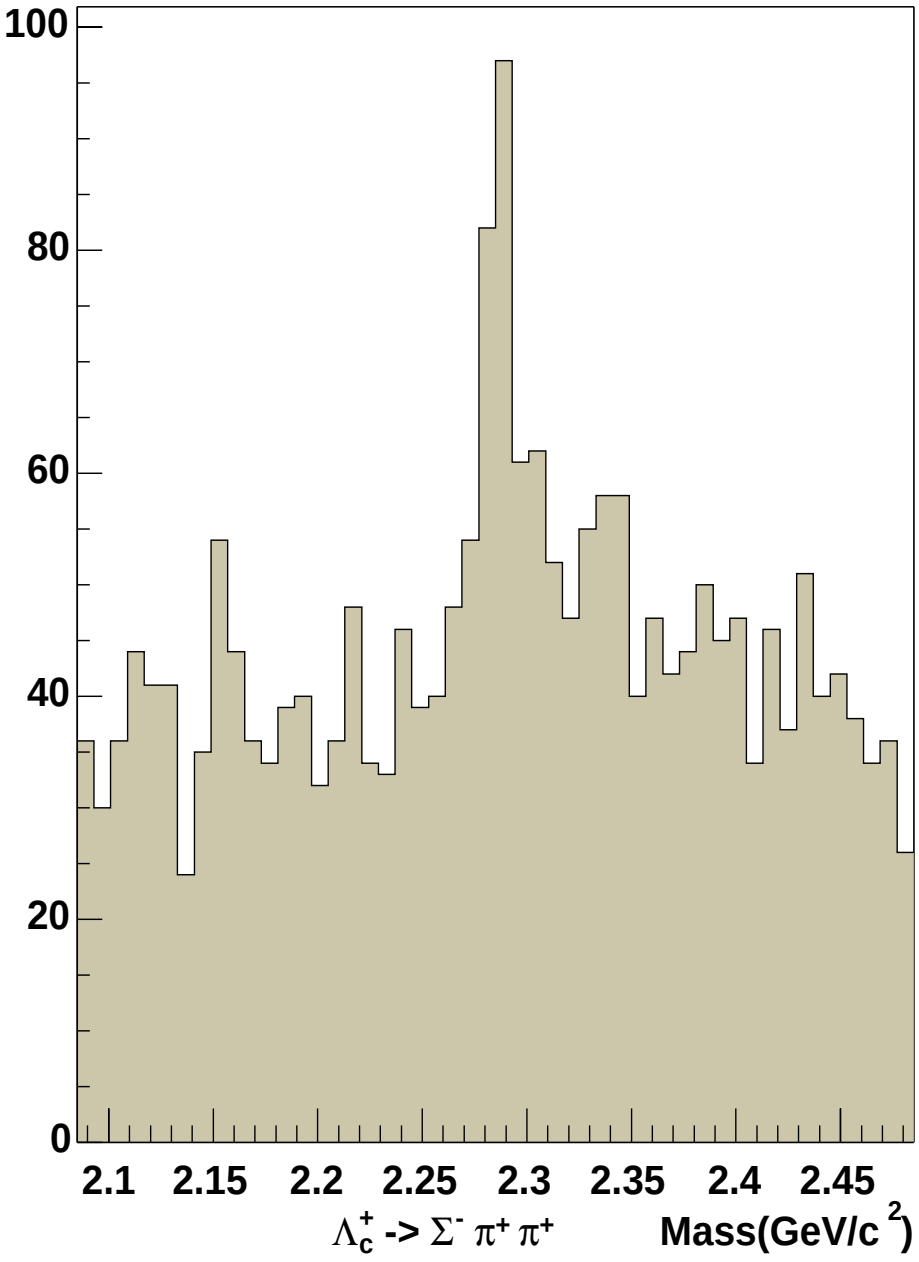

Figure 5.2: $\Lambda_c^+ -> \Sigma^-\pi^+\pi^+$ data in Pass2 after the $\Xi_c^+ -> \Xi^-\pi^+\pi^+$ cuts.

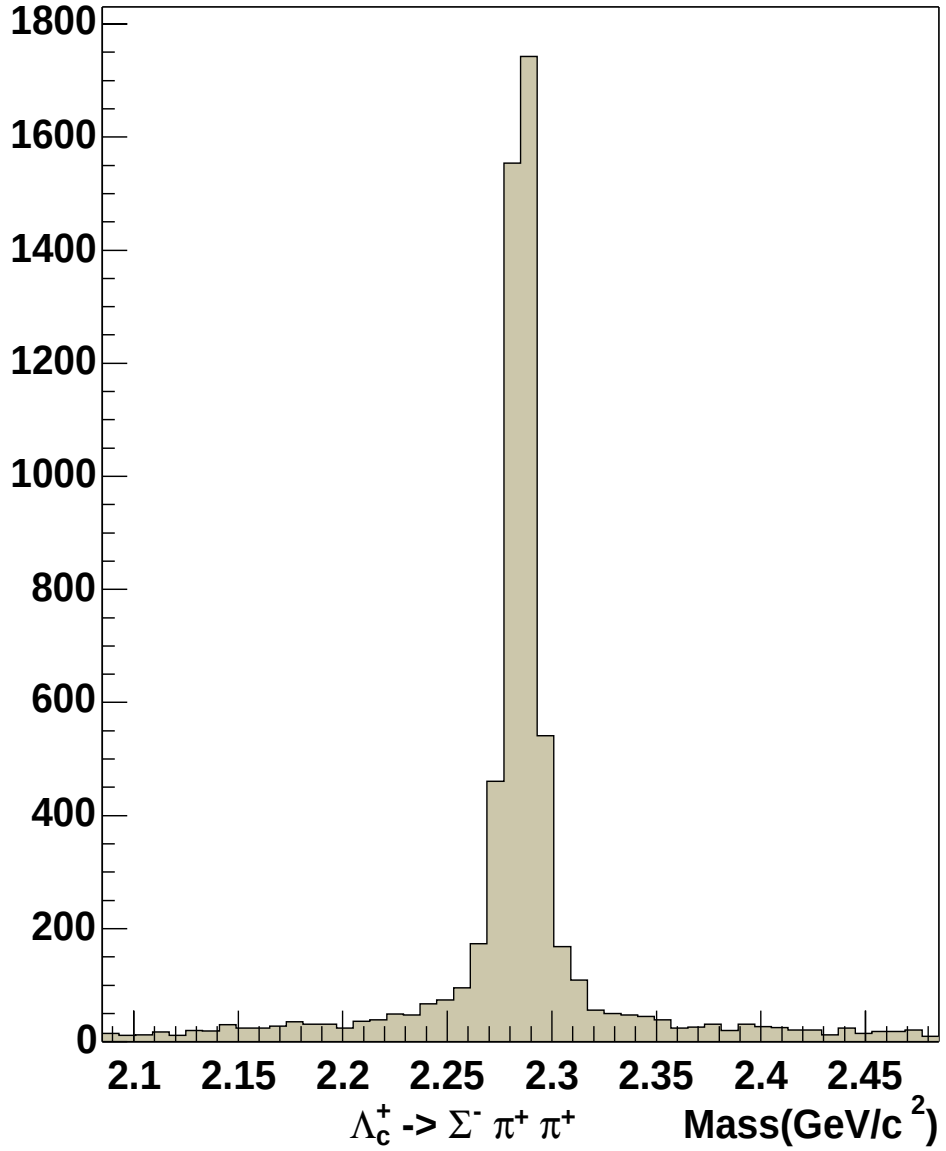

Figure 5.3: $\Lambda_c^+ - > \Sigma^-\pi^+\pi^+$, 500,000 embedded MC events after the $\Xi_c^+ - > \Xi^-\pi^+\pi^+$ cuts.

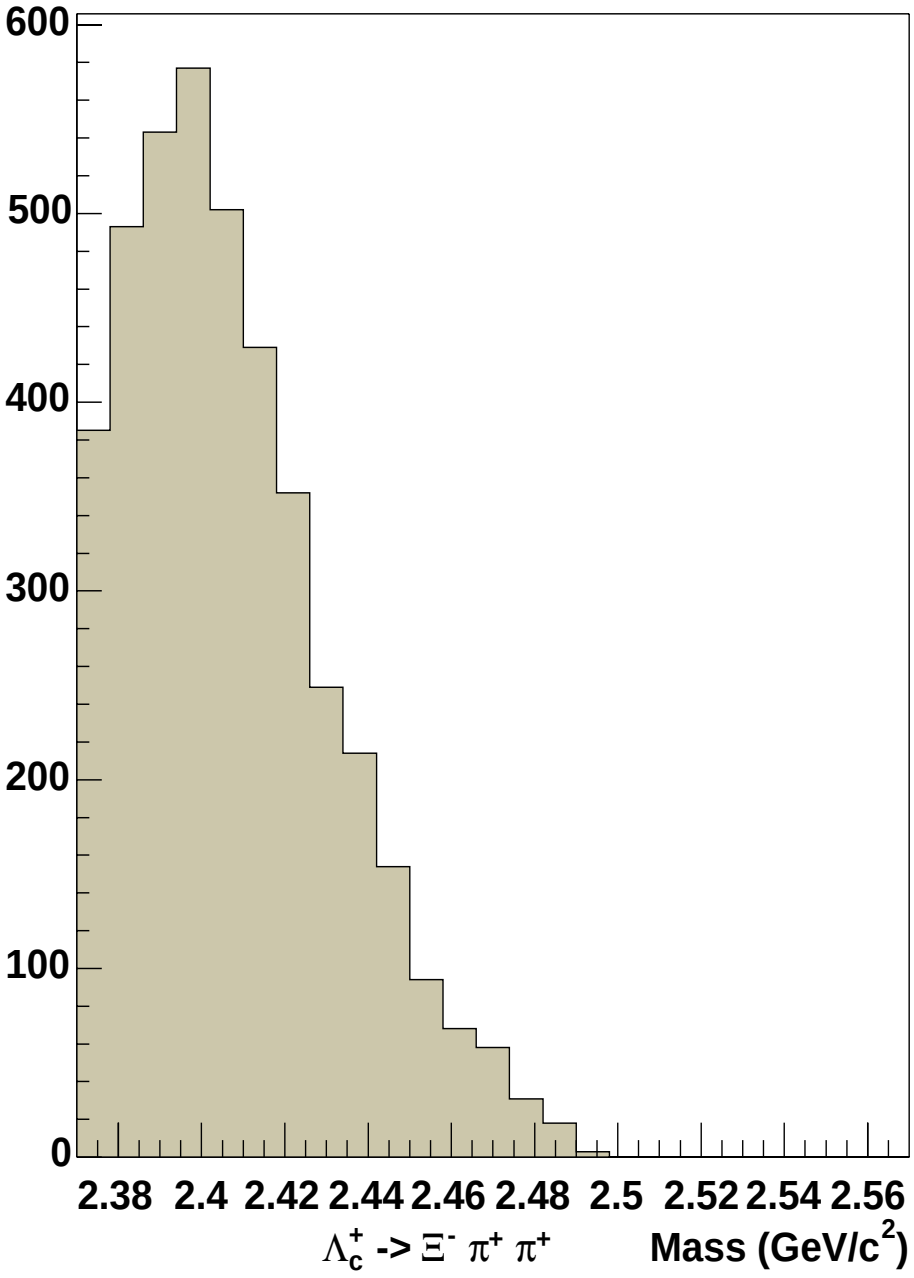

Figure 5.4: $\Lambda_c^+ -> \Sigma^-\pi^+\pi^+$ MC events, invariant mass distribution after switching Σ^- mass with Ξ^- mass.

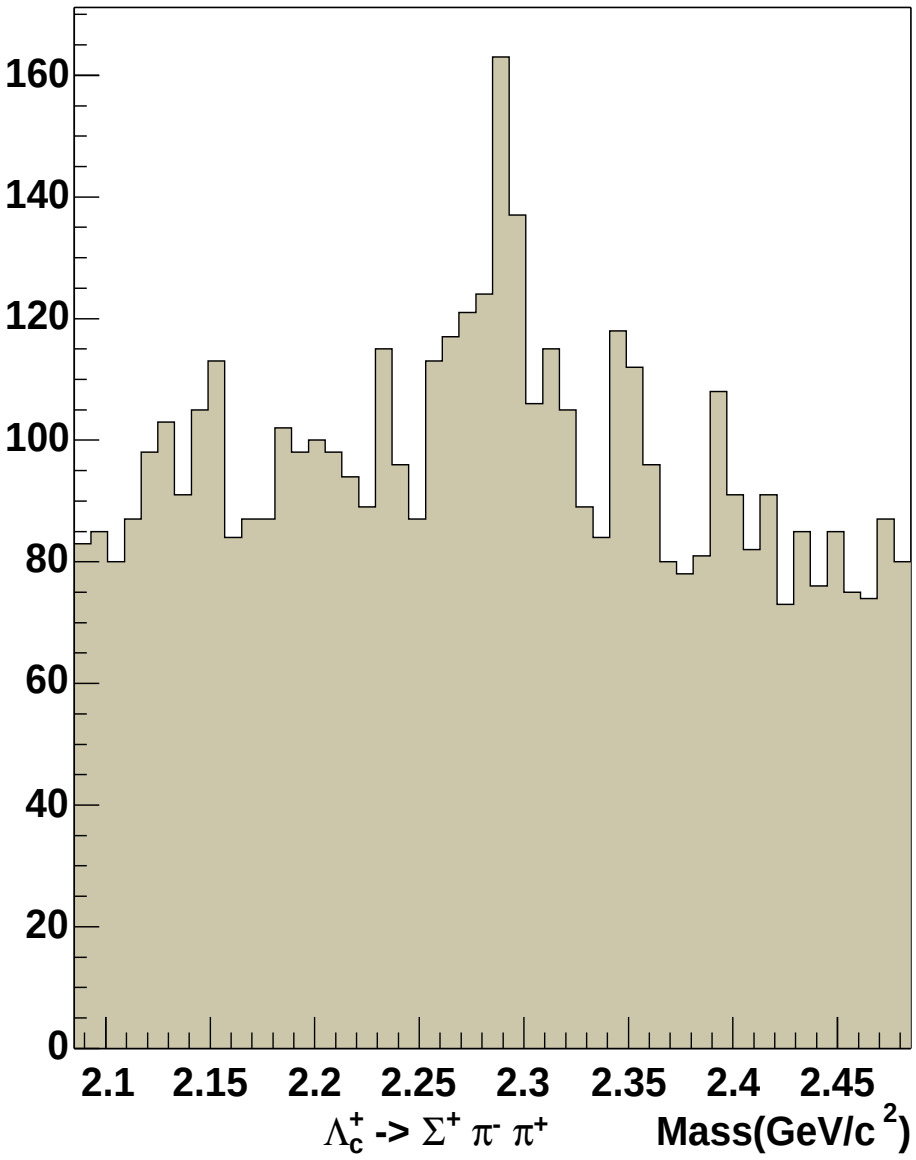

Figure 5.5: $\Lambda_c^+ -> \Sigma^+\pi^-\pi^+$ data in Pass2 after the $\Xi_c^+ -> \Sigma^+K^-\pi^+$ cuts.

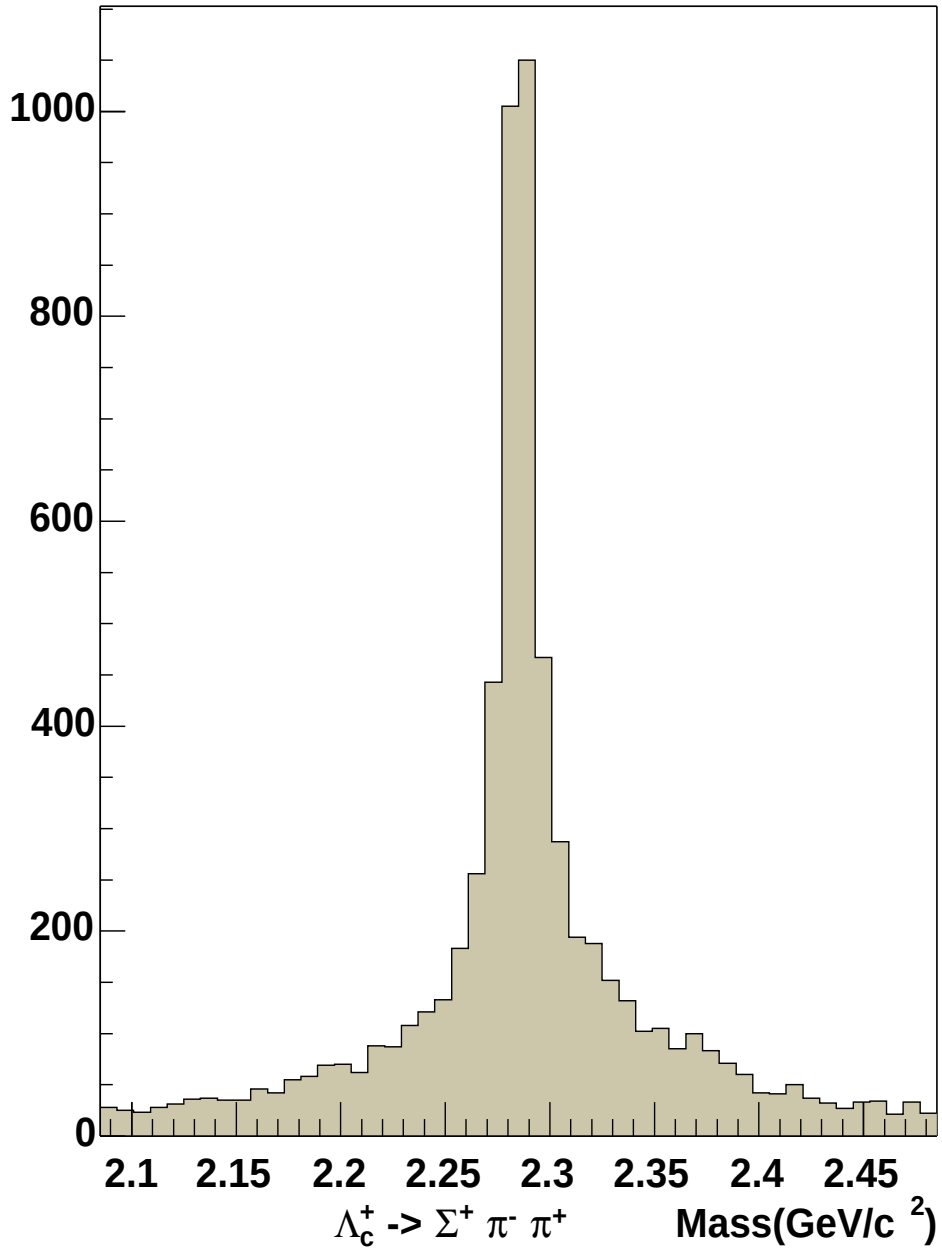

Figure 5.6: $\Lambda_c^+ - > \Sigma^+\pi^-\pi^+$, 500,000 embedded MC events after the $\Xi_c^+ - > \Sigma^-K^-\pi^+$ cuts.

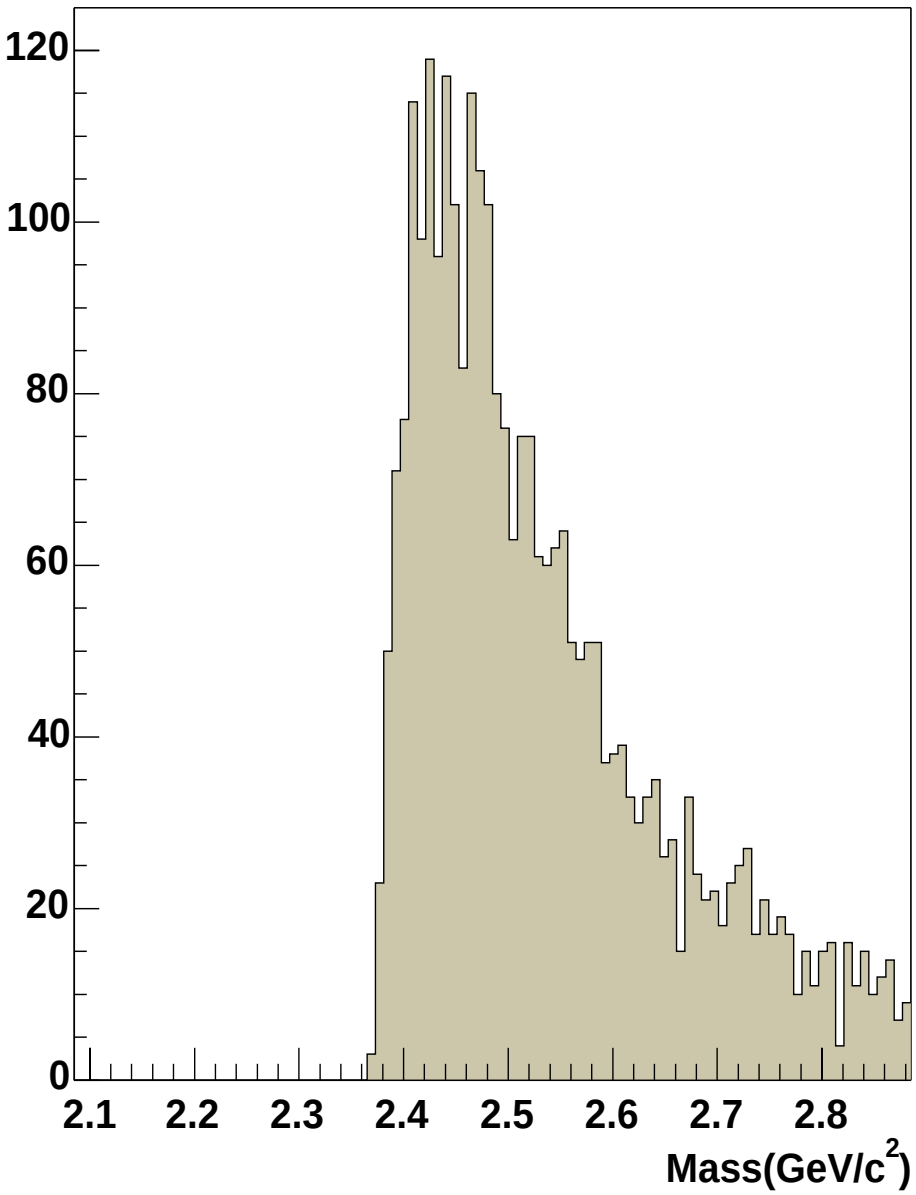

Figure 5.7: $\Lambda_c^+ -> \Sigma^-\pi^+\pi^+$ MC events, invariant mass distribution after switching π^- mass with K^- mass.

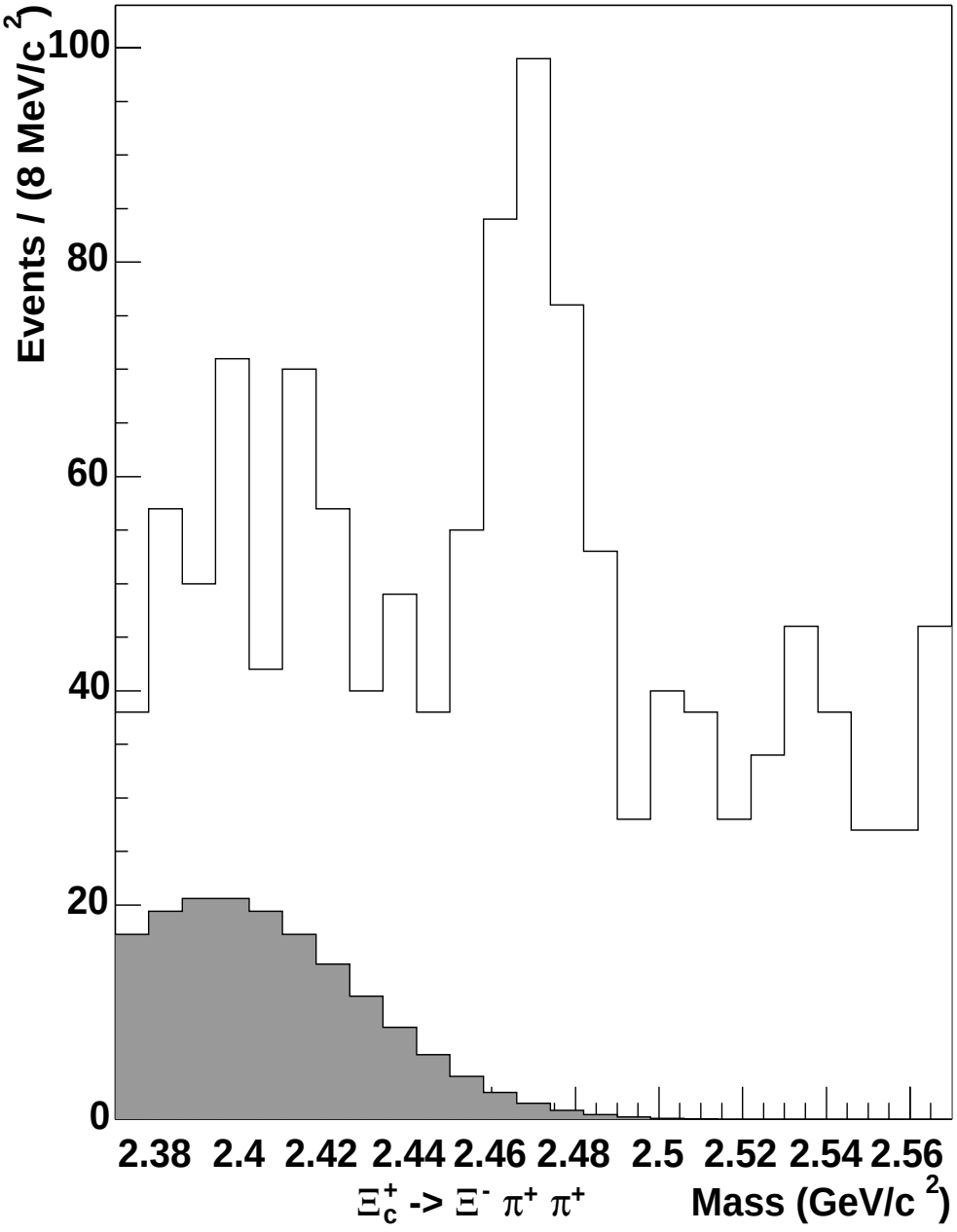

Figure 5.8: $\Xi_c^+ -> \Xi^-\pi^+\pi^+$ mass signal with reflection.

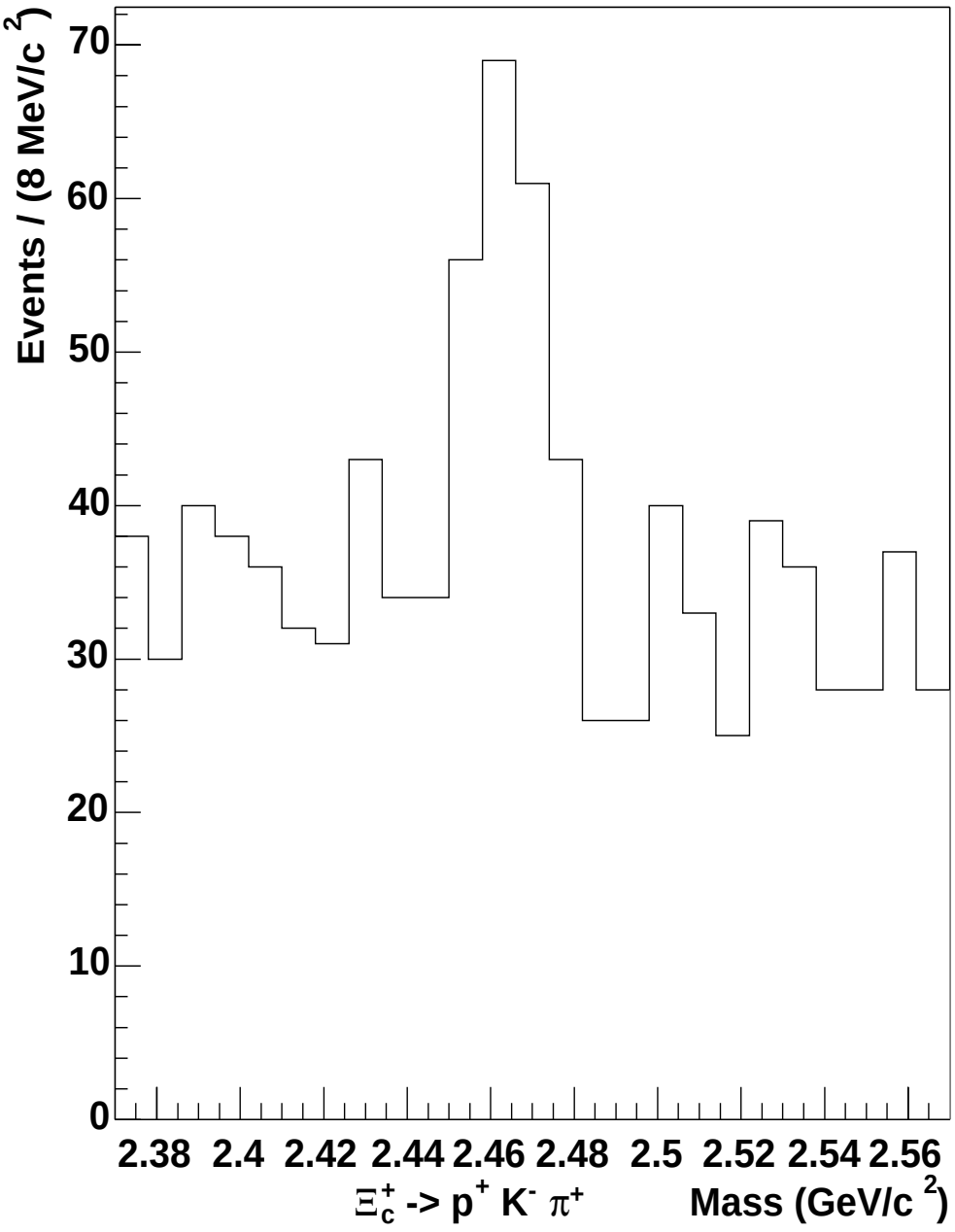

Figure 5.9: $\Xi_c^+ -> p^+K^-\pi^+$ mass signal.

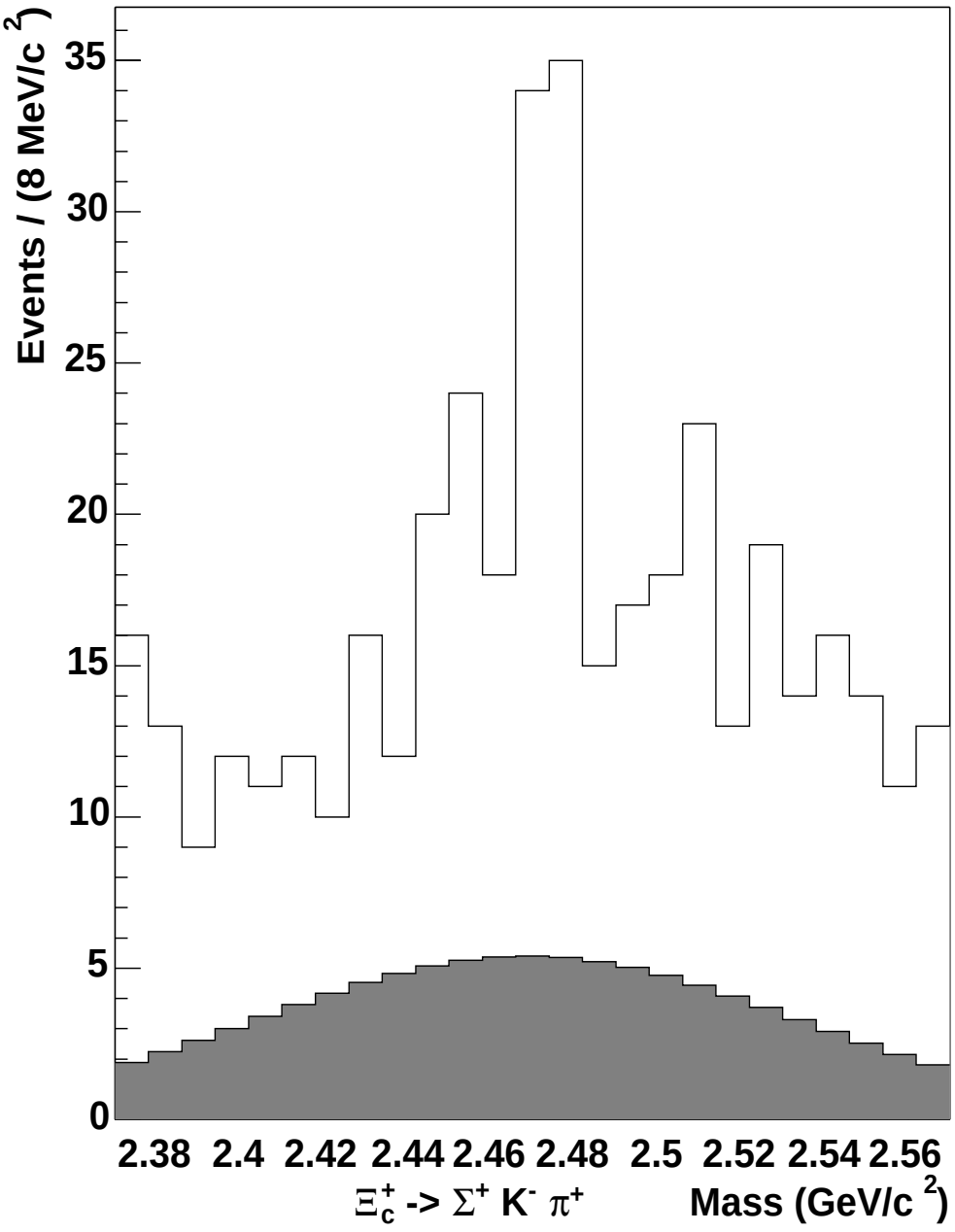

Figure 5.10: $\Xi_c^+ -> \Sigma^+ K^- \pi^+$ mass with reflection.

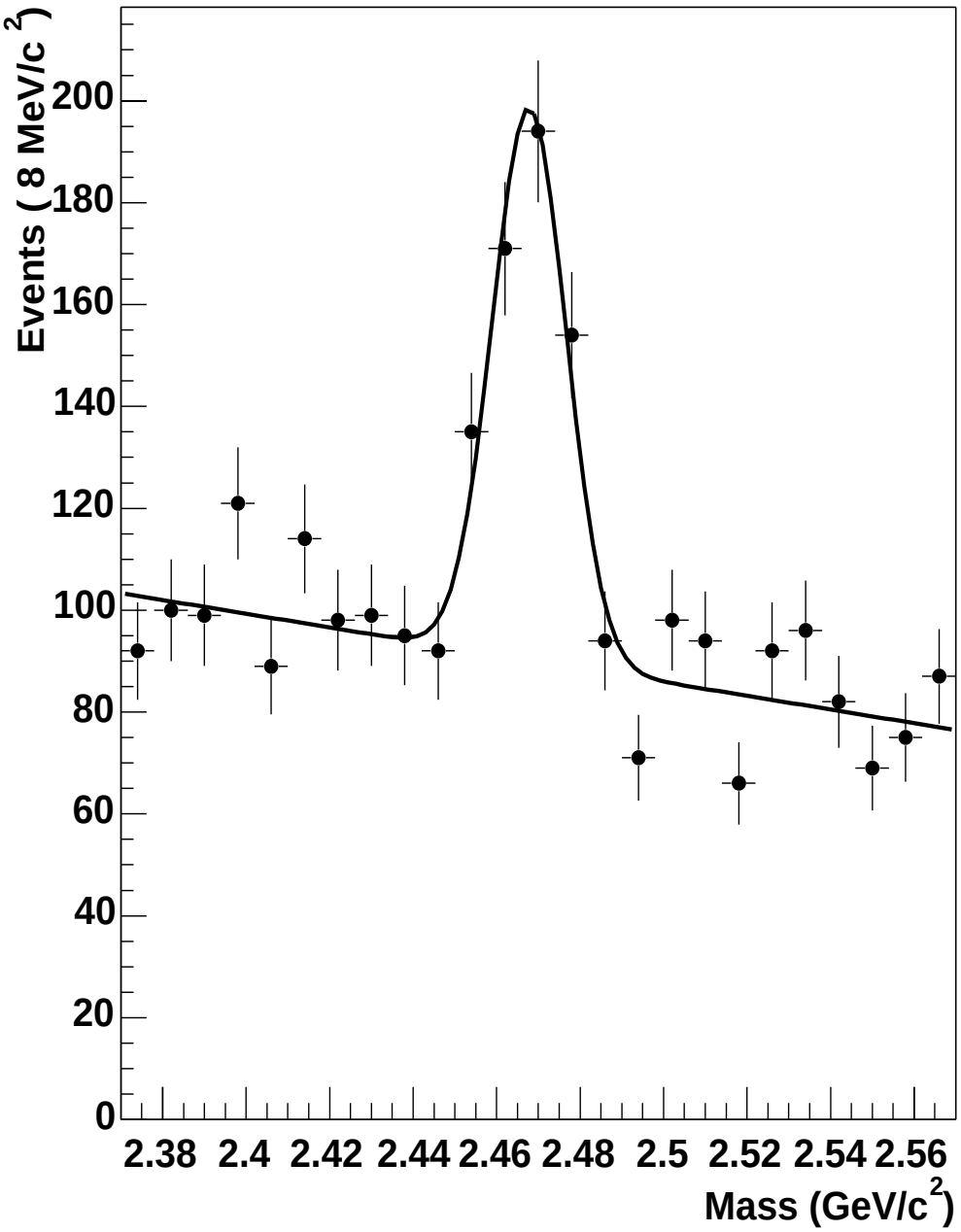

Figure 5.11: Total Ξ_c^+ events, mass distribution.

A fit to the total Ξ_c^+ mass distribution using one Gaussian for signal and a linear function for background yields 301 ± 31 reconstructed Ξ_c^+ and a Gaussian σ of 8.8 MeV/c^2, see Fig. 5.11.

5.4 Analysis Technique

The average longitudinal error, σ_z, on the primary and the secondary vertices for $\Xi_c^+ -> \Xi^-\pi^+\pi^+$ sample are $358\mu m$ and $539\mu m$ respectively, which gives combined error of $647\mu m$. In $\Xi_c^+ -> \Xi^-\pi^+\pi^+$ signal region the average momentum is $213GeV/c$, corresponding to a time resolution of 25fs, about 5% of the $\tau_{\Xi_c^+}$.

The Lifetime can be measured in different ways using maximum likelihood method. The basic idea behind this method is to use the known probability density function as the lifetime estimator, in our analysis we used reduced proper time for the sample of events.

$$t' = t - t_{min} = \frac{L - N\sigma_L}{\beta\gamma c} \tag{5.4}$$

where N is the significance of the detachment cut which has been adopted.

There are two different techniques for fitting; continuous and binned maximum likelihood methods. Since the bin-smearing effects are small we used binned maximum likelihood fitting technique to determine the Ξ_c^+ lifetime. So as to exclude the statistical fluctuations in reduced proper time of the background events we parameterized the background lifetime.

A correction function, f(t'), is applied to all data to take into account the factors dependent on the detector resolution and systematic effects. The Correction Function is obtained from bin by bin ratio of reduced proper time of the Monte Carlo samples' (see Figures 5.12 5.13 5.14) distributions before and after the reconstruction code. The ratio of two distributions is fitted to a polynomial function and the value of this function at the center of every bin is accepted as the correction function for

that reduced proper time bin.

We divided the data in lifetime bins and constructed the likelihood function using the probability of observing s_i signal events in a bin i centered around t'_i, when P_i events are predicted, in the presence of background events.

The probability density was performed by the function;

$$P(t', \tau_{\Xi_c^+}, \tau_{Bckg}, \tau_{\Lambda_c^+}, \alpha, \beta) = (1-\alpha-\beta)N_s \frac{e^{-t'/\tau_{\Xi_c^+}}}{\tau_{\Xi_c^+}} f(t') + \beta N_s \frac{e^{-t'/\tau_{Bckg}}}{\tau_{Bckg}} + \alpha N_s \frac{e^{-t'/\tau_{\Lambda_c^+}}}{\tau_{\Lambda_c^+}} \tag{5.5}$$

Where N_s is the total number of events having a mass $\pm 20 MeV/c^2$ around the mean mass. $\tau_{\Xi_c^+}, \tau_{Bckg}, \tau_{\Lambda_c^+}$ are the lifetimes of Ξ_c^+, background, and the reflection,Λ_c^+, events in this region, respectively. The lifetime of Λ_c^+ used in the fit is 200fs. f(t') is the corresponding correction function, every decay channel has its own correction function (see Fig 5.15, Fig 5.16, Fig 5.17). β and α are the ratios of background events and reflection events respectively.

The behavior of the background events in the signal region is assumed to be the same with the sideband region events. For $\Xi_c^+ -> \Xi^-\pi^+\pi^+$ decay channel, since the reflection events are localized on left side of the mass peak (see Fig 5.8), we chose the sideband region from $2.53 GeV/c^2$ to $2.57 GeV/c^2$, away from the effects of the possible reflection events. In the signal region we have around 12 reflection events. The reduced proper time distributions of the signal region events and the background events yield different lifetimes (see Fig 5.18).

For $\Xi_c^+ -> p^+K^-\pi^+$ decay channel, since there is no possible reflection we were able to take two symmetric sideband regions on both sides of the mass peak. The events that with the mass from $2.404 GeV/c^2$ to $2.424 GeV/c^2$ and from $2.504 GeV/c^2$ to $2.524 GeV/c^2$ are taken as sideband events. The reduced proper time distributions of the signal and the sideband regions are given in Fig 5.19.

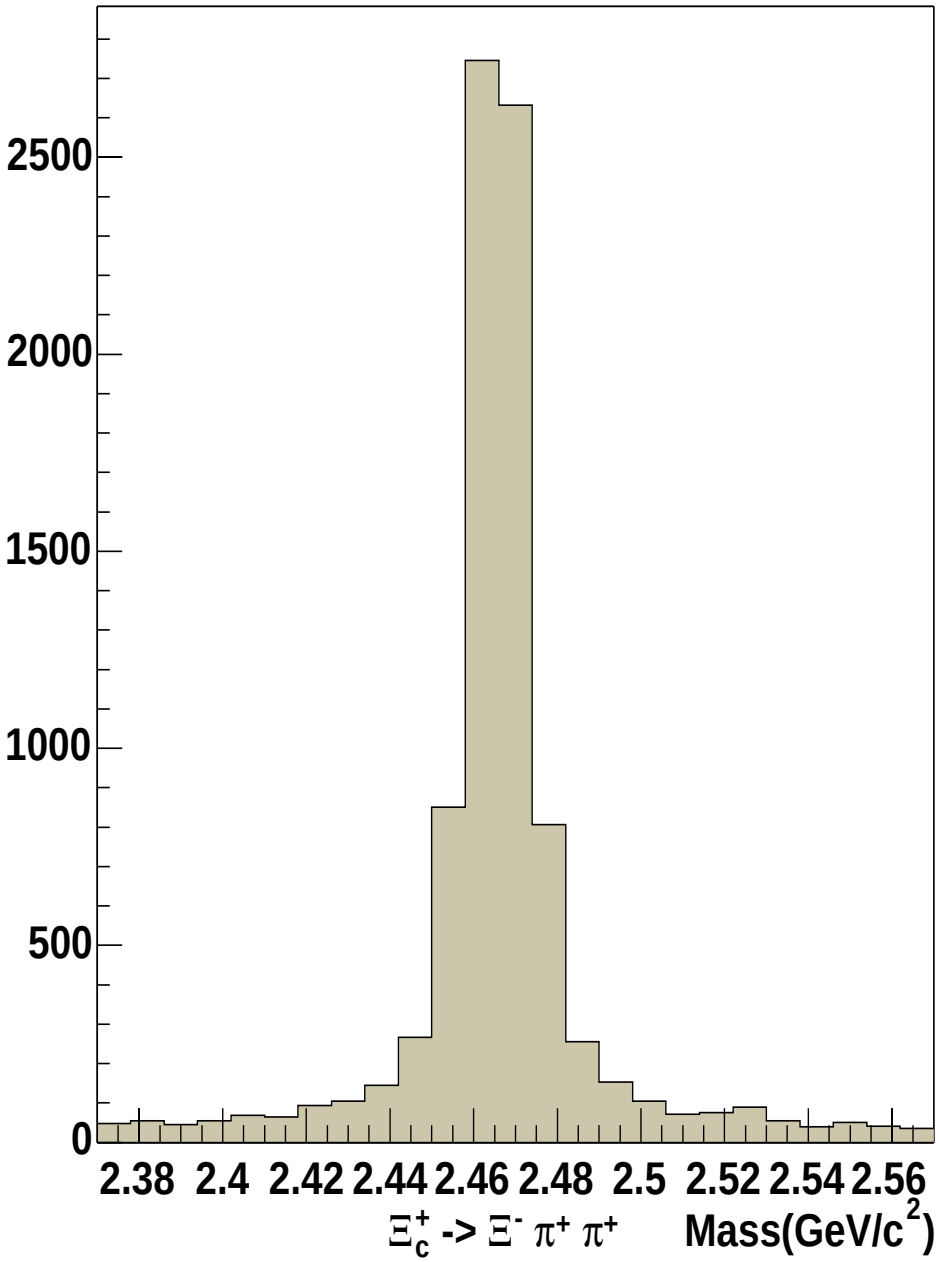

Figure 5.12: $\Xi_c^+ -> \Xi^-\pi^+\pi^+$ Monte Carlo sample after the cuts.

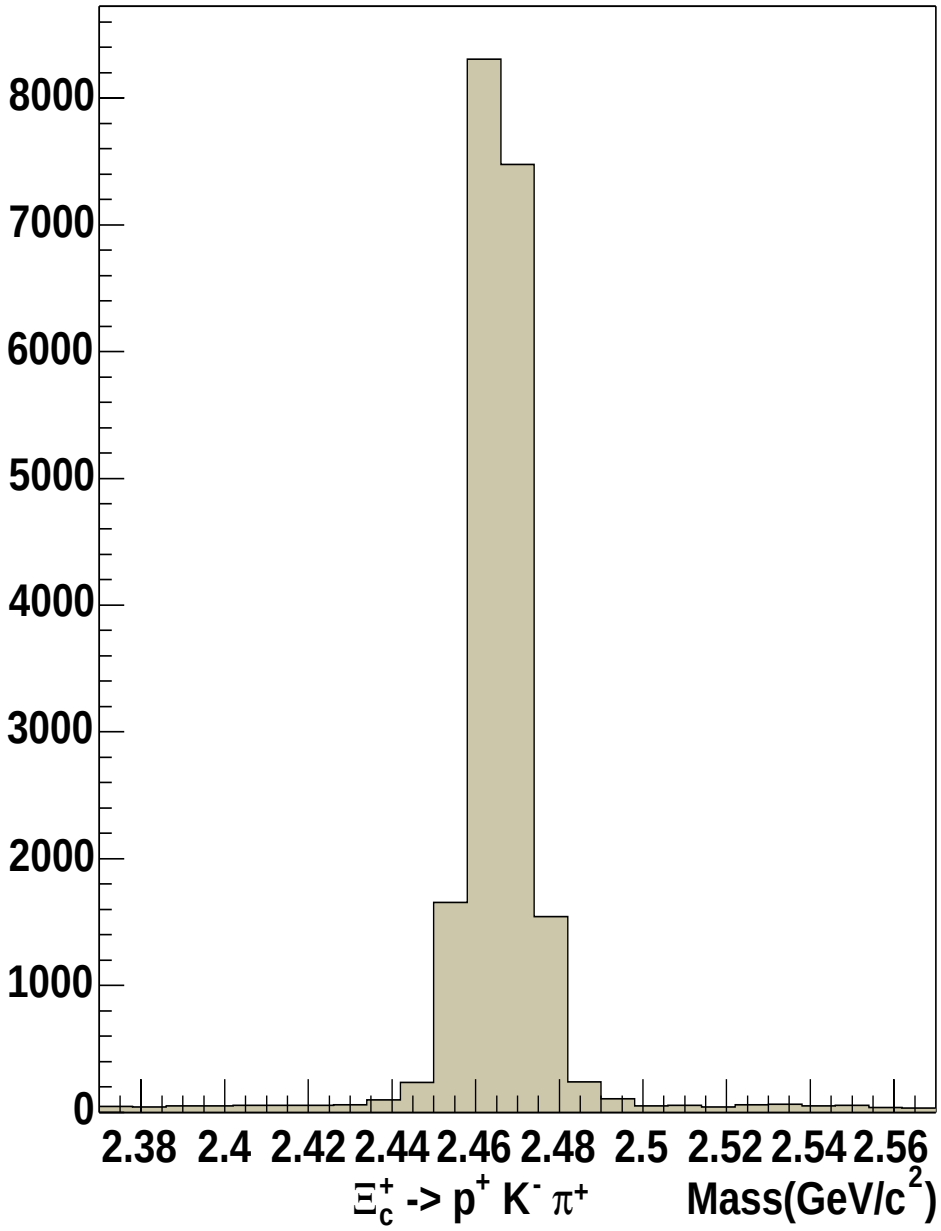

Figure 5.13: $\Xi_c^+ -> p^+K^-\pi^+$ Monte Carlo sample after the cuts.

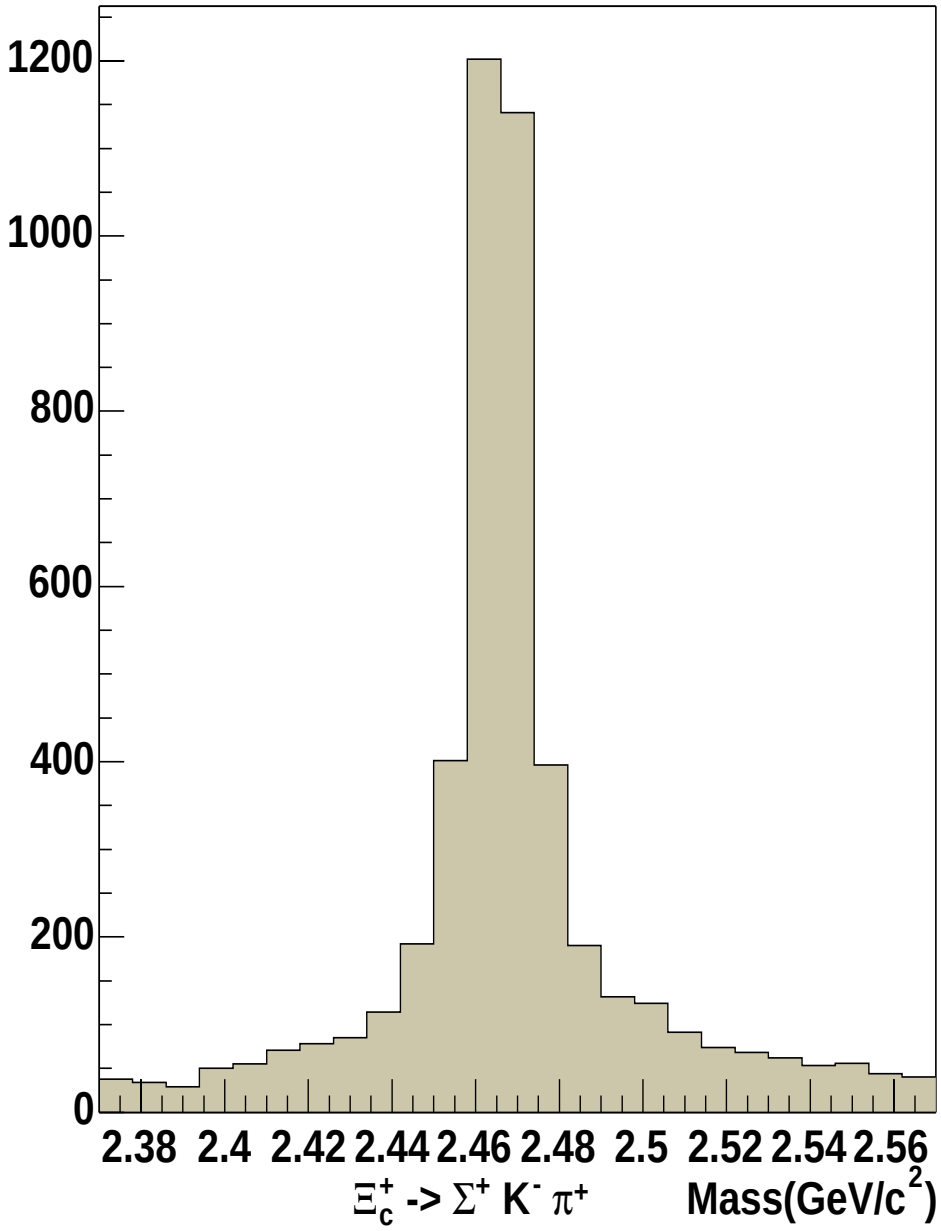

Figure 5.14: $\Xi_c^+ -> \Sigma^+ K^- \pi^+$ Monte Carlo sample after the cuts.

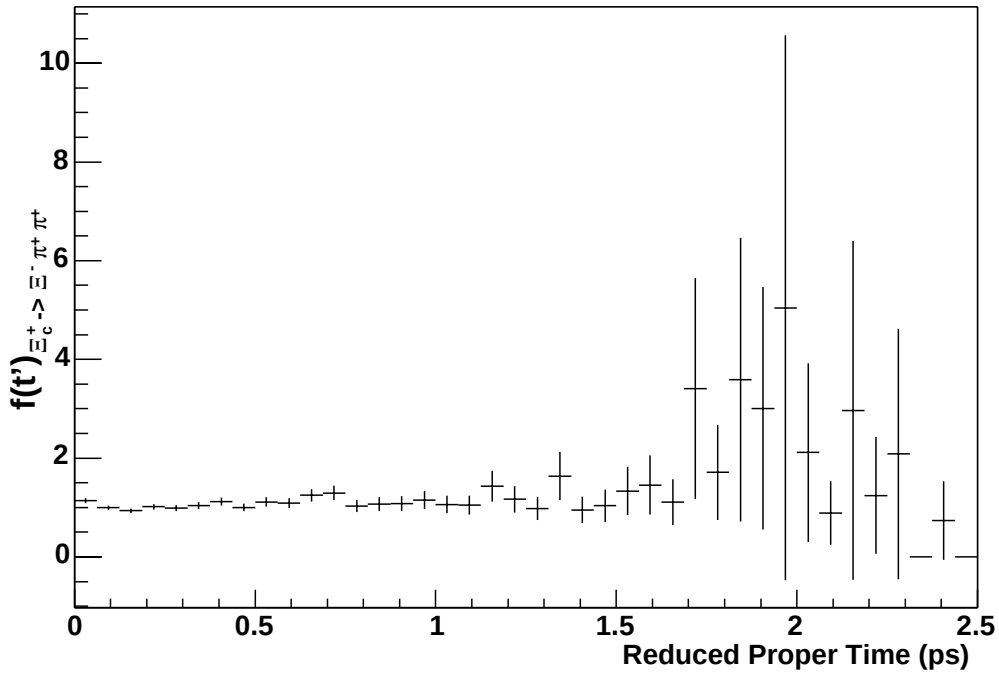

Figure 5.15: $\Xi_c^+ -> \Xi^-\pi^+\pi^+$ Correction Function.

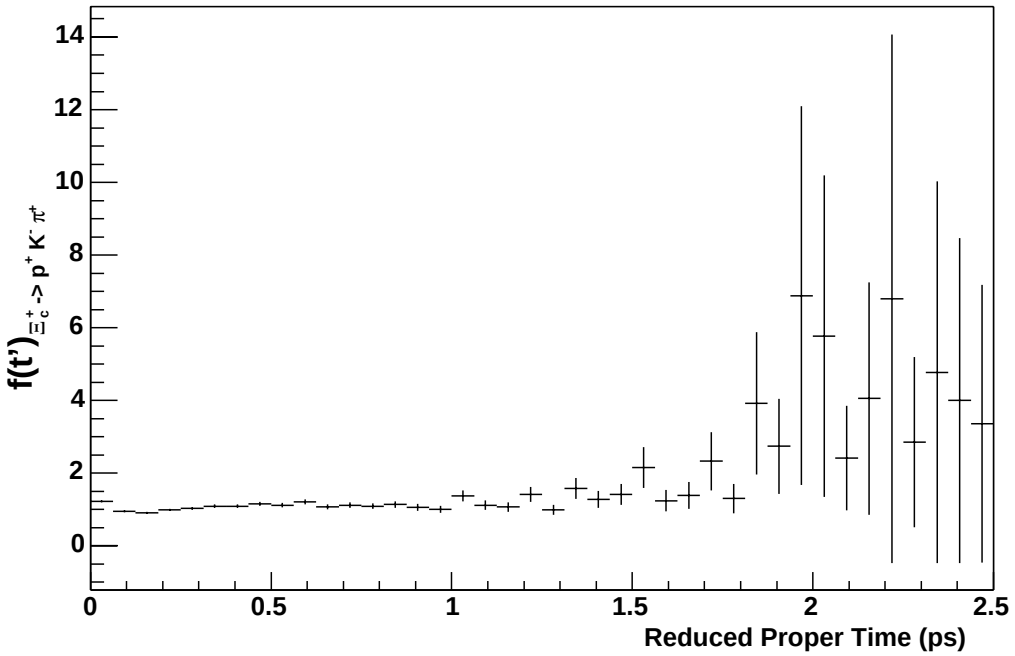

Figure 5.16: $\Xi_c^+ -> p^+K^-\pi^+$ Correction Function.

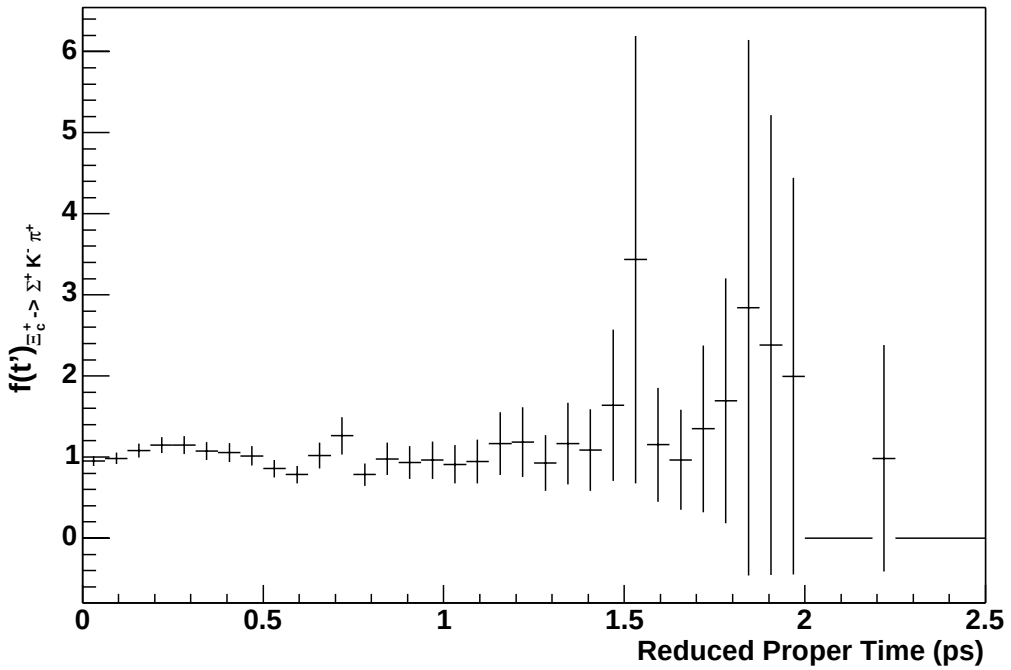

Figure 5.17: $\Xi_c^+ -> \Sigma^+ K^- \pi^+$ Correction Function.

For $\Xi_c^+ -> \Sigma^+ K^- \pi^+$ decay channel the situation is a little bit more complicated. The reflection is distributed all over the mass region, so we cannot find a sideband region that is not contaminated by possible reflection (see Fig 5.10). The events that have mass from $2.414 GeV/c^2$ to $2.434 GeV/c^2$ and from $2.514 GeV/c^2$ to $2.534 GeV/c^2$ are chosen as sideband events. The reduced proper time difference between signal and the sideband events of this channel are given in Fig 5.20. There are 23 possible reflection events in the signal region (see Fig 5.10).

Finally, the Maximum Likelihood Function is the Landau probability of finding s_i events in i^{th} reduced proper time bin while we are expecting P_i events for all of the bins.

$$L = \Pi_{i=1}^{i=40} \frac{P_i^{s_i} e^{P_i}}{s_i!} \tag{5.6}$$

Where P_i and s_i are expected and existing number of events in i^{th} bin. Since

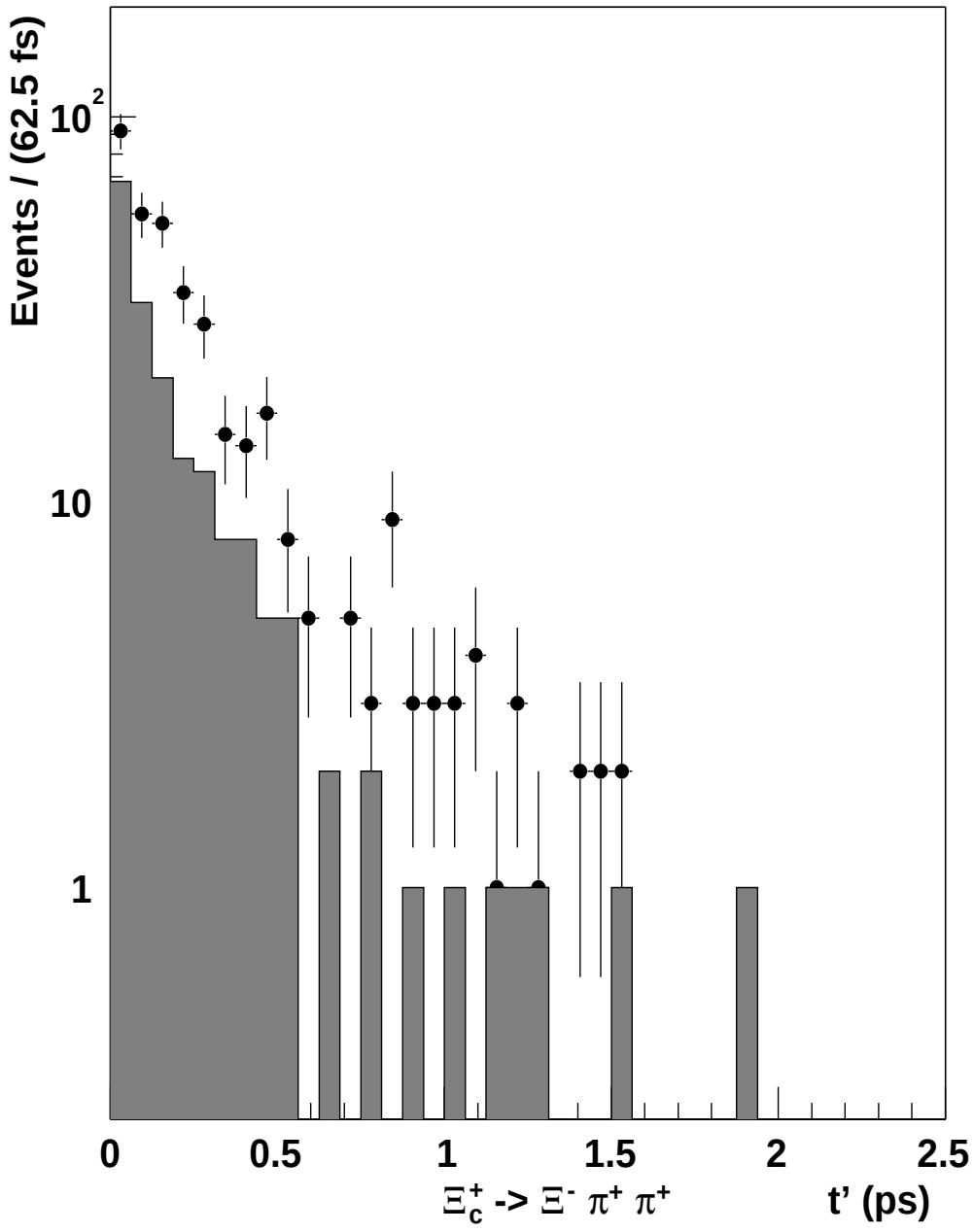

Figure 5.18: ID520 signal and sideband reduced proper time distributions.

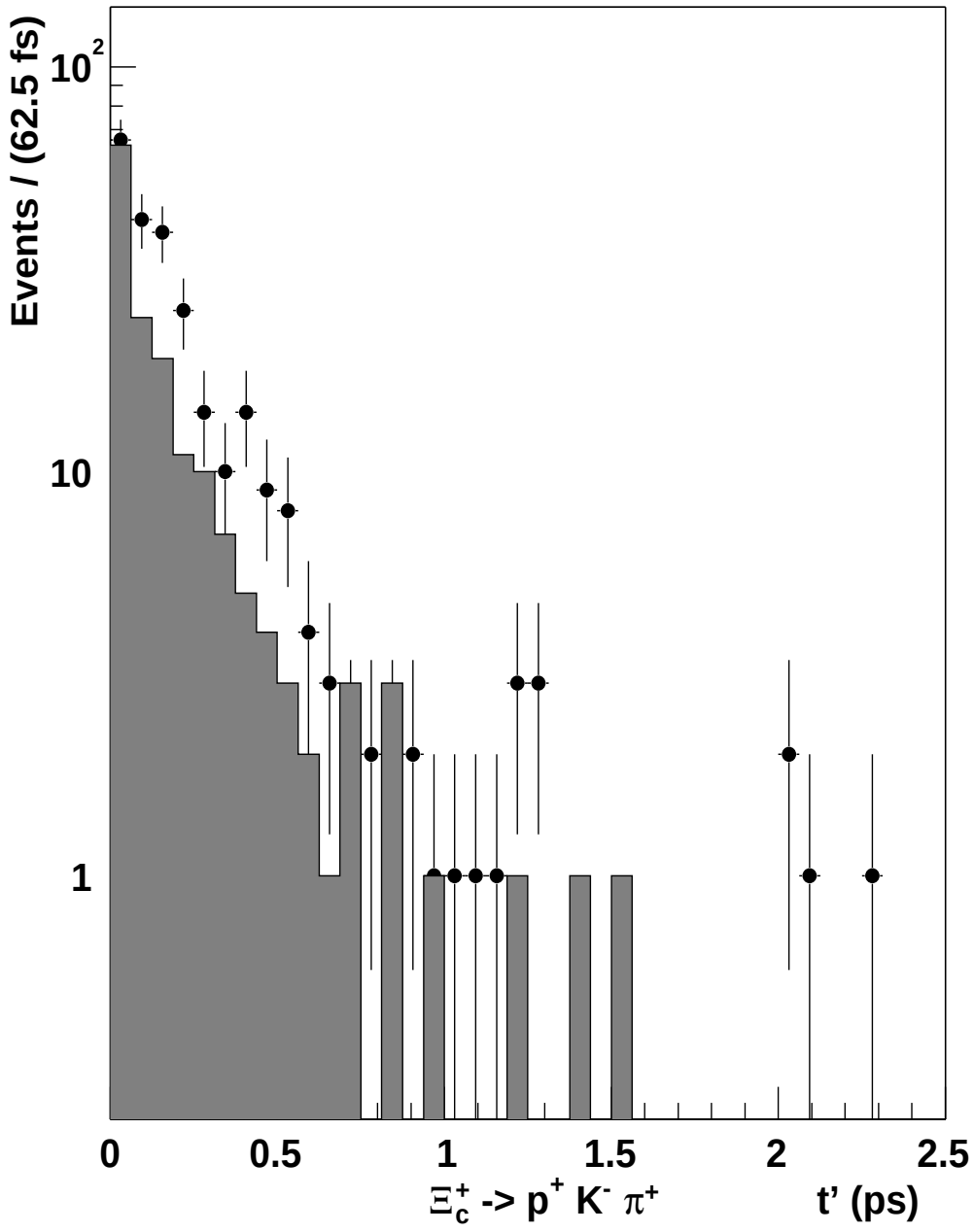

Figure 5.19: ID400 signal and sideband reduced proper time distributions.

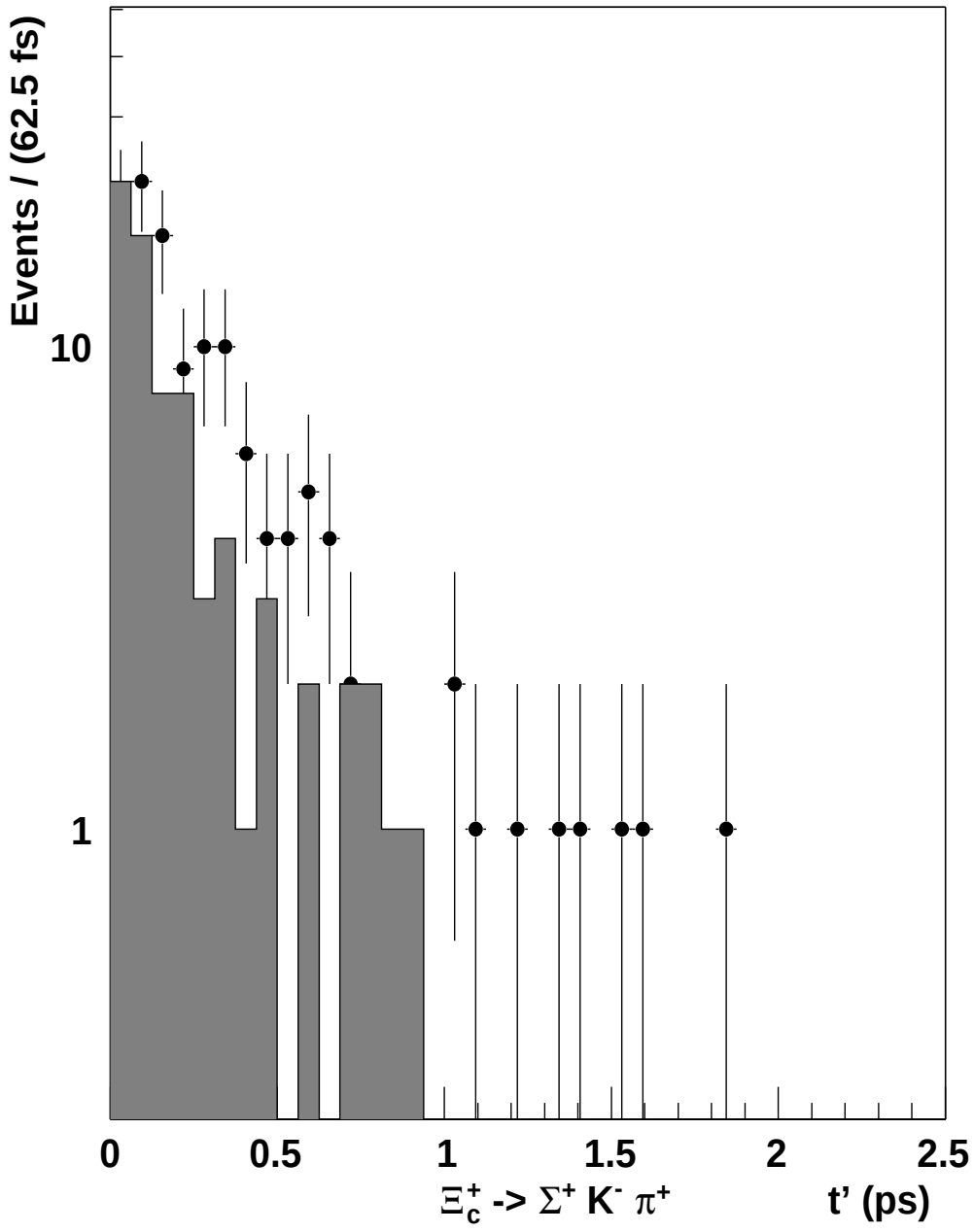

Figure 5.20: ID522 signal and sideband reduced proper time distributions.

we have three independent data set, we analyzed them separately and took the weighted average, the total lifetime for Ξ_c^+ is found to be 427 ± 31 fs 5.3.

Ξ_c^+ Decay Channel	Event Number	Lifetime (fs)
$\Xi^-\pi^+\pi^+$	157 ± 21	400 ± 45
$\Sigma^+K^-\pi^+$	46 ± 11	430 ± 63
$p^+K^-\pi^+$	98 ± 17	470 ± 60
Total	301 ± 31	427 ± 31

Table 5.3: Analysis results for different decay channels.

5.5 Systematic Errors

We have made the systematic study by using Monte Carlo simulations and 157 ± 21 $\Xi_c^+ -> \Xi^-\pi^+\pi^+$ decays. This lifetime analysis is based on the assumption that the background behavior under the signal peak is the same with the events in the mass sidebands. This fundamental assumption can be verified by calculating the lifetime with different sideband regions. We calculated the lifetime with 9 different sideband regions, the RMS of these measurements, 12.5fs, was used to understand the variations of lifetime, (see Fig 5.21). This variation is the combination of statistical fluctuations and the systematical errors.

$$\sigma_{obs} = \sqrt{\sigma^2_{expected} + \sigma^2_{syst}} \tag{5.7}$$

So as to understand the statistical background variations we used simulated events. The expected statistical fluctuation on background yields 12.5 fs, (see Fig 5.22). This shows that we don't have any systematic error coming from our choice of sideband.

In this lifetime analysis we have a resolution of 25fs, and the bin size for reduced proper time distribution we have chosen 62.5 fs, 2.5 times the resolution. Different bin sizes can change the outcome of the analysis. The systematic uncertainty due to reduced proper time bin size has been studied for 7 different bin sizes; 25fs, 50fs, 60fs, 62.5fs, 65fs, 70fs, 75fs. The systematic error due to bin size is 6.9 fs, (see Fig 5.23).

The X_f distribution for our data gives 3.6 ± 0.7 as X_f power. We created MC samples with different X_f powers and measured lifetime with the correction functions coming from these samples. The systematic errors coming from this study is 11fs.

The Correction function is determined by the bin by bin ratio between the reduced proper time distributions of sideband subtracted Monte Carlo sample and the proper time function of created perfect events before the embedding. This ratio is fitted to a function so the correction function varies smoothly along the reduced proper time range. This fit procedure yields 3fs systematical errors to our measurement.

Other than these we studied different t_{max} values for reduced proper time distributions. The contribution of the change in the range of the reduced proper time to the systematic is found to be 1fs.

Adding these contributions in quadrature gives a total systematic uncertainty of 13 fs.

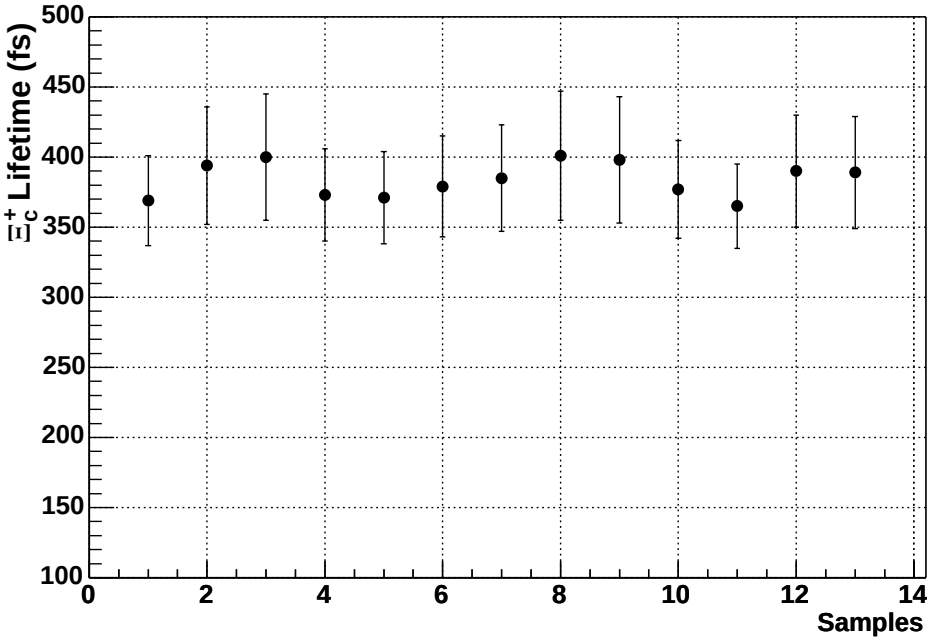

Figure 5.21: Lifetime variations on data for different sideband regions.

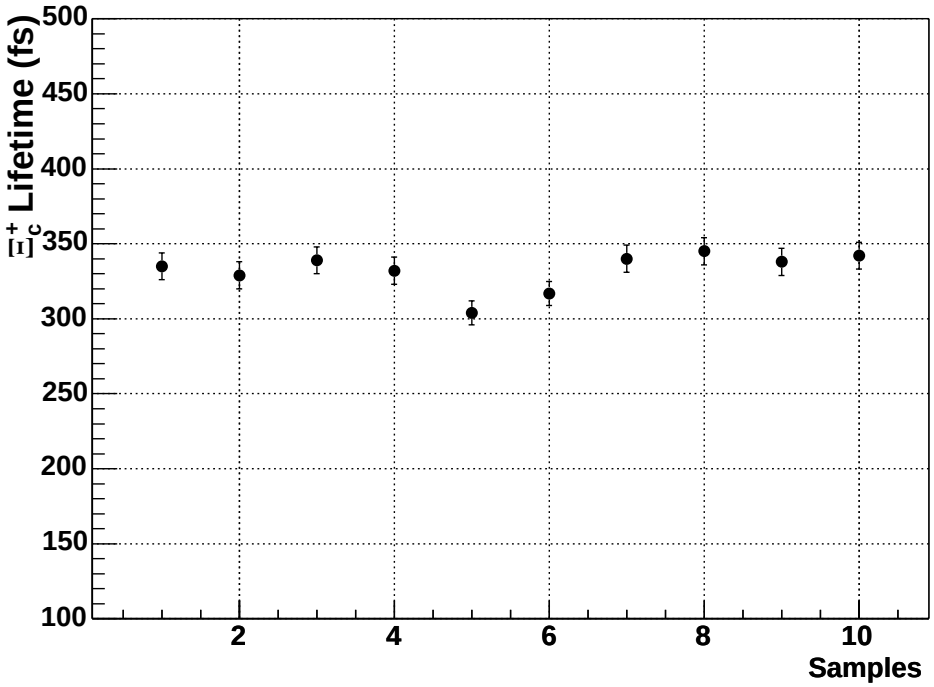

Figure 5.22: Statistical fluctuations on lifetime due to sideband for simulated events.

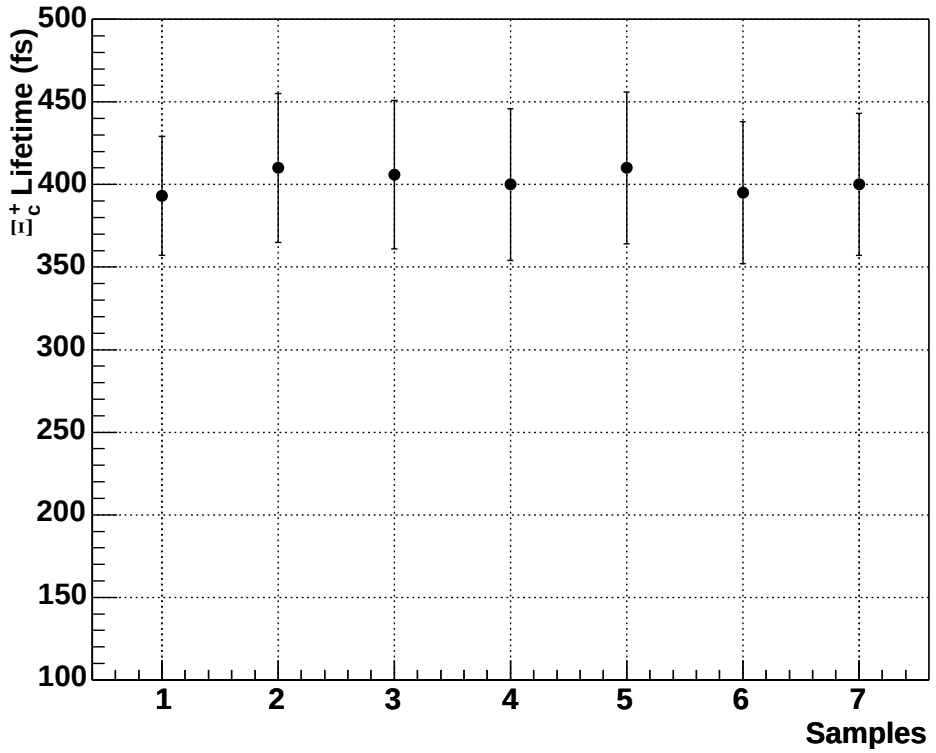

Figure 5.23: The variations on lifetime for different bin size of reduced proper time distribution.

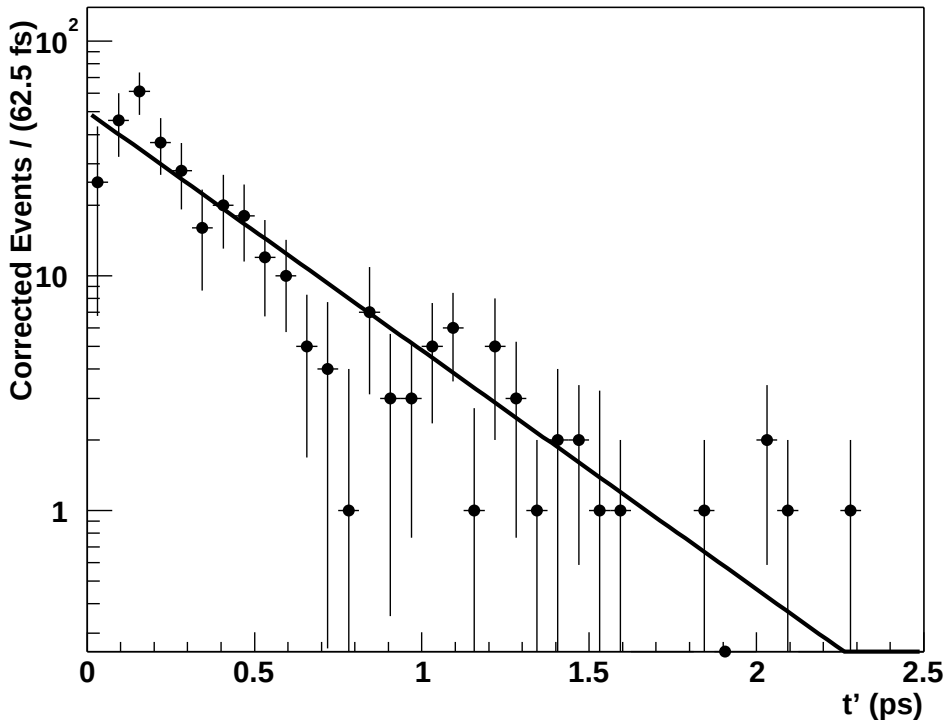

Figure 5.24: The combined lifetime fit of the Ξ_c^+ decays with a sideband subtracted, Monte Carlo corrected, reduced proper time distribution. Solid line gives $427 \pm 31 \pm 13$ fs.

CHAPTER 6
CONCLUSION

The PMT evaluation process consists of some tests which are necessary to compare the sample PMTs from three different manufacturers. The tests were designed to determine whether the sample PMTs suggested by the manufacturers satisfy the operational requirements listed in Table 2.1. (Initial requirements, which are basically physical characteristics, listed in that table are already satisfied by the tubes suggested.) The quantities measured in these tests were transit time, pulse width, rise time, transit time spread, dark current, gain, linearity, and single photoelectron resolution. PMTs from all three manufacturers either performed within the required limits or better in most of these tests. Spatial uniformity of the photocathode surface was not a selective quantity.

However, the single photoelectron resolution measurement showed a clear difference in the performance of the sample tubes. Hamamatsu R7525HA and Electron Tubes D844WSB PMTs produced single photoelectron spectra with parameters within the required limits. On the other hand, Photonis XP3182 PMTs did not produce a single photoelectron spectrum in the same setup.

Even though Electron Tubes and Hamamatsu PMTs were somewhat comparable in general, in terms of overall performance Hamamatsu PMTs performed much closer to the HF Forward Calorimeter specifications. Lower cost was also an additional point in favor of Hamamatsu PMTs.

The complete tests we performed on the 2300 R7525HA PMT delivered by Hamamatsu consist of two groups; the tests we performed on every PMT, and the tests we performed on some portion of the sample. Transit time, pulse width, rise time, transit time spread, dark current, relative gain, single pulse linearity, tests were done to all 2300 PMTs. And the results were used to reject the PMTs which

do not meet to the CMS HF specifications. We rejected total 20 PMTs due to high dark current.

The sampling tests were single photoelectron resolution, gain versus high voltage, double pulse linearity, relative quantum efficiency, photocathode uniformity and lifetime test. Overall the randomly chosen PMTs performed pretty well on these tests. For the design and construction of the HF calorimeter the gain and lifetime of the PMTs are very important. The tests show that PMTs will survive 10 years of operation, up to 3000 C of charge accumulation if they run with mid level gain value.

In the second part of the thesis we report charm baryon lifetime analysis done with SELEX pass2 data sample. We have measured the lifetime of Ξ_c^+ using three different decay modes with 301 ± 31 events. This is the second biggest Ξ_c^+ sample among the current charm baryon experiments (see Table 6.1). Due to the high background which is a characteristic of SELEX we used binned maximum likelihood method and found the lifetime to be $427 \pm 31 \pm 13$ fs, where the first error is statistical and the second is systematic. This measured value is in agreement with theoretical predictions. The Monte Carlo corrected, background subtracted, total reduced proper time distribution is shown in Fig 5.24.

Experiment	Year	Event Number	Lifetime (fs)
SELEX	2003	301	$427 \pm 31 \pm 13$
FOCUS	2001	532	$427 \pm 31 \pm 13$
CLEO	2001	250	$503 \pm 47 \pm 18$
E687	1998	56	$340 \pm 70 \pm 20$
E400	1987	102	$400 \pm 180 \pm 100$

Table 6.1: Ξ_c^+ lifetime measurements from different experiments.

APPENDIX A
THE CUT OPTIMIZATION STUDY ON SELEX PASS2 DATA

A.1 Cut Optimization Study

In this section we give the detailed cut optimization study that we performed on three decay channels of Ξ_c^+ sample. We used these Monte Carlo events for cut optimization study. We scanned all the possible cut values to see where we can maximize the significance.

$$Significance = S_{mc}/\sqrt{S_{data} + B_{data}} \tag{A.1}$$

This process has been done for every decay channel in this analysis, the cut optimization results for $\Xi_c^+ -> \Xi^-\pi^+\pi^+$ are shown in Figures A.1 A.2 A.3 A.4 A.5 A.6 A.7 A.8.

The cut optimization results for the decay channel $\Xi_c^+ -> p^+K^-\pi^+$ are shown in Figures A.9 A.10 A.11 A.12 A.13.

The cut optimization results for the decay channel $\Xi_c^+ -> \Sigma^+K^-\pi^+$ are also given in the Figures A.14 A.15 A.16 A.17.

S_{mc} is the number of signal events on the Monte Carlo events after the cut is applied, S_{data} and B_{data} are the signal and the background events in the signal region of the real data sample, respectively. Signal region is defined to be the $\pm 20 MeV/c^2$ around the mean mass value.

The cuts we used or considered to use are;

(i) L/σ_L : L is the distance between the primary and the secondary vertices (see Fig 5.1). Since the charm baryon angles of deflection are very small, around 10 mrad, $L = z_{sec} - z_{prim}$ is an excellent approximation. The secondary vertex position is defined by the fit of the secondary vertex tracks to the common vertex. The primary vertex position is defined by the fit of the tracks from primary vertex. The definition of σ_L is;

$$\sigma_L = \sqrt{\sigma_{prim}^2 + \sigma_{sec}^2} \tag{A.2}$$

(ii) *Pvtx* : The charm track was reconstructed as the vector sum of its secondary tracks, and this summation vector is extrapolated to the primary vertex, the misdistance with respect to the primary vertex is calculated. The misdistance divided by its error is called Pvtx, point back.

(iii) *Scut* : The secondary vertex tracks are extrapolated back to the z_{prim}. The second largest miss-distance with respect to primary vertex is called s_2, and σ_{s_2} is the extrapolated error, calculated using the track error matrix. Scut is defined to be s_2/σ_{s_2}. This cut suppresses the background events generated by the secondary vertex tracks extrapolated back to the primary vertex.

(iv) ΣP_t^2 : Sum of the squared transverse momentum of the secondary particles with respect to the charm track.

(v) P_{π^+} : The momentum of the π^+ is required to be greater than some value this cut helps to reject the soft pion that cause high background.

(vi) *Smin* : Smin is very similar to the Scut, but Smin gives the spatial distance for the second biggest misdistance in unit of cm. In Pass1 analysis Smin was applied to the Ξ_c^+ sample (see [33]), but in Pass2 sample we found Scut more powerful to reduce the background.

(vii) χ^2 : In the reconstruction package the second vertex reconstruction was attempted when the χ^2 per degree of freedom (χ^2/dof) for the fit of ensemble of the tracks to a single primary vertex exceeds 5. We did not need to apply this cut again in the analysis code, it was already applied as a default value in reconstruction package.

(viii) x_f : When the Feynman x distribution of the particles are required to be higher, we tend to reduce the background by eliminating the soft particles. This cut is powerful to reduce the background but we did not include it in out cut sample

for lifetime analysis.

(ix) *RICHprobability* : For the decay channels that have protons, sigmas and kaons we required the RICH identification probability of these particles to be equal or greater than pion probability.

(vi) Δz_{tgt} : Most of the events in the experiment were not charm, but rather secondary interactions in the targets, where tracks could accidentally form a mass close to a charm mass. Removing events which have a secondary vertex z_{sec} close to one of the targets significantly reduced that background. This cut discriminate against secondary interactions and multiple scattering effects. So, for some of the decay channels we required the secondary vertex z position to be at least $500\mu m$ away from the closest target.

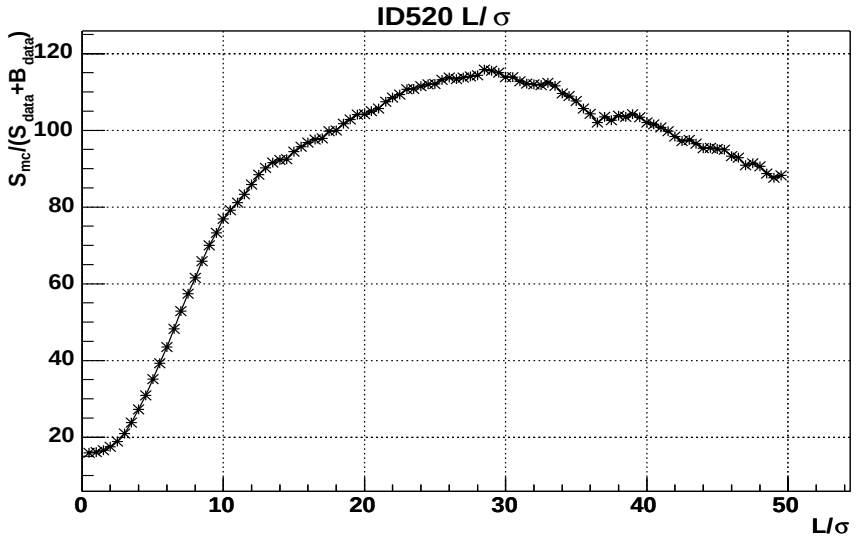

Figure A.1: $\Xi_c^+ -> \Xi^-\pi^+\pi^+$ significance variation with respect to L/σ cut.

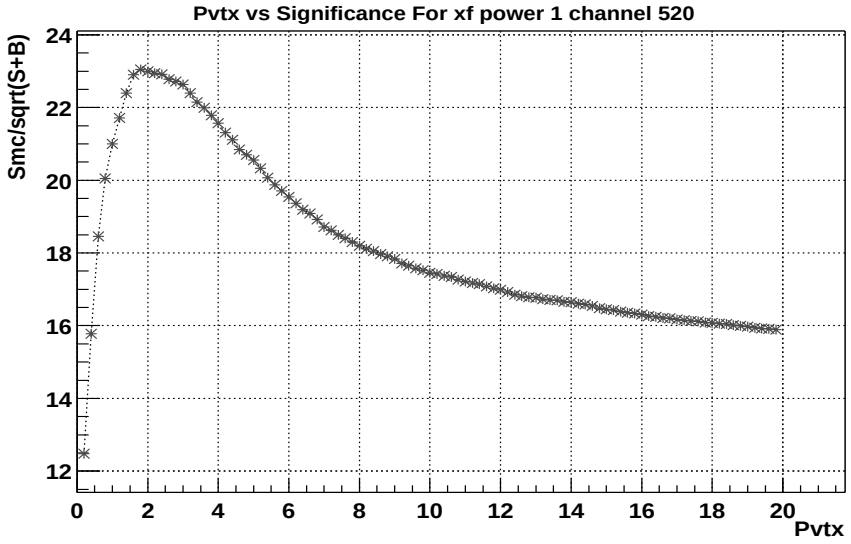

Figure A.2: $\Xi_c^+ -> \Xi^-\pi^+\pi^+$ significance variation with respect to Pvtx cut.

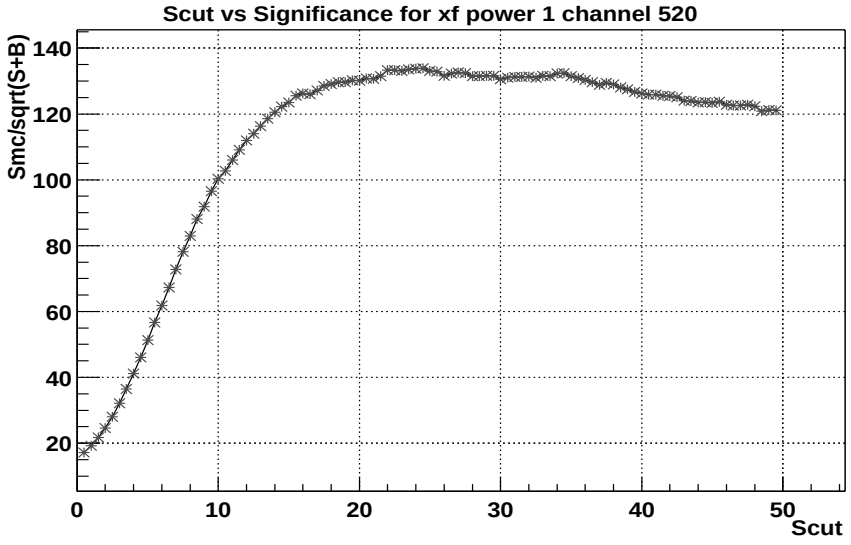

Figure A.3: $\Xi_c^+ -> \Xi^-\pi^+\pi^+$ significance variation with respect to Scut cut.

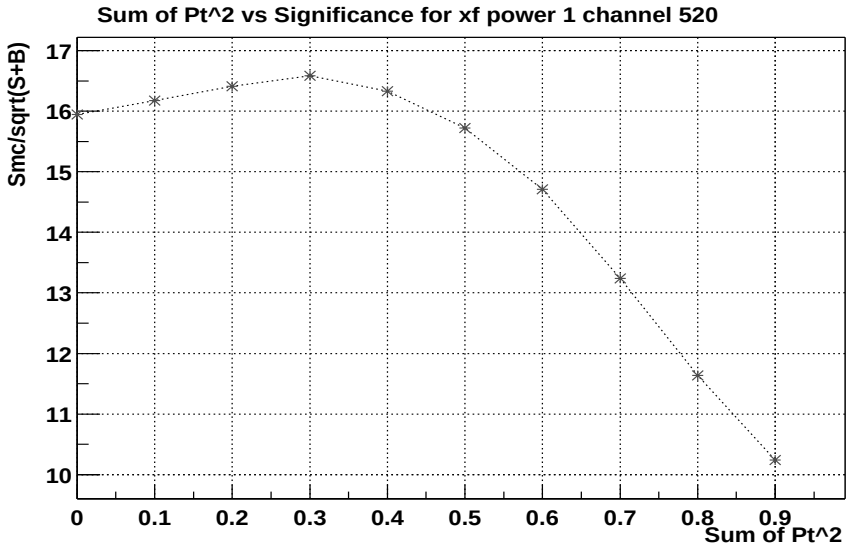

Figure A.4: $\Xi_c^+ -> \Xi^-\pi^+\pi^+$ significance variation with respect to ΣP_t^2 cut.

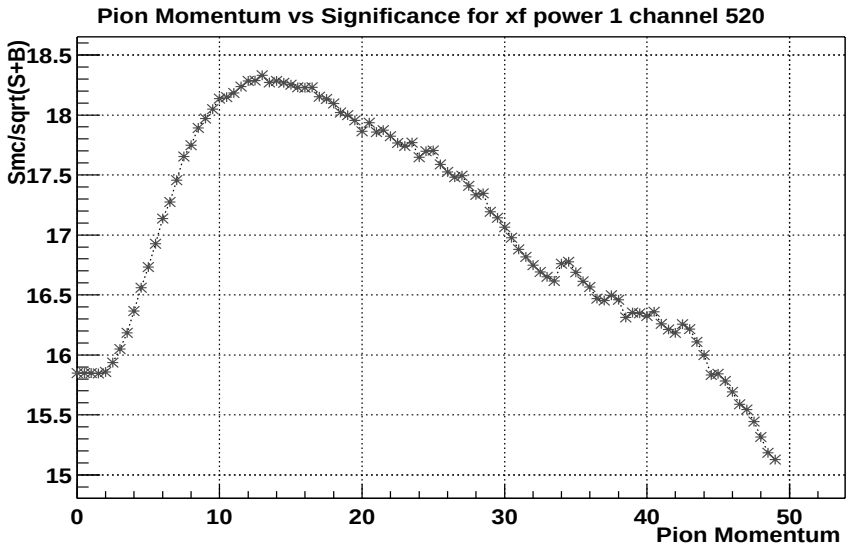

Figure A.5: $\Xi_c^+ -> \Xi^-\pi^+\pi^+$ significance variation with respect to pion momentum cut.

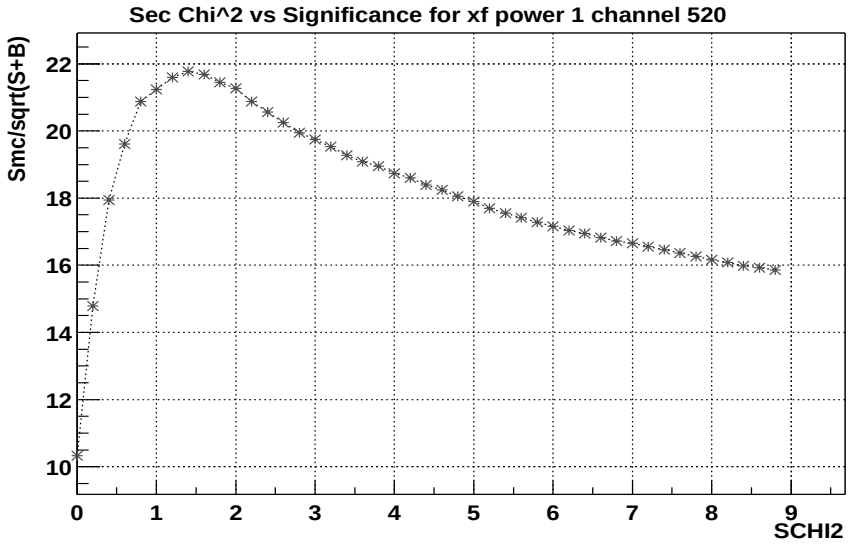

Figure A.6: $\Xi_c^+ -> \Xi^-\pi^+\pi^+$ significance variation with respect to χ^2 cut.

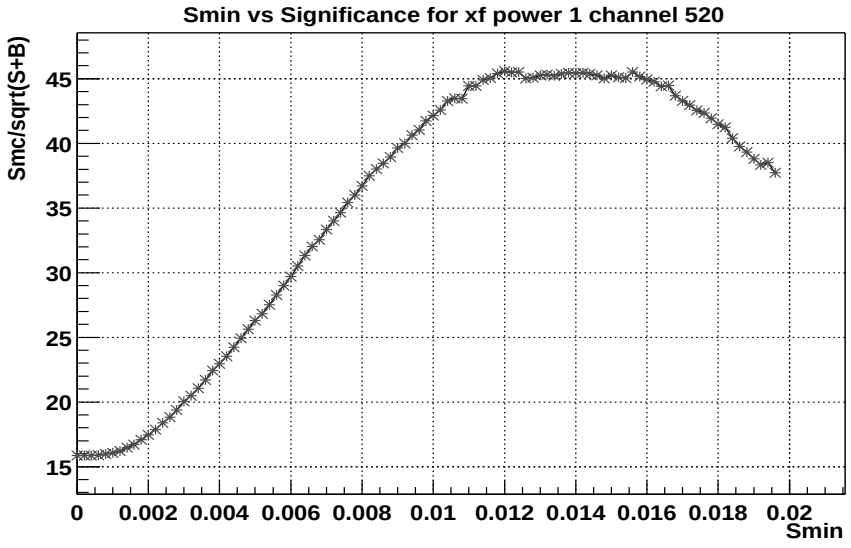

Figure A.7: $\Xi_c^+ -> \Xi^-\pi^+\pi^+$ significance variation with respect to Smin cut.

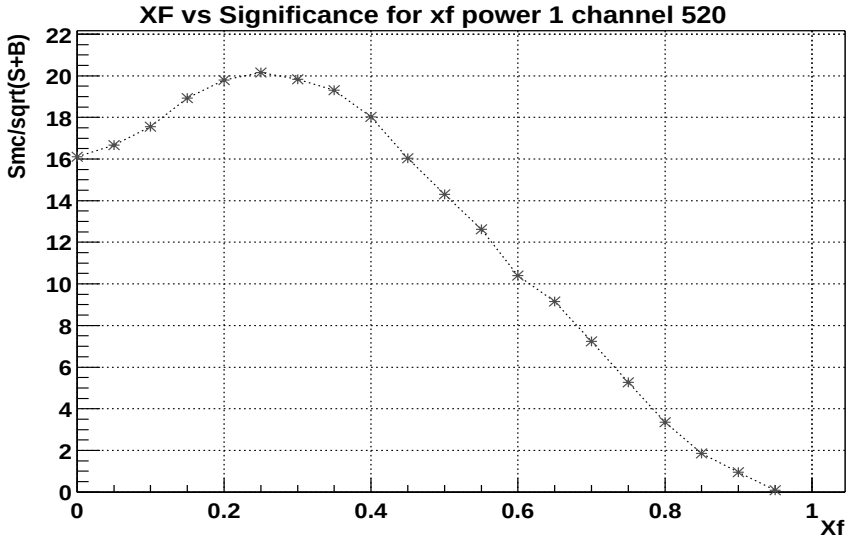

Figure A.8: $\Xi_c^+ -> \Xi^-\pi^+\pi^+$ significance variation with respect to x_f cut.

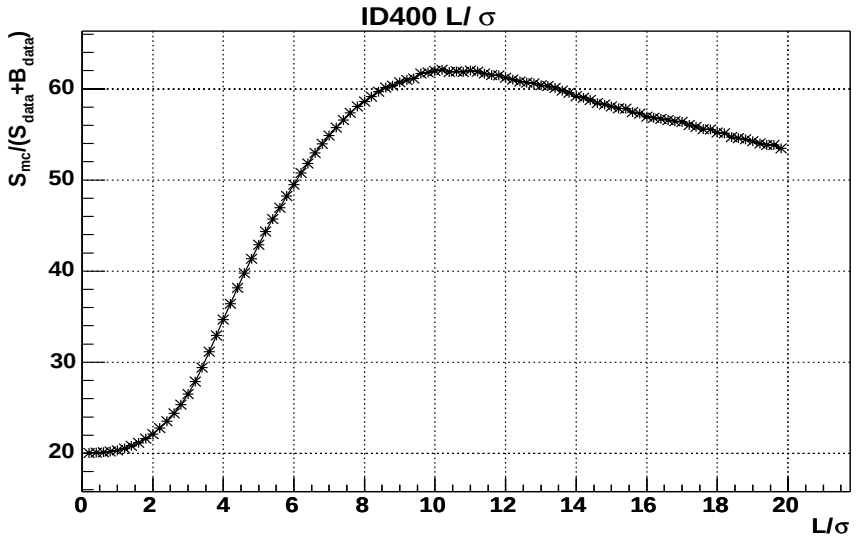

Figure A.9: $\Xi_c^+ -> p^+K^-\pi^+$ significance variation with respect to L/σ cut.

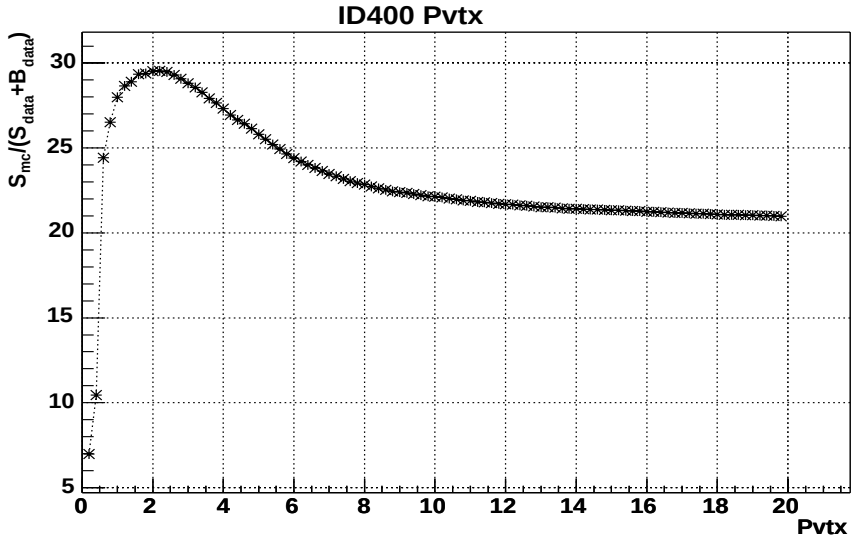

Figure A.10: $\Xi_c^+ -> p^+K^-\pi^+$ significance variation with respect to Pvtx cut.

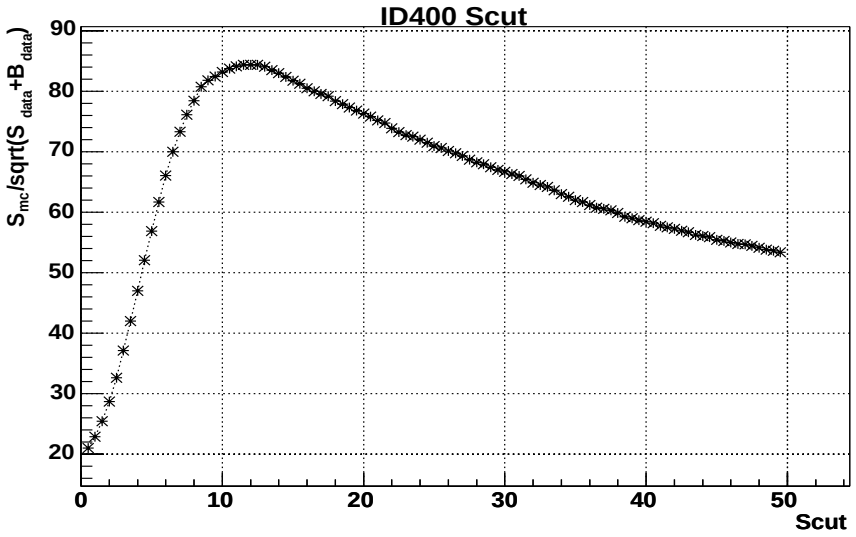

Figure A.11: $\Xi_c^+ -> p^+K^-\pi^+$ significance variation with respect to Scut cut.

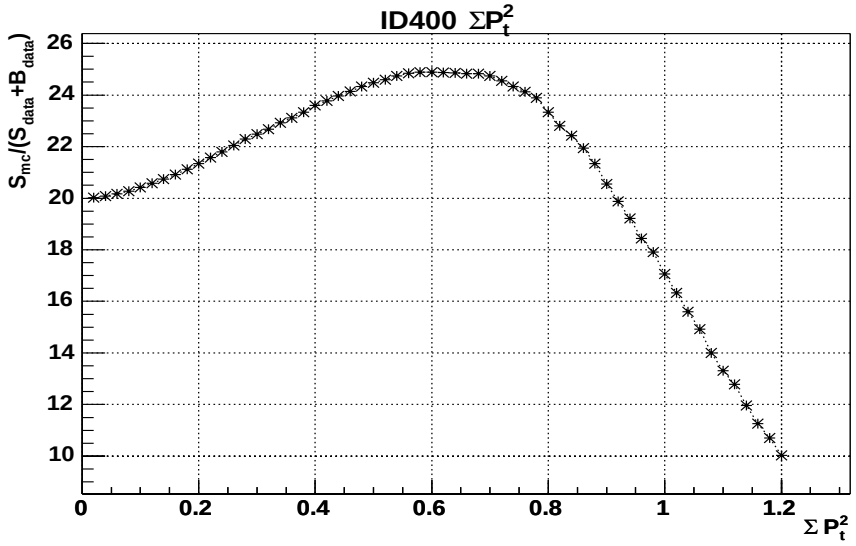

Figure A.12: $\Xi_c^+ -> p^+K^-\pi^+$ significance variation with respect to ΣP_t^2 cut.

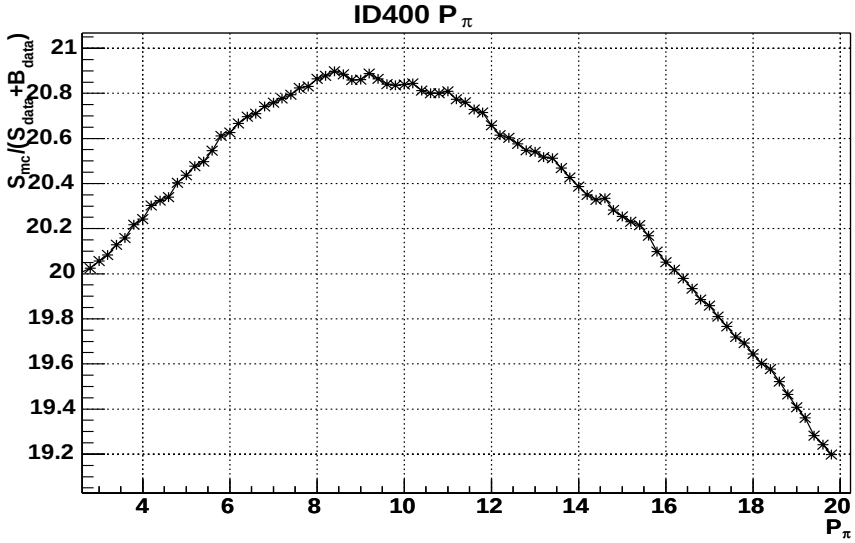

Figure A.13: $\Xi_c^+ -> p^+K^-\pi^+$ significance variation with respect to pion momentum cut.

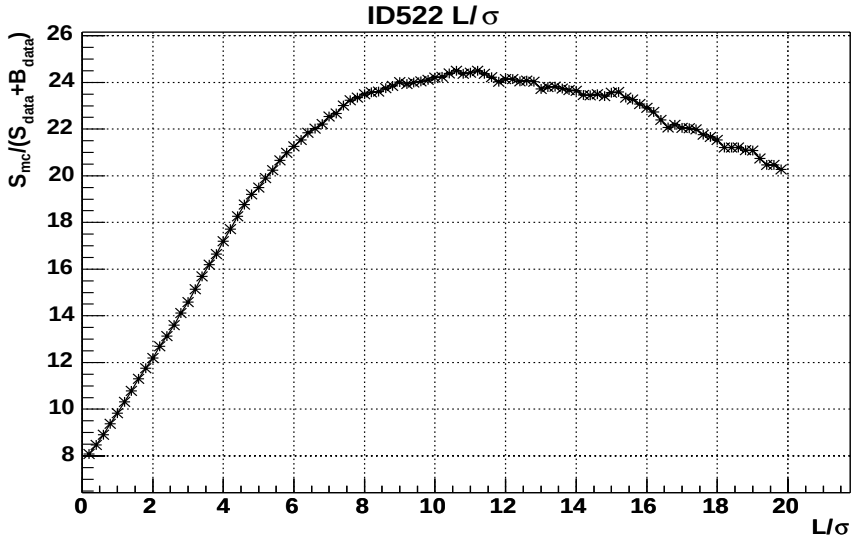

Figure A.14: $\Xi_c^+ -> \Sigma^+ K^- \pi^+$ significance variation with respect to L/σ cut.

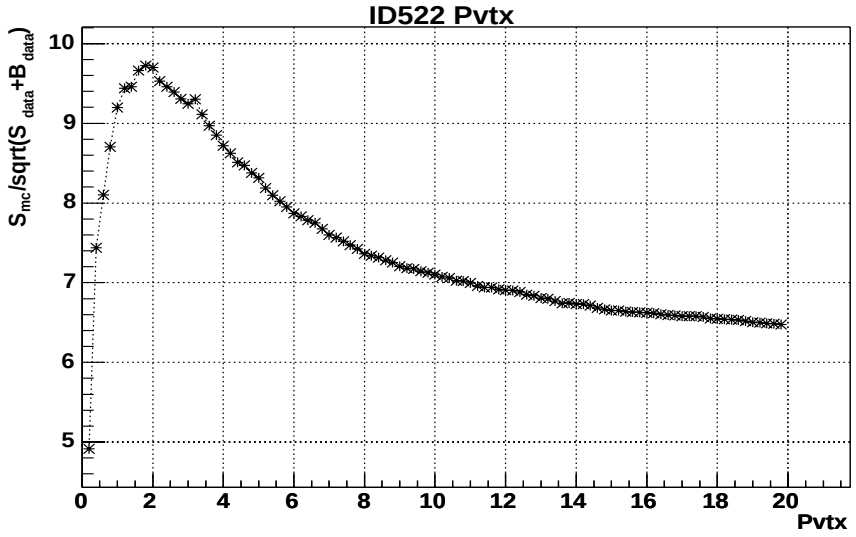

Figure A.15: $\Xi_c^+ -> \Sigma^+ K^- \pi^+$ significance variation with respect to Pvtx cut.

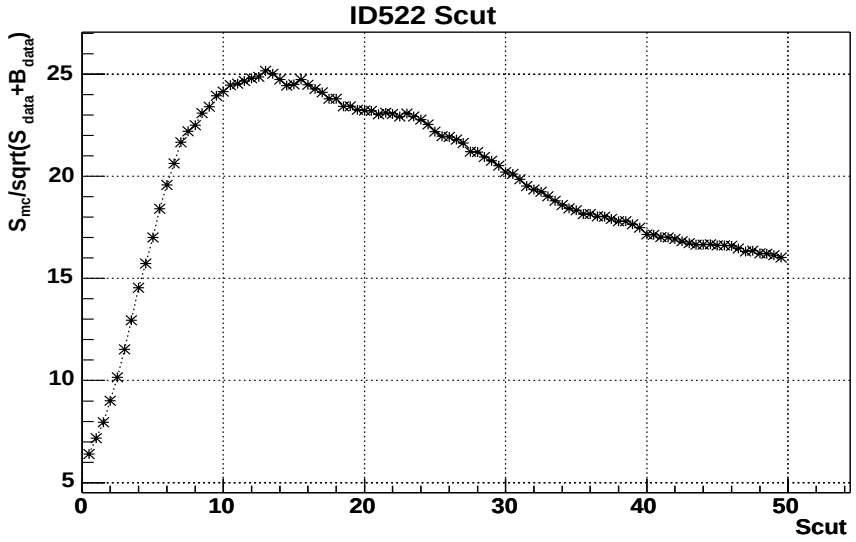

Figure A.16: $\Xi_c^+ -> \Sigma^+ K^- \pi^+$ significance variation with respect to Scut cut.

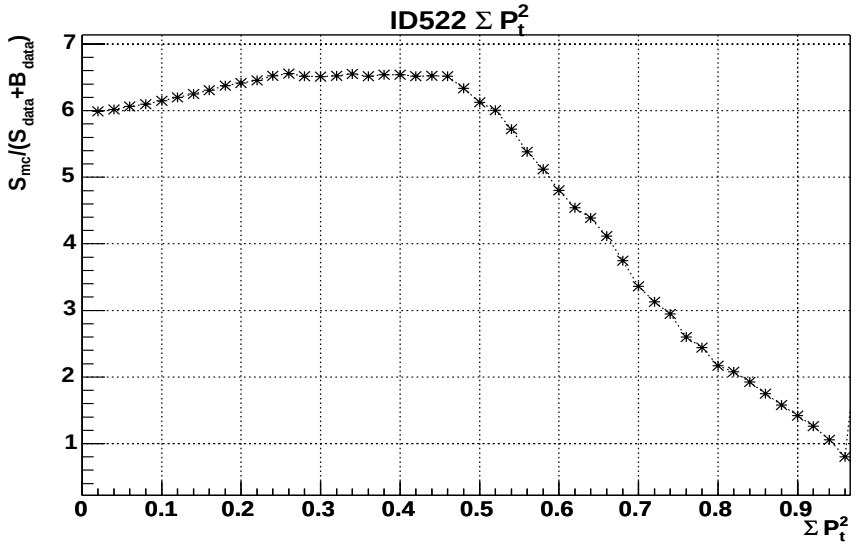

Figure A.17: $\Xi_c^+ -> \Sigma^+ K^- \pi^+$ significance variation with respect to ΣP_t^2 cut.

REFERENCES

[1] The CMS Collaboration, *CMS Technical Proposal*, CERN/LHCC 94-038, (1994).

[2] The ATLAS Collaboration, *ATLAS Technical Proposal*, CERN/LHCC 94-043, (1994).

[3] The ALICE Collaboration, *ALICE Technical Proposal*, CERN/LHCC 95-071, (1995).

[4] The LHCb Collaboration, *LHCb Technical Proposal*, CERN/LHCC 98-4, (1998).

[5] LEP Electroweak Working Group, *A Combination of Preliminary Electroweak Measurements and Constraints in Standard Model*, Presented by D. Charlton, EPS HEP 2001, Budapest, Hungary, July 12-18, (2001).

[6] U. Amaldi, W. de Boer and H. Fürstenau, Phys. Lett. **260B**, 447 (1991).

[7] U. Heinz and M. Jacob, *Evidence for a New State of Matter: An Assessment of the Results from the CERN Lead Beam Programme*, nucl-th/0002042.

[8] The CMS Collaboration, *The Compact Muon Solenoid Letter of Intent*, CERN/LHC 92-3 LHCC/I1 (1992).

[9] A. S. Ayan *et al.*, *Results from the Beam Test of the CMS Forward Quartz Fiber*

Calorimeter Pre-Production Prototype (PPP-I), CMS Note IN 2002/021, (2002).

[10] P. Gorodetzky, Rad. Phys and Chem. **41**, 253 (1993).

[11] N. Akchurin *et al.*; Nucl. Inst. Meth. **A379**, 526-527 (1996).

[12] V.V. Abramov *et al.*, *Studies of the response of the prototype CMS hadron calorimeter, including magnetic field effects, to pion, electron, and muon beams*, CMS Note 2000/003, (2000).

[13] N. Akchurin *et al.*, Nucl. Inst. Meth. **A400**, 267-278 (1997).

[14] N. Akchurin *et al.*, Nucl. Inst. Meth. **A399**, 202-226 (1997).

[15] N. Akchurin *et al.*, Nucl. Inst. Meth. **A409,**, 593-597 (1998).

[16] N. Akchurin et al., *PYTHIA-GEANT calculation of resolutions and reconstruction efficiencies in an Fe HF calorimeter*, CMS Note 2000-004, (2000).

[17] N. Akchurin *et al.*, *The η=3 region of EE, HE and HF: using 1 TeV jets in PYTHIA-GEANT*, CMS-Note 2000-006, (2000).

[18] N. Akchurin *et al.*, *Effects of channel-failure rates on the jet reconstruction efficiencies and resolutions in an Fe HF calorimeter*, CMS-Note 2000-005, (2000).

[19] N. Akchurin et al., *Preliminary results from situ quartz fiber neutron radiations*,

CMS-Note 1998-056, (1998).

[20] U. Akgun *et al.*, *Timing, Gain, and Dark Current Measurements of PMTs from Three Different Manufacturers for HF Calorimeter*, CMS Internal Note: IN 2002/032, (2002).

[21] U. Akgun *et. al.*, *Single and Double Pulse Linearity Studies Performed on Candidate PMTs for HF Calorimeter*, CMS Internal Note: IN 2002/030, (2002).

[22] U. Akgun *et al.*, *Single Photoelectron Spectrum Measurements of HF Calorimetry Candidate PMTs in The University of Iowa PMT Test Station*, CMS Internal Note: IN 2002/026, (2002).

[23] U. Akgun *et al.*, *Tests of the CMS-HF Light Guide System at the University of Iowa PMT Test Station*,CMS Internal Note: IN 2002/029, (2002).

[24] *Photomultiplier Tubes, Principles and Applications*, Philips Photonics, Philips France, (1994).

[25] *Photomultiplier Tubes, Basics and Applications*, Hamamatsu Photonics K.K. Editorial Committee, Hamamatsu Photonics K.K., (1999).

[26] *Techniques for Nuclear and Particle Physics Experiments*, W.R. Leo.

[27] U. Akgun *et al.*, *Comparison of the Candidate PMTs for the CMS HF Calorimeter*, CMS-NOTE 2003/029, (2003).

[28] U. Akgun *et al.*, *CMS HF Calorimeter Light Guide System Radiation Damage Studies*,CMS Internal Note: IN 2003/029, (2003).

[29] P. Bruecken *et al.*, *Radiation Effect Studies on High Efficiency Mirror (HEM) and Aluminized Mylar for the HF Optical Design.*, CMS Internal Note: IN 2002/031, (2003).

[30] SELEX Collaboration, J. S. Russ *et al.*,*Recent Results from SELEX*, Talk given at 30th International Conference on High-Energy Physics(ICHEP 2000), Osaka, Japan, 27 Jul - 2 Aug 2000, hep-ex/0010011.

[31] F. Garcia, *Hadroproducao do Barion Charmoso Λ_c no Experimento SELEX-E781*, PhD thesis, University of Sao Paulo, Sao Paulo, Brazil, (2000).

[32] E791 Collaboration, E. M. Aitala *et al.*,*Multidimensional resonance analysis of $\Lambda_c^+ \to pK^-\pi^+$*, PL **B471** (2000), 449-459, hep-ex/9912003.

[33] SELEX Collaboration, S. Y. Jun *et al.*,*Observation of the Cabibo suppressed decay $\Xi_c^+ \to pK^-\pi^+$*, PRL **84**, 1857-1861, (2000), hep-ex/9907062.

[34] FOCUS Collaboration, J. M. Link *et al.*,*Measurements of the Σ_c^0 and Σ_c^++ mass splitting*, PL **B488**, 218-224, (2000), hep-ex/0005011.

[35] FOCUS Collaboration, F. Fabri *et al.*,*Results on charmed meson spectroscopy from FOCUS*, Talk given at 30th International Conference on High-Energy Physics(ICHEP 2000), Osaka, Japan, 27 Jul - 2 Aug 2000.

[36] CLEO Collaboration, C. P. Jessop *et al.*,*Observation of two narrow states decaying into* $\Xi_c^+\gamma$ *and* $\Xi_c^0\gamma$, PRL **82**, 492-496, (1999), hep-ex/9810036.

[37] SELEX Collaboration, U. Dersch *et al.*,*Total crossection measurements with* π^-, Σ^- *and protons on nuclei and nucleons around 600 GeV/c*, Nucl. Phys. **B579**, 277, (2000), hep-ex/9910052.

[38] S. F. Biagi *et al.*,*Measurements of total crossection of* Σ^- *and* Ξ^- *on protons and deuterons between 74 GeV/c and 137 GeV/c*, Nucl. Phys. **B186**, 1, (1981).

[39] K. Vorwalter,*Determination of the Pion Charge Radius with a Silicon Microstrip Detector System*, PhD thesis, Max-Planc-Institut fur Kernphysik, 1998.

[40] I. Eschrich,*Measurement of the* Σ^- *charge radius at the Fermilab hyperon beam*, PhD thesis, Max-Planc-Institut fur Kernphysik, 1998.

[41] H. Krueger,*Untersuchung der elastischen Hadron-Electron-Streuung bei 540 Gev/c zur Messung des elektromagnetischen Ladungsradius des Protons*, PhD thesis, Max-Planc-Institut fur Kernphysik, 1999.

[42] G. Bunce *et al.*,Λ^0 *hyperon polarization in inclusive production by 300 GeV protons on beryllium*, PRL **36**, 1113-1116, (1976).

[43] J.Soffer, *Is the riddle of the hyperon polarization solved?*, Invited talk at Hyperon 99: Hyperon Physics Symposium, Batavia, Illinois, 27-29 Sept. 1999, hep-ph/9911373.

[44] P. Pogodin, *Polarization of Σ^+ hyperons produced by 800 GeV/c protons on copper and beryllium*, PhD thesis, The University of Iowa, 1999.

[45] K. Nelson, *Polarization of Λ^0 inclusively produced by a 610 GeV/c Σ^- beam*, PhD thesis, The University of Iowa, 1999.

[46] P. Mathew, *Construction and evaluation of a high resolution silicon microstrip tracking detector and utilization to determine interaction vertices*, PhD thesis, Carnegie Mellon University, 1997.

[47] N. Bondar *et al.*, *Beam Transition Radiation Detectors*, H-Note 746, SELEX Internal Report (1995).

[48] SELEX Collaboration, A. Atamantchuck *et al.*, *Design and Performance of the Fermilab E781 (SELEX) Hardware Scattering Trigger*, Nucl. Inst. Meth. **A425**, 529-535, (1999).

[49] U. Dersch *et al.*, *Mechanical design of the large angle silicon detectors*, H-Note 804, SELEX Internal Report, (1998).

[50] P. Pogodin *et al.*, *Drift chambers of the M1 spectrometer: the detector, electronics and software*, H-Note 788, SELEX Internal Report, (1997).

[51] M. K. A. Antonov, G. Dsyubenko, *Geometry of the assembled E781 Photon 1, 2 detectors*, H-Note 748, SELEX Internal Report, (1995).

[52] V. V. Davidenko, M. Kubantsev, *Photon database for E781*, SELEX Internal Report, (1996).

[53] V. Maleev, *Description and test results for DPWC and TRD in E781*, H-Note 747, SELEX Internal Report, (1995).

[54] SELEX Collaboration, J. Engelfried *et al.*, *The E781 (SELEX) RICH detector*, Nucl.Instrum.Meth. **A409**, 439, (1998).

[55] L. E. T. Lungov, *Vector drift chambers database*, H-Note 779,SELEX Internal Report, (1997).

[56] E687 Collaboration, P. L. Frabetti *et al.*, *Description and performance of the Fermilab E687 spectrometer*, Nucl.Instrum.Meth. **A320**, 519-547, (1992).

[57] E791 Collaboration, E. M. Aitala *et al.*, *Correlations between D and* $\overline{D}$ *mesons produced in 500 GeV/c* π^-*-nucleon interactions*, Eur. Phys. J. direct **C4**, 1-67, (1999) hep-ex/9809029.

[58] A. Kulyatsev *et al.*, *E781 hardware trigger preliminary design*, H-Note 676, SELEX Internal Report, (1994).

[59] J. Engelfried, P. Cooper, *The E781 Trigger and DAQ system*, H-Note 643, SELEX Internal Report, (1995).

[60] J. G. Korner and M. Kramer, Z. Phys. **C55**, 659 (1992).

[61] M. Bauer, B. Stech and M. Wirbel, Z. Phys, **C34**, 103 (1987).

[62] G. Bellini, I. I. Bigi, and P. J. Dornan, Phys. Rept. **289**, 1 (1997).

[63] M. B. Voloshin, Phys. Lett. **B515**, 74 (2001).

[64] G. Bonvicini *et al.*, Phys. Rev. Lett. **82**, 4586 (1999).

[65] R. Godang *et al.*, Phys. Rev. Lett. **84**, 5038 (2000).

[66] K. Abe *et al.*, hep-ex/0111026.

[67] Particle Data Group, K. Hagiwara*et al.*, Physical Review **D66**, 1, (2002).

[68] B. Blok and M. Shifman, in *Proceedings of the Third Workshop on the Physics at a Tau- Charm Factory*, Marbella, Spain, 1993, edited by R. Kirkby and J. Kirkby (Editions Frontieres, Gif-sur-Yvette, 1994).

[69] B. Guberina and B. Melic, Eur. Phys. J. C, **2**, 697, (1998).

[70] FOCUS Collaboration, J.M. Link *et al.*, *A Measurement of Lifetime Differences in the Neutral D Meson System*, Phys. Lett. **B485**, 62-70, (2000).

[71] CLEO Collaboration, S. E. Csorna *et al.*, *Lifetime Differences, Direct CP Violation and Partial Widths in D0 Meson Decays to K^+K^- and $\pi^+\pi^-$*, Phys. Rev. **D65**:092001, (2002).

[72] P. L. Frabetti *et al.*, PRL **70**, 1755, (1993).

[73] M. P. Alvarez *et al.*, Z. Physics **C47**, 539, (1990).

[74] S. Barlog *et al.*, PL **B218**, 374, (1989).

[75] J. C. Anjos *et al.*, PRL **60**, 1379, (1988).

[76] FOCUS Collaboration, J.M. Link *et al.*, *A High Statistics Measurement of the* $\Lambda_c{}^+$ *Lifetime*, Phys. Rev. Lett. **88**, 161801, (2002).

[77] CLEO Collaboration, A.H. Mahmood *et al.*, *Measurement of the* Λ_c^+ *Lifetime*, Phys. Rev. Lett.**86**:2232-2236, (2001).

[78] SELEX Collaboration, A. Kushnirenko *et al.*,*Precision measurements of the* Λ_c^+ *and* D^0 *lifetimes*, Phys. Rev. Lett. **86**, 5243 (2001), hep-ex/0010014.

[79] P.L. Frabetti *et al.*, PL **B427**, 211, (1998).

[80] S. Barlog *et al.*, PL **B233**, 522, (1989).

[81] P. Coteus *et al.*, PRL **59**, 1530, (1987).

[82] S. F. Biagi *et al.*, PL **150B**, 230, (1985).

[83] P. L. Frabetti *et al.*, PRL **70**, 2058, (1993).

[84] S. Barlog *et al.*, PL **B236**, 495, (1990).

[85] M. I. Adamovich *et al.*, PL **B358**, 151, (1995).

[86] P. L. Frabetti *et al.*, PL **B357**, 678, (1995).

[87] FOCUS Collaboration, J.M. Link *et al.*, *Measurement of the* Ω_c^0 *Lifetime*, Phys.Lett. **B561**, 41-48, (2003).

[88] FOCUS Collaboration, J.M. Link *et al.*, *A Measurement of the* Ξ_c^0 *Lifetime*, Phys.Lett. **B541**, 211-218, (2002).

[89] FOCUS Collaboration, J.M. Link *et al.*, *A New Measurement of the* Ξ_c^+ *Lifetime*, Phys.Lett. **B523**, 53-59, (2001).

[90] E687 Collaboration, P. L. Frabetti *et al.*, *A New Measurement of the Lifetime of the* Ξ_c^+, PL **B427** 211 (1998).

[91] CLEO Collaboration, A.H. Mahmood *et al.*, *Measurement of the* Ξ_c^+ *Lifetime*, Phys.Rev.**D65**:031102, (2002).

[92] CLEO Collaboration, M. Artuso *et al.*, *Measurement of the* Ξ_c^+ *Lifetime*, Phys. Rev. International Europhysics Conference on High Energy Physics (HEP 2001), Budapest, Hungary, 12-18 Jul 2001.

[93] B. Guberina, S. Nussinov, R. D. Peccei, and R. Ruckl, Phys. Lett. **B89**, 111, (1979).

[94] B. Guberina, R. Ruckl, and J. Trompetic, Z. Physics, **C33**, 297, (1986).